ROLE OF DOPANTS AND CHEMICAL SYNTHESIZATION ON THE PROPERTIES OF SUBSTITUTED COBALT FERRITC NANOPARTICLES

Thesis Submitted for the
Award of the Degree of
Doctor of Philosophy in Chemistry

To
Dr. Babasaheb Ambedkar Marathwada University,
Aurangabad.

By
Shri Mallinath Maruti Langade
Dept. Of Chemistry
Jawahar College, Andur Ta. Tuljapur

Under the Guidance of
Professor D.V. Mane
Dept. Of Chemistry, Shri Chhatrapati Shivaji College,
Omerga Dist. Osmanabad (M.S)

December, 2014

CERTIFICATE

This is to certify that the Thesis "***Role of Dopants and Chemical Synthesization on the Properties of Substituted Cobalt Ferrite Nanoparticles"*** being submitted by Shri **Mallinath Maruti Langade,** Submitted to Dr. Babasaheb Ambedkar Marathwada University, Aurangabad for the award of Doctor of Philosophy, is a record of bonafide research work carried out by him. He has worked under my guidance and supervision and has fulfilled the requirement for the submission of the thesis, which to my knowledge has reached the requisite standard.

The result contained in the thesis has not been submitted in part or in full to any other University / Institute for the award of any degree or diploma.

Place : Aurangabad

Research Guide
(Dr. D.V. Mane)
Professor & Deputy Director,
UGC- Academic Staff College,
Dr. Babasaheb Ambedkar Marathwada
University, Aurangabad

Date :

DECLARATION

I hereby declare that the Thesis titled ***“Role of dopants and Chemical Synthesization on the Properties of substituted Cobalt ferrite Nanoparticles”*** being submitted to Dr. Babasaheb Ambedkar Marathwada University, for the award of Doctorate in Philosophy, is a record of bonafide research work carried out by me under the guidance of **Dr. D.V. Mane,** Professor & Deputy Director, Academic Staff, College, Dr. Babasaheb Ambedkar Marathwada University Aurangabad.

The thesis has not been submitted in part or in full to any other University Institute for the award of any degree or diploma.

Place: Aurangabad
Date:

Mallinath. M. Langade
Research Student

Acknowledgement

I am happy today to express my deep indebtedness and gratitude's to Dr. D. V. Mane, Professor and Deputy Director, Academic Staff College, Dr. Babasaheb Ambedkar Marathwada University, Aurangabad. Under whose scholarly guidance and co-operative nature, this thesis was completed. He encouraged me to do my research work and achieve the aim of my life.

It's a very proud feeling for me to extend my gratitude's to Hon Sidramappa Alure, Guruji, Secretary of Shikshan Prasarak Mandal, Andur and Hon Madhukarraoji Chavan Saheb, President of Shikshan Prasarak Mandal, Andur whose blessings are always with me and inspired me to do my work. I am thankful to Principal Dr. Anita Mudkanna for providing Laboratory facilities and supported me always to finish my research work.

I am grateful to Dr. D. R. Mane , Registrar, Dr. Ashok Mohekar (Dean, faculty of science), Dr. S. N. Thore (Chairman, BOS in chemistry), Dr. Anjali Rajbhoj , (Head, Dept. Of Chemistry), Dr. Babasaheb Ambedkar Marathwada University, Aurangabad, Prof. M.S. Shingare, Prof. B. R. Arbad, Prof. R. A. Mane, Prof. T. K. Chondekar , Prof. M.S. Gill, Dr. M. K. Lande, Dr. S.T. Gaikwad, Dr. Sunil Shankarwar, Dr. Bhaskar Sathe, Dr. Bapurao Shingate and other administrative staff as well as the library section of Dr. BAMU, Aurangabad.

I am thankful to Head, dept. of physics, Savitribai Phule Pune University, Pune. Director, TIFR Trombay Laxai-Avanti lab, Hydrabad. I am very much thankful to Dr. N. D. Shinde, Principal, Shri Chhatrapati Shivaji College, Omerga, Dr. Somnath Akuskar, Principal Shri Madhavrao Patil College, Murum, Dr. Suhas Peshwe, Principal ASC College, Naldurg for providing me laboratory facilities during my research work.

I realize that no research work is possible without the collective endeavour. So it's my moral duty to express my gratitude's to Dr. Lohar Kisan whose encouragement and co-operation is hardly to be expressed in words. I am so much thankful to Dr. Ram Kadam, Dr. S.V. Rajmane , Dr. A. B. Kadam and my departmental colleges Dr. D. N. Gattlewar, Dr. V.G. Mane, Prof. S. B. Shaiwale , Shri P. R. Bhure and Shri D. R. Chavan for having moral support.

I specially express my deep gratitude’s to Shri. Amol Pachpinde who has lightened the burden of my academic work and helped me always whenever I need his support. I very much thankful to Dr. Jaiprakash Sangshetti, Y.C. College of Pharmacy, Aurangabad for his guidance during research work.

I wish to record my tributes to my dearest late. Annarao Muley Mama, My father Mr. Marutirao Langade, My Mother Mrs. Tangawa, My brother Mr. Shrishail, sister Mrs. Uma, other family members and all my friends who have always been the part of my encouragement. I am thankful to my wife Dr. Anita, my lovely daughters Vaishnavi & Krishnai for having supported me to complete this task.

Shri M. M. Langade

Contents

Chapter 1

Introduction to ferrites

1.1 Introduction

Now a day's nanotechnology is an important branch of science and technology and has taken a lead role in the 21st century. In current material science, nano scale materials have stimulated great interest due to their importance in basic scientific research and potential technology applications such as microelectronic devices [1], chemical and biological sensors [2], light emitting displays [3], catalysis [4], energy storage and conversion devices [5], water splitting [6], dye sentisitized solar cells (DSSCs) [7, 8], photo catalysis [9] etc. In the past decade, nano materials have been the subject of enormous interest because fundamental physical, chemical, electronic, magnetic and optical properties are also quite different at this nano level when compared to larger scale materials and they have potential applications in nano scale devices [10-13]. This opens the new era for scientist, researchers, technologist and engineers to study the nano materials with different properties.

The chemical and physical properties of nano materials can significantly differ from those of bulk materials of same chemical composition. The uniqueness of the structural characteristics, energetics, response, dynamics and chemistry of nanostructures constitutes the experimental and conceptual background for the field of nanoscience. Suitable control of properties and response of nanostructures can lead to new devices and technologies. The underlying themes of nano science and nanotechnology are dual: first, the bottom-up approach of the self-assembly of molecular components where each molecular or nano structured component plugs itself into a superstructure [14]; second, the top-down approach of miniaturization of the components [15].The deviation of properties of the nano sized materials from the bulk material properties are due to surface effects which mainly depend upon the ratio of surface area to volume and size of the particles along with the chemical composition and interaction between particles. The increase in surface to volume ratio, which is a gradual progression as the particle gets smaller, leads to an increasing dominance of the behavior of atoms on the surface of particles over that of those in the interior of particle as these atoms have lower coordination number than the interior atoms. In addition, depending on the geometry, different sites on the surface will be different in local coordination number [16].In the last two decades; a class of materials with a nanometer-sized microstructure have been synthesized and studied. These materials are assembled from nanometer-sized building blocks, mostly crystallites. The building blocks may differ in their atomic structure, crystallographic orientation or chemical composition. In cases where the building blocks are crystallites, incoherent or coherent interfaces may be formed between them, depending on the atomic structure, the crystallographic orientation, and the chemical composition of adjacent crystallites. In other words, materials assembled of nanometer-sized building blocks are micro-structurally heterogeneous, consisting of the building blocks (e.g. crystallites) and the regions between adjacent building blocks (e.g. grain boundaries).The inherently heterogeneous structure on a nanometer scale that is crucial for many of their properties and also distinguishes them from glasses, gels etc., that are micro structurally homogeneous [17].

1.2 Magnetic nano particles

Magnetic nano particles are a class of nano particle which can be manipulated using magnetic field. Such particles commonly consist of magnetic elements such as iron, nickel and cobalt and their chemical compounds. While nano particles are smaller than 1 micrometer in diameter (typically 5–500 nanometers), the larger micro beads are 0.5–500 micrometer in diameter. The magnetic nano particles have been the focus of much research recently because they possess attractive properties which could see potential use in catalysis including nano material-based catalysts [18], biomedicine [19], magnetic resonance imaging [20], magnetic particle imaging [21], data storage [22], environmental remediation [23], nano fluids [24], and optical filters [25], defect sensor [26] and cation sensors [27].

1.2.1 Types of magnetic nano particles

Currently, three different kinds of magnetic nano particles are being produced and used

i) Oxides: ferrite

Ferrite nano particles are the most explored magnetic nano particles up to date. Once the ferrite particles become smaller than 128 nm [28] they become super paramagnetic which prevents self-agglomeration since they exhibit their magnetic behavior only when an external magnetic field is applied. With the external magnetic field switched off, the remanence falls back to zero. Just like non-magnetic oxide nano particles, the surface of ferrite nano particles is often modified by surfactants, silicones or phosphoric acid derivatives to increase their stability in solution [29]

ii) Metallic

Metallic nano particles have the great disadvantage of being pyrophoric and reactive to oxidizing agents to various degrees. This makes their handling difficult and enables unwanted side reactions.

iii) Metallic with a shell

The metallic core of magnetic nano particles may be passivated by gentle oxidation, surfactants, polymers and precious metals [30]. In an oxygen environment, Co nano particles form an anti-ferromagnetic CoO layer on the surface of the Co nano particle. Recently, work has explored the synthesis and exchange bias effect in these Co core CoO shell nano particles with a gold outer shell [31]. Nano particles with a magnetic core consisting either of elementary Iron or Cobalt with a non reactive shell made of graphene have been synthesized recently [32]. The advantages compared to ferrite or elemental nano particles are:

- Higher magnetization
- Higher stability in acidic and basic solution as well as organic solvents

- Chemistry [33] on the graphene surface via methods already known for carbon nano tubes

1.2.2 Applications of magnetic nano particles

i) Medical diagnostics and treatments

Magnetic nano particles are used in an experimental cancer treatment called magnetic hyperthermia [34] in which the fact that nano particles heat when they are placed in an alternative magnetic field is used.

Another potential treatment of cancer includes attaching magnetic nano particles to free-floating cancer cells, allowing them to be captured and carried out of the body. The treatment has been tested in the laboratory on mice and will be looked at in survival studies [35, 36].

Magnetic nano particles can be used for the detection of cancer. Blood can be inserted onto a micro fluidic chip with magnetic nano particles in it. These magnetic nano particles are trapped inside due to an externally applied magnetic field as the blood is free to flow through. The magnetic nano particles are coated with antibodies targeting cancer cells or proteins. The magnetic nano particles can be recovered and the attached cancer-associated molecules can be assayed to test for their existence.

Magnetic nano particles can be conjugated with carbohydrates and used for detection of bacteria. Iron oxide particles have been used for the detection of Gram negative bacteria like Escherichia coli and for detection of Gram positive bacteria like Streptococcus Suis [37, 38].

ii) Magnetic immunoassay

Magnetic immunoassay[39] (MIA) is a novel type of diagnostic immunoassay utilizing magnetic beads as labels in lieu of conventional, enzymes, radioisotopes or fluorescent moieties. This assay involves the specific binding of an antibody to its antigen, where a magnetic label is conjugated to one element of the pair. The presence of magnetic beads is then detected by a magnetic reader (magnetometer) which measures the magnetic field change induced by the beads. The signal measured by the magnetometer is proportional to the analyte (virus, toxin, bacteria, cardiac marker, etc.) quantity in the initial sample.

iii) Waste water treatment

Thanks to the easy separation by applying a magnetic field and the very large surface to volume ratio, magnetic nano particles have a good potential for treatment of contaminated water [40]. In this method, attachment of EDTA-like chelators to carbon coated metal nano magnets results in a magnetic reagent for the rapid removal of heavy metals from solutions or contaminated water by three orders of magnitude to concentrations as low as micrograms per litre.

iv) Chemistry

Magnetic nano particles are being used or have the potential use as a catalyst or catalyst supports [41]. In chemistry, a catalyst support is the material, usually a solid with a high surface area, to which a catalyst is affixed. The reactivity of heterogeneous catalysts occurs at the surface atoms. Consequently great effort is made to maximize the surface area of a catalyst by distributing it over the support. The support may be inert or participate in the catalytic reactions. Typical supports include various kinds of carbon, alumina, and silica.

v) Biomedical imaging

There are many applications for iron-oxide based nano particles in concert with magnetic resonance imaging [42]. Magnetic CoPt nano particles are being used as an MRI contrast agent for transplanted neural stem cell detection [43].

vi) Information storage

Research is going into the use of using MNPs for magnetic recording media. The most promising candidate for high-density storage is the face-centered tetragonal phase FePt alloy. Grain sizes can be as small as 3 nanometers. If it's possible to modify the MNPs at this small scale, the information density that can be achieved with this media could easily surpass 1 Terabyte per square inch [44].

vii) Genetic engineering

Magnetic nano particles can be used for a variety of genetics applications. One application is the isolation of mRNA. This can be done quickly – usually within 15 minutes. In this particular application, the magnetic bead is attached to a poly T tail. When mixed with mRNA, the poly A tail of the mRNA will attach to the bead's poly T tail and the isolation takes place simply by placing a magnet on the side of the tube and pouring out the liquid. Magnetic beads have also been used in plasmid assembly. Rapid genetic circuit construction has been achieved by the sequential addition of genes onto a growing genetic chain, using nano beads as an anchor. This method has been shown to be much faster than previous methods, taking less than an hour to create functional multi-gene constructs in vitro [45].

1.3 Magnetic materials

Magnetic materials can be divided into two group soft and hard magnetic materials. The soft magnetic materials are those materials which are magnetized and demagnetized easily while the hard magnetic materials are those which are difficult to magnetize and demagnetize. The hard magnetic materials have high coercively, because the high coercivity resists the magnetization action. The basic difference of two types of permanent magnets was described on the basis of hysteresis loop. The soft magnetic materials exhibit a narrow hysteresis loop, whereas; the hard magnetic materials show a broad hysteresis loop. In the narrow hysteresis loop magnetization follows the variation of the applied field without significant loss. The broad hysteresis loop shows the magnetic energy that can be stored in the materials [46].

1.3.1 Soft magnetic materials

Soft magnetic materials can be easily magnetized and demagnetized. They retain their magnetization only in presence of a magnetic field. They show a narrow hysteresisloop, so that the magnetization follows the variation of applied field nearly without hysteresis loss [47]. They are used to enhance the flux, produced by an electric current in them. The quality factor of a soft magnetic material is to measure of its permeability with respect to the applied magnetic field. The other main parameter is the coercivity, saturation magnetization and the electrical conductivity. An ideal soft magnetic material would have low coercivity (Hc), a very large saturation magnetization (Ms), zero remanence (Br), zero hysteresis loss and very large permeability [48].

1.3.2 Hard magnetic materials

Hard Magnetic materials also called as permanent magnets are used to produce strong field without applying a current to coil. Permanent magnets required high coercivity, so they should exhibit a strong net magnetization and is stable in the presence of external fields, which requires high coercivity. In hard magnetic materials uniaxial magnetic anisotropy is necessary and the following magnetic properties are required[49]. Important properties of hard magnetic materials are mentioned below:

i) High coercivity:

The coercivity, also called the coercive field, of a ferromagnetic material is the intensity of the applied magnetic field required to reduce the magnetization of that material to zero after the magnetization of the sample has been driven to saturation. Coercivity is usually measured in oersted or ampere/meter units and is denoted Hc. Materials with high coercivity are called hard ferromagnetic materials, and are used to make permanent magnets [50].

ii) Large magnetization:

The process of making a substance temporarily or permanently magnetic, as by insertion the material in a magnetic field.

iii) Rectangular hysteresis loop:

A hysteresis loop shows the relationship between the induced magnetic flux density (B) and the magnetizing force (H). hard magnetic materials have rectangular hysteresis loop [51].

1.4 Ferrites

Ferrites are magnetic ceramics containing iron oxide as a major constituent in it. It is now some 70 years since ferrites debuted as an important new category of magnetic materials. These are now very well established group of magnetic materials. Today ferrites are employed in a truly wide range of applications, and have contributed materially to the advances in electronics. In the area of new materials, ferrites with permeabilities up to 30,000 and power ferrites for frequencies up to 10 MHz have been made available commercially. Even though, improvements and innovations continue to take place; many new applications, theories and preparation technologies are currently under development in field of ferrites.

Ferrites are iron based oxides with technologically fascinating magnetic properties, making them a prominent category in magnetic materials. The ferrite particles in nano-regime with significant change of physical properties provide more advantages over the bulk ferrites [52]. With regards to the rapidly mounting field of nanotechnology, ferrite nano particles have been the core of extensive research pertaining to their widespread applications, be it biomedical, techno- logical or industrial. Nano crystalline particles of magnetic materials show substantially enhanced magnetic properties.

The unit cell of the spinel ferrite is formed by doubling the face centered cubic oxygen sub lattice along each of the three dimensions. In this arrangement 64 tetrahedral or A-sitesand 32 octahedral or B-sites are created in the unit cell. In stoichio metric spinels only 8 A-sites and16 B-sites are filled by divalent transition-metal ions. The spine compounds belong to the space group Fd3m ($F^{4}{}_{1/d}3_{2/m}$, No. 227 in the International Tables for X-ray Crystallography)with lattice parameter 8.5 Å. In mixed spinel ferrites the concentrations of ferrous, ferric and substituted metal ions and their distribution over tetrahedral and octahedral sites play a vital role in determining their magnetic and electrical properties. In normal spinels, all the A-sites are occupied by divalent transition metal ions while in inverse spinels; the divalent ions occupy B-sites. In disordered spinels the divalent ions are present on both

A and B-sites. The normal and inverse spinels are two extremes between which the cation distribution may vary. When the origin of the unit cell is taken at the centers of symmetry$\bar{4}$3m and $\bar{3}$ m, then oxygen positional parameter '*u*' (the distance between the oxygen ion and the face of the cube edge along the cube diagonal of the spinel sub cell) has ideal values 0.375 (3/8) and 0.250 (1/4) respectively, for a perfect cubic close-packed arrangement of oxygen ions. In this case the octahedral cation–anion distance or bond length is 1.155 times larger than the tetrahedral bond length. A deviation from the ideal structure occurs when oxygen is displaced along [111] direction to accommodate the constituent cations, the tetrahedral site with smaller volume enlarges at the expense of the octahedral site and then u a value greater than 0.375.In order to control the domain of ferrite's applications, the investigation of cation distribution on A and B sites and oxygen positional parameter u, is most important [53, 54].

1.4.1 Applications of ferrites

The field of spinel ferrites is well cultivated because of their various potential applications and the interesting physics involved in it. Even after more than half of the century the scientist, researchers, technologist, and engineers are still excited in various types of bulk as well as nano crystalline ferrite materials. The recent trend is focused on the doped ferrites prepared using various synthesis techniques with different cation concentrations which intern affects the various properties like, electrical, dielectric, and magnetic behavior. Ferrite materials are important magnetic materials, which have various applications in power conditioning and conversion. Due to their distinct magnetic properties, ferrite materials have been widely used to prepare many electromagnetic devices such as inductors, converters, phase shifters and electromagnetic wave absorbers [55, 56].

Industrial applications of magnetic nano particles cover abroad spectrum such as magnetic seals in motors, magnetic inks for bank cards, magnetic recording media and biomedical applications such as magnetic resonance contrast media and therapeutic agents in cancer treatment [57-61].Each potential application requires the magnetic nano particles to have different properties. For example, in data storage applications, the particles need to have a stable, switchable magnetic state to represent bits of information, a state that is not affected by temperature fluctuations.

Inductors: Ferrites are primarily used as inductive components in a large variety of electronic circuits such as lownoise amplifiers, filters, voltage-controlled oscillators, impedance matching networks, for instance. Their recent applications as inductors obey, among other tendencies, to the general trend of miniaturization and integration as ferrite multilayers for passive functional electronic devices. The multilayer technology has become a key technology for mass production of integrated devices; multilayers allow a high degree of integration density. Multilayer capacitors penetrated the market a few decades ago, while inductors started in the 1980s.

High Frequency: There has been an increasing demand of magnetic materials for high-frequency applications such as telecommunications and radar systems, as microwave technology requires higher frequencies and bandwidths up to100 GHz. Ferrites are non conducting oxides and therefore allow total penetration of electromagnetic fields, in contrast with metals, where the skin effect severely limits the penetration of high-frequency fields [62].

Power Application: Power applications of ferrites are dominated by the power supplies for a large variety of devices such as computers, all kinds of peripherals, TV and video systems, and all types of small and medium instruments. The main applications in the systems known as switched-mode power supplies (SMPS). In this application, the mains power signal is first rectified it is then switched as regular pulses (typically rectangular) at a high frequency to feed into a ferrite transformer, and finally it is rectified again to provide the required power to the instrument. An increase in power delivery and efficiency can be obtained by increasing the working frequency of the transformer.

Electromagnetic Interference (EMI) Suppression: The significant increase in the amount of electronic equipment such as high-speed digital interfaces in notebooks and computers, digital cameras, scanners, and so forth, in small areas, has seriously enhanced the possibility of disturbing each other by electromagnetic interference (EMI). In particular, the fast development of wireless communications has led to interference induced by electric and magnetic fields. Electromagnetic interference can be defined as the degradation in performance of an electronic system caused by an electromagnetic disturbance [63]. The noise from electric devices is usually produced at frequencies higher than circuit signals. To avoid, or at least reduce EMI, suppressors should work as low-pass filters, that is, circuits that block signals with frequencies higher than a given frequency value. There are several approaches to build EMI suppressors: soft ferrites [64], ferromagnetic metals [65], ferromagnetic metal/hexaferrite composites [66], encapsulated magnetic particles [67], and carbon nano tube composites [68].

High-density write-once optical recording: Thin films of defect spinel ferrites can be used as write-once read-many media working with blue wavelengths. In fact, because these non-stoichio metric ferrites are meta stable, they can be transformed into corundum phases at moderate temperatures by a laser spot. The transformed regions have different optical indices from the starting ferrite film, making the readout process possible.

Magnetic sensors: These are used for temperature control and these can be made using ferrite with sharp and definite Curie temperature. Position and rotational angle sensors (proximity switches) have also been designed using ferrites.

Magnetic shielding: A radar absorbing paint containing ferrite has been developed to render an aircraft of submarine invisible to radar.

Pollution control: There are several Japanese installations which use precipitation of ferrite precursors to scavenge pollutant materials such as mercury from waste streams. The ferrites produced subsequently can be separated magnetically along with the pollutant.

Ferrite electrodes: Because of their high corrosion resistance, ferrites having the appropriate conductivities have been used as electrode in applications such as chromium plating.

Entertainment ferrites: Ferrites are widely used in radio and television circuits. Typically applications include deflection Yokes, fly back transformers and SMPS transformer for power applications.

1.5 Literature survey and aim of the present work

The structural, magnetic and dielectric properties of ferrites are of great importance to select materials for specific applications. Some factors which affect the properties of ferrites are the type and amount of substitution, chemical composition, methods of preparation and different types of irradiation. Since the research on ferrites is so vast, it is very difficult to collect all the experimental results and information's about all types of ferrites in every aspect that's why restrict our self to present a systematic review of different theoretical and experimental facts related to this present study. This literature survey not only highlights the various modifications attempted by various researchers and to mention the updated research activities in this important field but also to recognize the possible potential applications for which this material is of crucial significance.

Cobalt ferrite ($CoFe_2O_4$) a well-known hard ferromagnetic material, in its bulk form crystallizes in mixed spinel structure with space group Fd3m represented as $(Co_x^{2+}Fe_{1-x}^{3+})[Co_{1-x}^{2+}Fe_{1+x}^{3+}]O_4$, where round and square brackets indicate A and B sites, respectively, and x depends on the thermal history and preparation conditions [69]. The anti parallel alignment of magnetic moments of A-site with B-site is coupled by super exchange interaction through the O^{2-} ions, which shows ferri magnetism [70]. Since the $Fe_A^{3+} - Fe_B^{3+}$ super exchange interactions differs from the $Co_A^{2+} - Fe_B^{3+}$ interactions, variation of the cation distribution over the A and B sites in the spinel leads to different magnetic properties of this ferrite even though the chemical compositions of the compounds do not change [71]. It has a curie temperature around ~ 520 °C, and exhibits high coercivity, moderate saturation magnetisation and good chemical stability [72]. Hence this material is a promising candidate for most technological applications at room temperature such as data storage devices, magnetic sensors, actuators, targeted drug delivery, medical diagnosis, etc. [73-76]. The cubic $CoFe_2O_4$ has large magneto crystalline anisotropy energy with positive anisotropy constant. It has six easy directions along the cube edges of the crystal represented as <100>, four hard directions across the body diagonals denoted as <111> and twelve saddle points across the face diagonals, which lead to positive magneto crystalline anisotropy constant [77,78]. The large magneto crystalline anisotropy energy of cobalt ferrite is mainly attributed to the Co^{2+} ions on the B sites of the spinel. As the crystal field is not capable to quench the orbital magnetic moment, there is a strong spin-orbit coupling (L-S coupling) and due to this coupling there is large magneto crystalline anisotropy energy (MAE) [79].

The properties of ferrites are greatly depends upon the type and amount of do pant. Cr^{3+} and Al^{3+} ions are known to change the properties of ferrite and are invested by several workers. Jianxun Qiu et al. studied the Effect of Cr substitution on microwave absorption of $BaFe_{12}O_{19}$ [80]. Vasambekar et al. studied cation distribution and susceptibility study of Cd-Co and Cr^{3+}substituted Cd-Co ferrites [81]. Radhapiyari et.al. studied magnetic properties of Cr^{3+} substituted Li-Sb ferrites [82]. The effect of Al-substitution on the magnetic and electrical properties of different ferrites was studied by many authors [83-87]. Influence of Al^{3+} ion concentration on the crystal structure and magnetic anisotropy of nano crystalline spinel cobalt ferrite has been studied by Lawrence Kumar and Manoranjan Kar [88]. Gul et. al. studied Optical, magnetic and electrical investigation of cobalt ferrite nano particles synthesized by co-precipitation route [89].

The substitutional effect of Cr^{3+} ions, when they replaces Fe^{3+} ions show some interesting results [90,91]. The effect of replacement of Fe^{3+} ions by Cr^{3+} ion have been studied by various workers [92, 93]. Lee et al. studied the magnetic properties and showed magnetic moment and Curie temperature decreases with Cr^{3+} substitution [94]. Magnetic properties like remanence and coercivity which are of utmost technological importance could be modified and controlled by Cr^{3+} substitution [95]. It was also found that the crystallographic transport and magnetic properties were also affected for Cr-substituted ferrites [96].

Manganese ferrite ($MnFe_2O_4$), Mn-Fe-O has received a great attention in the area of magnetic storage device, microwave, and electronic device because it has high magnetic permeability and high electrical resistance. Many research groups have investigated to enhance the magnetic property of magnetic materials such as manganese ferrite. $MnFe_2O_4$ is a ferrimagnet (T_N= 560 K) having the spinel structure with two in equivalnt sub lattices of tetrahedral (A) and octahedral [B] symmetries for the magnetic ions sites [97-100].Mn cation in spinel is at its high spin state. Its five d electrons display the configurations $e^2t_2^3$ and $t_{2g}^3e_g^2$ at the tetrahedral and octahedral lattice site, respectively. As a result, the coupling between the electron spin and the angular momentum of its orbital should be rather small in Mn cations [101].

By considering the above facts and importance of cobalt ferrite, manganese ferrite and Al^{3+}/Cr^{3+}substitution it was decided that to prepare the $CoMn_{1-x}Al_xFeO_4$ and $CoMn_{1-x}Cr_xFeO_4$ ferrite systems where x = 0.0-1.0 in steps of x = 0.25, in order to investigate structural and magnetic properties.

References

[1] L.J. Lauhon, M.S. Gudiksen, C.L. Wang and C.M. Lieber, Nature, 420 (2002) 57.

[2] A. Modi, N. Koratkar, E. Lass, B.Q. Wei and P.M. Ajayan, Nature, 424 (2003)171.

[3] D. Banerjee, S.H. Jo and Z.F. Ren, Adv. Mater., 16 (2004) 2028

[4] V. Bansal, H. Jani, P.J. Du, P.J. Coloe and S.K. Bhargava, Adv. Mater, 20 (2008) 717

[5] A.S. Arico, P. Bruce, B. Scrosati, J.M. Tarascon and S.W. Van, Nat. Mater, 4 (2005) 366.

[6] A. Fujishima and K. Honda, Nature, 238 (1972) 37.

[7] B. O'Regan and M. Graztel, Nature, 353 (1991) 737.

[8] G.K. Mor, K. Shandar, M. Paulose and C.A. Grimes, Nano. Lett., 6 (2006) 215.

[9] S.P. Albu, A. Ghicov, J.M. Macak and P. Schmuki, Nano Lett., 7 (2007) 1286.

[10] S. Lijima, Nature, 354 (1991)56.

[11] S.S. Wang, E. Joselevich, A.T. Wooley, C.L. Cheung and C.M. Liber, Nature, 394 (1998) 52

[12] Y. Huang, X. Duan, Y. Cui, L.J. Lauhon, K. Kim and C.M. Lieber, Science, 294 (2001) 1313.

[13] W.Q. Han, S.S. Fan, Q.Q. Li and Y.D. Hu, Science, 277 (1997) 1287.

[14] R. P. Feynman, *Miniaturization;* Reinhold: New York, 2001.

[15] J. M.Lehn, *Super molecular Chemistry*; VCH: Weinheim, 1995.

[16] L. E.Smart, E. A.Moore, *Solid State Chemistry*; CRC: New York, 2005.

[17] K. J.Klabunde, *Nano scale Materials in Chemistry*; Wiley Inter science: New York, 2001.

[18] A.-H. Lu, W. Schmidt, N. Matoussevitch, H. Bönnemann, B. Spliethoff, B. Tesche, E. Bill, W. Kiefer, F. Schüth, "Nano engineering of a

Magnetically Separable Hydrogenation Catalyst". Angewandte Chemie International Edition 43 (2004) 4303–4306.

[19] A. K. Gupta, M. Gupta, Biomaterials 26 (2005) 3995–4021.

[20] S. Mornet, S. Vasseur, F. Grasset, P. Verveka, G. Goglio, A. Demourgues, J. Portier, E. Pollert, E. Duguet, Prog. Solid State Chem. 34 (2006) 237.

[21] B. Gleich, J. Weizenecker, Nature 435 (2005) 1214–1217.

[22] T. Hyeon, Chem. Commun. (2003) 927.

[23] D. W. Elliott, W.-X. Zhang. Environ. Sci. Technol. 35: (2001) 4922.

[24] J. Philip, Shima. P.D. B. Raj. Appl. Phys. Lett. 92 (2006) 043108.

[25] J.Philip, T.J. Kumar, P.Kalyanasundaram, B.Raj, Measurement Science & Technology 14 (2003) 1289–1294.

[26] V. Mahendran and J.Philip, Appl. Phys. Lett. 100 (2012) 073104.

[27] J. Philip, V. Mahendran, and Leona J. Felicia , J. Nano fluids 2 (2013) 112-119.

[28] An-Hui Lu, An-Hui; E. L. Salabas, and Ferdi Schüth, Angew. Chem. Int. Ed. 46 (2007) 1222–1244.

[29] D.K. Kim, M. Mikhaylova, et al. Chemistry of Materials 15 (2003) 1617–1627.

[30] A.-H. Lu, E. L. Salabas and F. Schüt, Angew. Chem. Int. Ed. 46 (2007) 1222–1244.

[31] Stephanie H. Johnson, C.L. Johnson, S.J. May, S. Hirsch, M.W. Cole, J.E. Spanier, Journal of Materials Chemistry 20 (2010) 439.

[32] R. N. Grass, N. Robert, W. J. Stark, J. Mater. Chem. 16 (2006) 1825.

[33] R.N. Grass, N. Robert, E.K. Athanassiou, W.J. Stark, Angew. Chem. Int. Ed. 46 (2007) 4909–12.

[34] I. Rabias et al., Biomicro fluidics 4 (2010) 024111.

[35] K.E. Scarberry, E.B. Dickerson, J.F. McDonald, Z.J. Zhang. Journal of the American Chemical Society 130 (2008) 10258–62.

[36] Using Magnetic Nano particles to Combat Cancer News wise, Retrieved on July 17, 2008.

[37] N. Parera Pera, A. Kouki, J. Finne, R. J. Pieters, Organic & Bio molecular Chemo 8 (2010) 2425–2429.

[38] Highlights in Chemical Biology. Rsc.org. (2007). Retrieved on (2011).

[39] Magnetic immunoassays: A new paradigm in POCT IVDt, (2008).

[40] F.M. Koehler, Fabian M.; M. Rossier, M. Waelle, E.K. Athanassiou, L.K. Limbach, R.N. Grass, D. Günther, W.J. Stark, Chem. Commun. 32 (2009) 4862–4.

[41] A. Schätz, Alexander; O. Reiser, W.J. Stark, Chem. Eur. J. 16 (2010) 8950–67.

[42] M. Colombo et al. Chem. Soc. Rev. 41(2012): 4306-34

[43] Xiaoting Meng, Xiaoting; Hugh C. Seton, Le T. Lu, Ian A. Prior, Nguyen T. K. Thanh and Bing Song, Nano scale 3 (2011) 977–984.

[44] Natalie A. Frey and Shouheng Sun Magnetic Nano particle for Information Storage Applications

[45] A Elaissari, J Chatterjee, M Hamoudeh and H Fessi, CRC Press. (2010) pp. 315–337.

[46] W. Ervens and H. Wilmesmeier, Ullmann’s Encyclopedia of Industrial Chemistry, fifth editionA16 (1990), 1-51.

[47] C.W. chen, Magnetism and Metallurgy of Magnetic materials, North Holland Publishing Company, 1997.

[48] W.H. Yeadon & A. W. Yeadon, Handbook of small Electric Motors,Mcgraw Hill Company Inc. USA, 2001.

[49] M. V. Rane, D. Bahadur, S. D. Kulkarni & S. K. Date, J. Magn, Magn. Mater. 293 (1999), 1256.

[50] J.D. Livingston, J. Appl. Phys.(1981), 522-541.

[51] Min Chen and David E. Nikles, Nano Lett. (2002) 211–214.

[52] A.A.Thant, S.Srimala ,P.Kaung ,M.Itoh ,O.Radzali, M.N.Ahmad Fauzi, *J. Austr. Ceram.Soc.*46(1)(2010)11–14.

[53] Tahir Abbas, Y. Khan, Mushtaq Ahmed, Shahid Anwar, *Solid State Commun.*82 (1992) 701–703.

[54] Abid Hussain, T. Abbas, Shahida B.Niazi, *Ceram. Inter.* 39 (2013) 1221–1225

[55] Alex Goldman, Modern Ferrite Technology, 2nd ed. Springer, New York (2006).

[56] S. Peng, X. Fu, H. Ge, Z. Fu, C. Wang, L.Qi and H. Miao, *J. Magn. Magn. Mater.* 323(2011)2513–2518

[57] M.R. Bhandare, H.V Jamadar., A.T. Pathan, B.K. Chougule and A.M. Shaikh,, *J. Alloys Compd.*509 (2011) 113–L118.

[58] B. M. Berkovsky, V. F. Medvedev and M. S. Krokov, Magnetic Fluids: Engineering Applications, Oxford: Oxford University Press, 1993.

[59] S. W. Charles and J. Popple well, Properties and applications of magnetic liquids Hand Book of Magnetic Materials vol 2, ed K.H.J. Buschow, (1986) 153.

[60] A. E. Merbach and E. Toth, The Chemistry of contrast agents in medical magnetic resonance imaging,Chichester, UK: Wiley, 2001.

[61] I. Hilbert, W. Andra, R. Bahring, A. Daum, R. Hergt,W. A. Kaiser, Invest. Radiol. 32 (1997) 705

[62] M. Pardavi-Horvath,*J. Magn. Magn. Mater.* 215 (2000) 171-183.

[63] G. Stojanovic, M. Damnjanovic, V. Desnica,L. Zivanov, R. Raghavendra, P. Bellew, N. Mcloughlin, *J. Magn. Magn. Mater.* 297 (2006) 76.

[64] Z. W. Li, L. Guoqing, L. Chen, W. Yuping, C. K. Ong, *J. Appl. Phys.*99 (2006) 063905.

[65] Y. B. Feng, T. Qiu, C. Y. Shen, X. -Y. Li , *IEEE Trans. Magn.*42 (2006) 363-369.

[66] B. W. Li, Y. Shen, Z.-X. Yue, C.-W. Nan, *Appl. Phys. Lett.*89 (2006) 132504.

[67] R. C. Che, C. Y. Zhi, C. Y. Liang, X. G. Zhou, ,*Appl. Phys. Lett.*88 (2006) 033105.

[68] C. Xiang, Y. Pan, X. Liu, X. Sun, X. Shi, J. Guo , ,*Appl. Phys. Lett.*87, (2005) 123103.

[69] S.A. Mazen, S.F. Mansour, E. Dhahri, H.M. Zaki, T.A. Elmosalami, J. Alloy. Compd. 470 (2009) 294-300.

[70] K. Haneda, A.H. Morrish, J. Appl. Phys. 63 (8) (1988) 4258.

[71] Anthony R. West, Solid State Chemistry and its Application, Wiley India Edition, 2009.

[72] A. Broese Van Groenou, P.F. Bongers, A.L. Stuyts, Mater. Sci. Eng. 3 (1968/69) 317.

[73] S. Chikazumi, Physics of Ferromagnetism, second ed., Oxford University Press, New York, 1997.

[74] Y. Yin, A.P. Alivisatos, Nature (London) 437 (2005) 664.

[75] M.A. El-Sayed, Acc. Chem. Res. 37 (2004) 326–333.

[76] B.Y. Geng, J.Z. Ma, X.W. Liu, Q.B. Du, M.G. Kong, L.D. Zhang, Appl. Phys. Lett. 90 (2007) 043120.

[77] S. Sun, C.B. Murray, D. Weller, L. Folks, A. Moser, Science 287 (2000) (1989).

[78] H. Shenker, Phys. Rev. 107 (1957) 1246.

[79] M. Walker, P.I. Mayo, K. O’Grady, S.W. Charles, R.W. Chantrell, J. Phys. Condens. Matter 5 (1993) 2779.

[80] Jianxun Qiu, Yi Wang, Mingyuan Gu, Mater. Lett. 60 (2006) 2728-2732

[81] P.N. Vasambekar, C.B. Kolekar, A.S. Vaingankar, J. Magn. Magn. Mater.186 (1998) 333Ð341

[82] Radhapiyari Laishram, Chandra Prakash, J. Magn. Magn. Mater. 305 (2006) 35-39

[83] A.G. Bhosale, B.K. Chougule, J. Mater. Chem. Phys. 97 (2006) 273–276.

[84] G.J. Baldha, K.G. Saija, K.B. Modi, H.H. Joshi, R.G. Kulkarni, J. Mater. Lett. 53 (2002) 233-237.

[85] Y.-P. Fu, S. Tsao, C.-T. Hu, Y.-D. Yao, J. Alloy Compd. 395 (2005) 272-276.

[86] A.M. Sankpal, S.S. Suryawanshi, S.V. Kakatkar, G.G. Tengshe, R.S. Patil, N.D. Chaudhari, S.R. Sawant, J. Magn. Magn. Mater. 186 (1998) 349–356.

[87] U.V. Chhaya, B.S. Trivedi, R.G. Kulkarni, J. Phys. B 262 (1999) 5-12.

[88] Lawrence Kumar, Manoranjan Kar, J. Magn. Magn. Mater. 323 (2011) 2042-2048

[89] I. H. Gul, A. Maqsood, M. Naeem, M. Naeem Ashiq, J. Alloy. Compd. 507 (2010) 201-206

[90] D.R. Mane, Swati Patil, D.D. Birajdar, A.B. Kadam, Sagar E. Shirsath, R.H. Kadam, Mater. Chem. Phys.126 (2011) 755–760

[91] A.A. Birajdar, Sagar E. Shirsath, R.H. Kadam, S.M. Patange, D.R. Mane, A.R. Shitre, Ceram. Intern. 8 (2012) 2963

[92] A. M. Gismelseed, A. A. Yousif, Physica B 370 (2005) 215.

[93] S. M. Patange, Sagar E. Shirsath, B. G. Toksha, S. S. Jadhav, K. M. Jadhav, J. Appl. Phys.106 (2009) 023914.

[94] S. H. Lee, S. J. Yoon, G. J. Lee, H. S. Kim, C. H. Yo, K. Ahn, D. H. Lee, K. H. Kim, Mater. Chem. Phys. 61 (1999) 147.

[95] Yen-Pei Fu, Mater. Res. Bull. 41 (2006) 809.

[96] V.M. Nanoti, D.K. Kulkarni, Mater. Lett. 33 (1997) 37

[97] R. H. Kadam, A. R. Biradar, M. L. Mane, Sagar E. Shirsath, J. Appl. Phys. 112 (2012) 043902

[98] Q. Song, Y. Ding, Z. L. Wang, Z. J. Zhang, Chem. Mater. 19 (2007) 4633-4638

[99] D. Carta, M. F. Casula, P. Floris, A. Falqui, G. Mountjoy, A. Boni, C. Sangregorio and A. Corrias, Phys. Chem. Chem. Phys. 12 (2010) 5074-5083

[100] S. Matzen,J. B. Moussy, R.Mattana, K.Bouzehouane, C.Deranlot, F.Petroff, J. C.Cezar, M. A.Arrio, Ph. Sainctavit, C. Gatel, B. Warot-Fonrose,Y. Zheng, Phys. Rev. B 83 (2011) 184402.

[101] A. J. Rondinone, C. Liu, Z. J. Zhang, J. Phys. Chem. B 105 (2001) 7967-7971

Chapter 2

Crystal structure and properties of ferrites

2.1 Spinel compounds

2.1.1 Introduction to spinel compounds

The word spinel is derived from Italian *spinella*, diminutive of spine, thorn(from its sharply pointed crystals). Spinel crystallizes in the cubic system, forming octahedral crystals. There are at least 30 oxide minerals included in spinel supergroup. The majority of spinel compounds belong to the space group Fd3m. The principal member of the group has the formula, AB_2O_4; the '*A*' represents a divalent metal ion such as magnesium, iron, nickel, manganese and zinc. The quadrovalent lead ion can also occupy this site. The '*B*' represents trivalent metal ions such as aluminum, iron, chromium and/or manganese. However, titanium Ti^{4+} and Pb^{2+} etc.may also occupy this site. Solid solutioning is common in this group of minerals meaning that they may contain certain percentages of different ions in any particular specimen [1]. In most oxide structures, the oxygen ions are appreciably larger than the metallic ions and the spinel structure can be approximated by a cubic close packing of O^{2-} ions in which the cations (e.g. Co^{2+}, Fe^{3+}) occupy certain interstices.

The structure of a spinel compound is similar to the highly symmetric structure of diamond. The position of the *A* ions is nearly identical to the positions occupied by carbon atoms in the diamond structure. This could explain the relatively high hardness and high density typical of this group. The arrangement of the other ions in the structure conforms to the symmetry of the diamond structure. The arrangement of the ions also favors the octahedral crystal structure, which is the predominant crystal form and is in fact the trademark of the spinels. There are well over a hundred compounds with the spinel structure reported to date. Most are oxides, some are sulphides, selenides and tellurides and few are halides. Many different cations may be introduced into the spinel structure and several different charge combinations are possible;

almost any combination that adds up to eight positive charges to balance eight anionic charges [1], for example $Co^{2+}Fe_2^{3+}O_4$,$Mg_2^{2+}Ti^{4+}O_4$, $Li^{1+}Al^{3+}Ti^{4+}O_4$, $Li_{0.5}^{1+}Al_{2.5}^{3+}O_4$ and $Na_2^{1+}W^{6+}O_4$, etc.

In oxide spinels, the two types of cations do not usually differ greatly in size, because the spinel structure is stable only if the cations are rather medium sized and, in addition, the radii of the different ionic species in the same compound do not differ too much. Similar cation combinations occur in sulphides, e.g. $Zn^{2+}Al_2^{3+}S_4$ and $Cu_2^{2+}Sn^{4+}S_4$. However, in halide spinels e.g. $Li_2^{1+}Ni^{3+}F_4$ and $Li^{1+}Mn_2^{3+/4+}F_4$, cations are limited to charges of +1 and +2, in order to give an overall cation: anion ratio of 3:4.

Most spinels fall into three series determined by a B metal: aluminate series with Al^{3+} (Hercynite, Gahnite, Galaxite); a magnetite series with Fe^{3+} (Magnetite, Magnesio ferrite, Franklinite); a chromite series with Cr^{3+} (Chromite,Magnesio chromite). There is extensive cationic exchange (solid solution) within each series but very little between the series [2]. Spinels are classified on the basis of the distribution of cations in the two principal sites, tetrahedral site (T-) and octahedral site (O-) [3], into three types.

2.1.2 Types of spinel

The spinels are any of a class of minerals of general formulation $A^{2+}B_2^{3+}O_4^{2-}$ which crystallise in the cubic (isometric) crystal system, with the oxide anions arranged in a cubic packed lattice and the cations A and B occupying some or all of the octahedral and tetrahedral sites in the lattice. A and B can be divalent, trivalent, or quadrivalent cations, including magnesium, zinc, iron, manganese, aluminium, chromium, titanium, and silicon. Although the anion is normally oxide, structures are also known for the rest of the chalcogenides. A and B can also be the same metal under different charges, such as the case in Fe_3O_4 (as $Fe^{2+}Fe_2^{3+}O_4^{2-}$).

Members of the spinel group include:

☐ Aluminium spinels:
  - ✓ Spinel – $MgAl_2O_4$, after which this class of minerals is named
  - ✓ Gahnite- $ZnAl_2O_4$

  - ✓ Hercynite - $FeAl_2O_4$
- ☐ Iron spinels:
  - ✓ Cuprospinel - $CuFe_2O_4$
  - ✓ Franklinite - $(Fe,Mn,Zn)(Fe,Mn)_2O_4$
  - ✓ Jacobsite - $MnFe_2O_4$
  - ✓ Magnetite - Fe_3O_4
  - ✓ Trevorite - $NiFe_2O_4$
  - ✓ Ulvöspinel - $TiFe_2O_4$
  - ✓ Zinc ferrite - $(Zn, Fe) Fe_2O_4$
- ☐ Chromium spinels:
  - ✓ Chromite - $FeCr_2O_4$
  - ✓ Magnesiochromite - $MgCr_2O_4$
- ☐ Others with the spinel structure:
  - ✓ Forsterite - Mg_2SiO_4
  - ✓ Ring woodite - $(Mg,Fe)_2SiO_4$, an abundant olivine polymorph within the Earth's mantle from about 520 to 660 km depth, and a rare mineral in meteorites

Cation disorder in multi-site oxides is quantified in terms of an "inversion parameter" (δ). The spinel structure is cubic, with two distinct cation sites characterized by different oxygen coordination (octahedral and tetrahedral). There are twice as many octahedral sites as tetrahedral sites.

Normal spinel:

The cation disorder is defined in terms of a "normal" spinel structure, such as that for ideal $MgAl_2O_4$, in which all the Mg resides on sites tetrahedrally coordinated with oxygen, and all the Al resides on sites octahedrally coordinated with oxygen. The inversion parameter is defined relative to this configuration, and is the ratio of the atomic fraction of Al on tetrahedral sites to the atomic fraction of Al on octahedral sites. For a perfect normal spinel, the inversion parameter is 0.0. Normal spinel structures are usually cubic closed-packed oxides with one octahedral and two tetrahedral sites per oxide. The tetrahedral points are smaller than the octahedral points.

B^{3+} ions occupy the octahedral holes because of a charge factor, but can only occupy half of the octahedral holes. A^{2+} ions occupy 1/8th of the tetrahedral holes. This maximises the lattice energy if the ions are similar in size. A common example of a normal spinel is $MgAl_2O_4$.

Inverse spinel:

For an ideal "inverse" spinel structure (such as for $MgFe_2O_4$), all of the Mg resides on octahedral sites, and the Fe is distributed equally over the remaining octahedral sites and all of the tetrahedral sites. In this case the inversion parameter would be 1.0. Inverse spinel structures however are slightly different in that one must take into account the crystal field stabilization energies (CFSE) of the transition metals present. Some ions may have a distinct preference on the octahedral site which is dependent on the d-electron count. If the A^{2+} ions have a strong preference for the octahedral site, they will force their way into it and displace half of the B^{3+} ions from the octahedral sites to the tetrahedral sites. If the B^{3+} ions have a low or zero octahedral site stabilization energy (OSSE), then they have no preference and will adopt the tetrahedral site. A common example of an inverse spinel is Fe_3O_4, if the Fe^{2+} (A^{2+}) ions are d^6 high-spin and the Fe^{3+} (B^{3+}) ions are d^5 high-spin.

Random spinel:

For a "random" spinel structure, the cations are equally distributed over the two sites in ratios proportional to their stoichiometry and the site ratios. A random spinel structure has an inversion parameter of (2/3), or 0.667. In spinel ferrites if the divalent metal ions and trivalent Fe^{3+} ions are distributed randomly over the tetrahedral and octahedral B-sites, then the spinel ferrite is called random spinel.

A whole range of possible distribution is observed. This can be represented in general terms by

$$(\mathrm{Me}^{\mathrm{II}}_{\delta}\,\mathrm{Fe}^{\mathrm{III}}_{1-\delta})^{A}\,[\mathrm{Me}^{\mathrm{II}}_{1-\delta}\,\mathrm{Fe}^{\mathrm{III}}_{1+\delta}]^{B}\,\mathrm{O}_4^{2-}\,.$$

where the ions inside the bracket are located in octahedral sites and the ions outside the brackets in tetrahedral sites.

2.2 Chemical composition of spinel ferrite

Complex oxides with the spinel structure often called “spinels” belong to the group of strategic materials which are used in the wide area of modern technologies. They exhibit excellent magnetic, refractory, semi conducting, catalytic and sorptionproperties.The general chemical formula of ferrites possessing the structure of the mineral spinel, $MeAl_2O_4$, is $MeFe_2O_4$, where Me represents a divalent metal ion with an ionic radius approximately between 0.6 and 1Å. In the case of simple ferrites, Me is one of the transition elements Mn, Fe, Co, Ni, Cu and Zn, or Mg and Cd. A combination of these ions is also possible, a mixed ferrite. The symbol Me can represent a combination of ions which have an average valency of two e.g. Li^{1+} and Fe^{3+} in lithium ferrite, $Li_{0.5}Fe_{2.5}O_4$.The trivalent iron ions ($Fe^{3+)}$ in $MeFe_2O_4$ can be completely or partly replaced by another trivalent ion such as Al^{3+} or Cr^{3+}, giving rise to mixed crystals with aluminates and chromites. These compounds are also ferrimagnetic at room temperature if large amount of non-magnetic ions are not present. If the ferric ions are replaced by a tetravalent ion like Ti^{4+}, an equal part of the Fe^{3+} are changed into Fe^{2+}.A great variety of the chemical composition of ferrimagnetic oxide with spinel structure is possible.

2.3 Crystal structure of ferrite

2.3.1 Spinel ferrite

Spinel ferrite crystallizes in the cubic structure. The spinel lattice is composed of a close-packed oxygen anions arrangement in which 32 oxygen ions form the unit cell (the smallest repeating unit in the crystal network). These anions are packed in a face centered cubic (FCC) arrangement leaving two kinds of spaces between anions:tetrahedrally coordinated sites (A), surrounded by four nearest oxygen atoms, and octahedrally coordinated sites (B), surrounded by six nearest neighbor oxygen atoms (Figure 2.1). There are total 64 tetrahedral sites and 32 octahedral sites in the unit cell, of which only 8 tetrahedral sites and 16 octahedral sites are occupied, resulting in a structure that is electrically neutral [4].

Spinels have general formula $M(Fe_2O_4)$, where M is usually a divalent cation such as manganese (Mn^{2+}), nickel (Ni^{2+}), cobalt (Co^{2+}), zinc (Zn^{2+}), copper (Cu^{2+}), or magnesium (Mg^{2+}). M can also represent the mono valent lithium cation (Li^+) or even vacancies, as long as these absences of positive charge are compensated for by additional trivalent iron cations (Fe^{3+}). The ionic distribution in this kind of structure may be represented by $[M_\delta Fe_{1-\delta}]^A[M_{1-\delta}Fe_{1+\delta}]^BO_4$, where δ is the inversion parameter and $\delta = 0$ and 1 stand for the inverse and normal cases respectively.

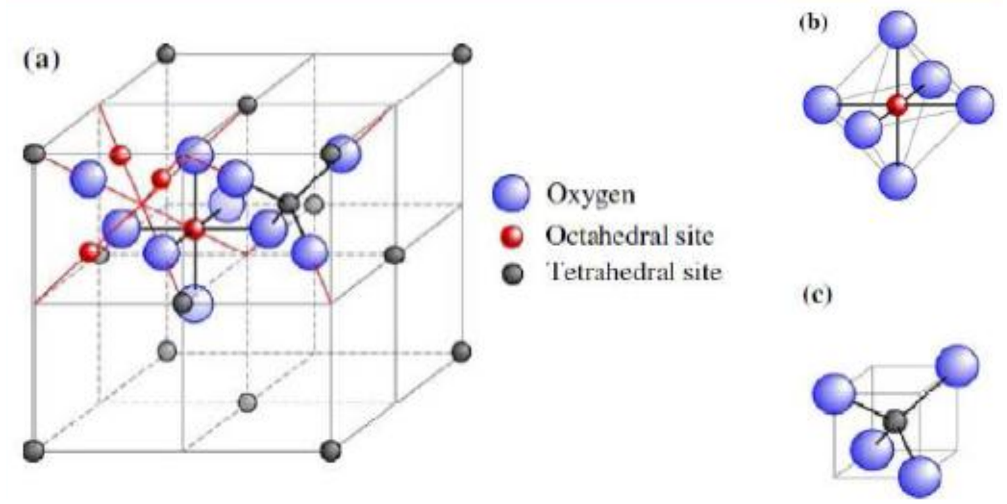

Fig. 2.1: (a) Spinel structure, (b) octahedral interstice (B site: 32 per unit cell,16 occupied), and (c) tetrahedral interstice (A site: 64 per unit cell, 8 occupied).

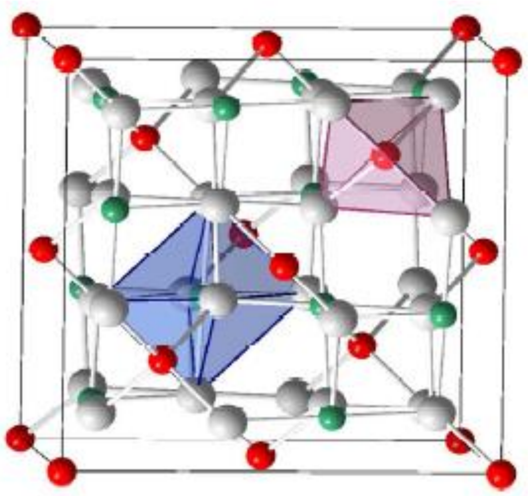

Fig. 2.2: Spinel unit cell structure

Although most spinel ferrites are cubic, there are some exceptions like $CuFe_2O_4$ that can have tetragonal unit cell symmetry if the sample is slowly cooled from high temperatures. There exists a super exchange interaction between the cations occupied in different interstitial sites through oxygen anion.

2.3.2 Garnet structure

The garnets have orthorhombic crystal structure (oxygen polyhedra, surrounding the cations) but with trivalent cations (including rare earth and Fe^{3+}) occupying tetrahedral (d), octahedral (a), or dodecahedral—a 12-sided distorted polyhedral—(c) sites. Specifically, the interaction between tetrahedral and octahedral sites is anti parallel, and the net magnetic moment is anti parallel to the rare earth ions on the c sites. The garnet structure is one of the most complicated crystal structures and it is difficult to draw a two dimensional representation that shows clearly all the ions (160) in the unit cell. For simplicity, only an octant of a garnet structure that shows just the cation positions is shown in Fig. 2.3. The garnet structure is composed of a combination of octahedral (trivalent cation surrounded by six oxygen ions), tetrahedral (trivalent cations surrounded by four oxygen ions), and 12-sidedpolyhedral - dodecahedral - (trivalent cations surrounded by 8 oxygen atoms) sites,the orientations of which are shown in Fig. 2.4 (a) [5]. The chemical formula for garnets is $3Me_2O_3 \cdot 5Fe_2O_3$ where Me represents the trivalent rare earth ions like nonmagnetic yttrium or a magnetic rare earth such as from lanthanum through ytterbium.

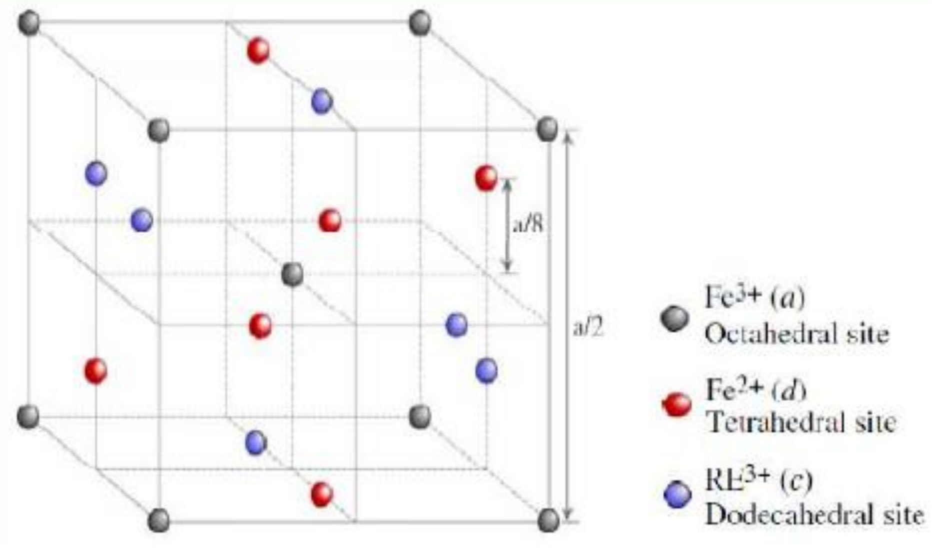

Fig. 2.3: Schematic representation of an 'octant' of a garnet crystal structure(lattice constant 'a') showing cation positions.

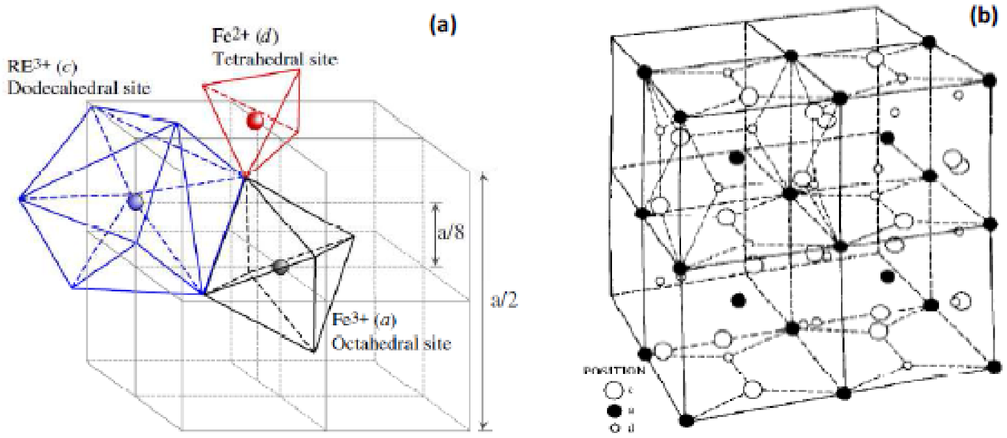

Fig. 2.4: (a) An 'octant' of a garnet crystal structure (b) Unit cell of a rare earth garnet.

Fig. 2.4 (b) shows a unit cell of rare earth garnet. In YIG, the five iron (III)ions occupy two octahedral and three tetrahedral sites, with the yttrium (III) ions coordinated by eight oxygen ions in an irregular cube. The iron ions in the two coordination sites exhibit different spins, resulting in magnetic behavior. By substituting specific sites with rare earth elements, interesting magnetic properties can be obtained. Trivalent iron ions on Tetrahedral (d) and Octahedral (a) are important for magnetic property. These two sites are coupled anti-ferromagnetically [6] and yields a Ferrimagnetic crystal [7].

2.3.3 Ortho ferrite

Rare earth ortho ferrites are classified as ferrites, although they are cantedantiferromagnets. The magnetic oxides with perovskite structure, which have been studied by Jonker and Van Santen [8], are an exception in the group of oxides. The perovskite structure is shown schematically in Fig. 2.5. Large divalent or trivalent ions (A) occupy the corners of a cube and small trivalent or tetravalent metal ions (B)occupy the centre of the cube. The oxygen ions are situated centrally on the faces of the cube. The general chemical formula is ABO3, where A represents yttrium or a rare earth.

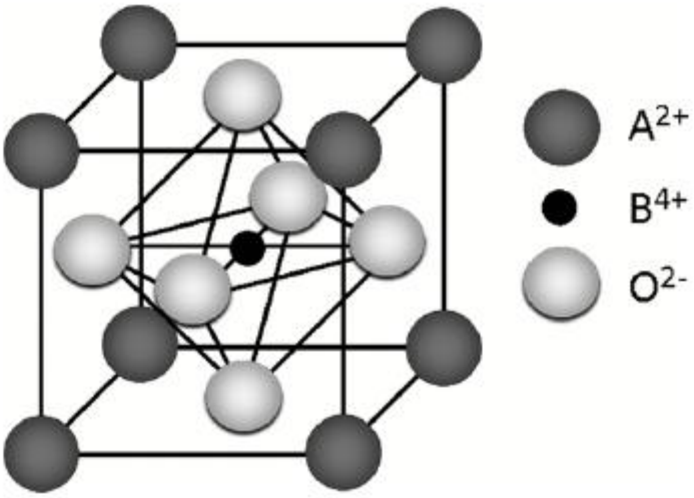

Fig. 2.5: A Perovskite structure of an orthoferrite

The magnetic structure inside of a sublattice is usually collinear ferromagnetic, but the different sub lattices are coupled antiferromagnetically. Due to the different number of magnetic ions in different sublattices, there is a net resulting magnetic moment, giving rise to ferrimagnetism. The nature of the superexchangeinteraction depends not only on the type of the magnetic ion, but rather strongly on the bond length and bonding angle.

2.3.4 Hexagonal ferrite

The regular barium hexaferrite has the crystal structure of the mineral magnet oplumbite, as shown in Fig. 2.6. It belongs to the group of hexagonal ferrite of the so-called M-type. The crystallographic unit cell corresponds to the space group $P6_3/mmc$ and contains two molecules of the chemical composition

$BaFe_{12}O_{19}$. The dimensions of the unit cell are approximately a = b =6Å and c = 23 Å.

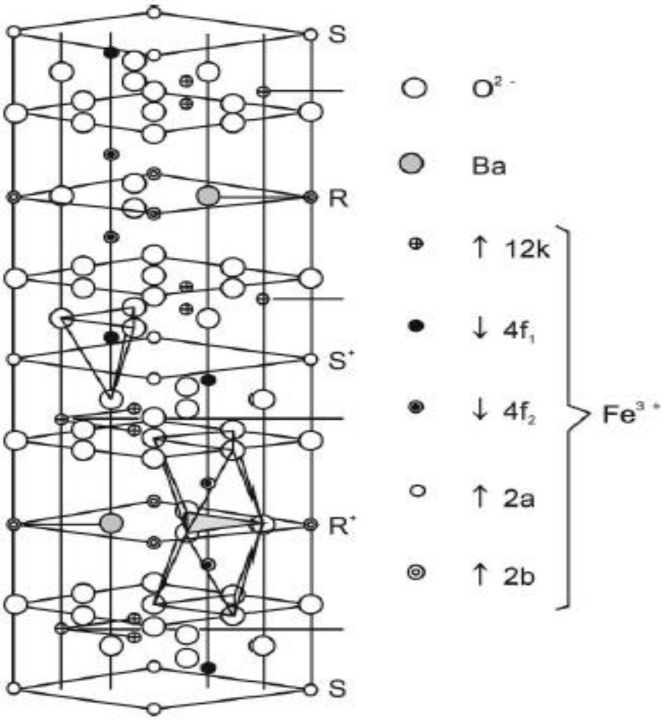

Fig. 2.6: Unit cell of barium hexaferrite based on two cells of $BaFe_{12}O_{19}$.

The basic structure of the unit cell is built up by ten layers of oxygen ions which are formed by a close packing of cubic or hexagonal stacked layers alternately. One O^{2-}ion is replaced by barium in every fifth layer (Fig. 2.6).

The crystal structure of M-type barium can be divided into several blocks. The structure of M-type barium ferrite is symbolically described as RSR*S*, where R is a one-layer block with composition $Ba^{2+}Fe_3^{3+}O_3^{2-}$ and S is a four O^{4-} layers block with composition $Fe_9^{3+}O_{16}^{2-}$, where the asterisk means that the corresponding block has been turned 180° around the hexagonal c-axis. All the metal ions are arranged in the interstices of oxygen atom. There are five Fe sites: two ions have tetrahedral surroundings ($4f_1$), and one Fe ion is located in a trigonal bipyramid (2b) with five-fold coordination [9] three octahedral positions (2a, $4f_1$ and 12k) are occupied by one, two and six Fe ions, respectively, as shown in Fig. 2.7.

According to Fig. 2.7, it can also be seen that Fe^{3+} ions with up-spin are distributed on the 2a, 2b and 12k sites and the ions with down-spin are located on the $4f_1$ and $4f_2$ sites. Due to antiparallel spin direction of ions, the magnetic moment can be expressed as following:

$$M=12k+2a+2b+4f_1+4f_2 \quad 2.1$$

According to Eq. (2.1), the more Fe^{3+} ions with up-spin exist, the larger magnetization will be. But, the excessive displacements of Fe ions will destroy the matching distribution of Fe ions between A site (tetrahedral positions) and B site (octahedral positions), which will weaken the super exchange interactions.

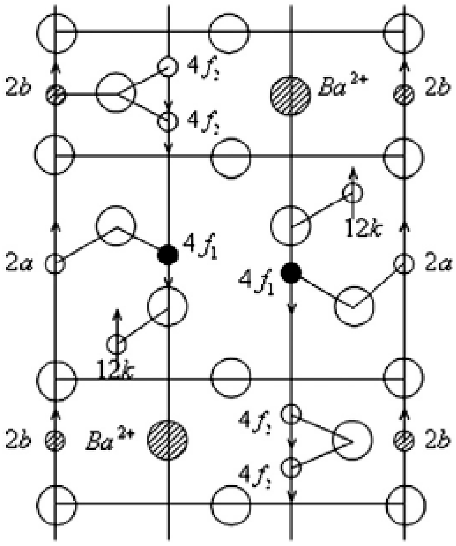

Fig. 2.7: The magnetic structure of Barium hexaferrite.

2.4 Cation distribution in spinel ferrite

2.4.1 Ionic radius

Since the tetrahedral site is the smaller, one might expect that the smaller ions will prefer to occupy the tetrahedral sites. Trivalent ions are usually smaller than the divalent ions and this favours the inverse structure.

2.4.2 Electronic configuration

Certain ions have special preference for a certain environment. For example ,Zn^{2+} and Cd^{2+} show a marked preference for tetrahedral sites where their *4s, p* or *5s, p* electrons respectively can form a covalent bond with the six

2p electrons of the oxygen ion. This produces four bonds oriented towards the corner of a tetrahedron. A marked preference of Ni^{2+}, Co^{2+} and Cr^{3+} for octahedral environment is due to favorable fit of the charge distribution of these ions in the crystal field at an octahedral site [10].

2.4.3 Electrostatic energy

The electrostatic energy is gained when the ions are brought close together to form the spinel cubic lattice from infinity. In the normal spinel, the cation with the smallest positive charge is surrounded by four oxygen atoms while the cation with the higher positive charge by six oxygen atoms, being electrostatically more favorable. In the spinels the inverse structure is electrostatically more favorable and has the lowest energy when the oxygen parameter value (u) is smaller than the normal value (u =0.379) while normal spinel has the lowest energy when 'u' is larger than the normal[10].

2.5 Magnetic properties

Magnetic material exhibits different kind of magnetic ordering depending upon spin orientation. The magnetic behaviour is caused by spinning of electrons of 'd' orbital about their own axis gives rise to spin magnetic moments. The motion of electron in the orbit around the nucleus results in orbital magnetic moments. In case of transition element, this orbital magnetic moments get quenched by crystalline electrical field. The different magnetic behaviour observed is due to different contribution of electron spin.

2.5.1 Classification of magnetic properties

On the basis of electron spin magnetism is classified in number of classes as diamagnetism, paramagnetism, ferromagnetism, anti-ferromagnetism and ferrimagnetism.

1) Diamagnetism

Diamagnetism is a fundamental property of all matter, although it is usually very weak. It is due to the non-cooperative behavior of orbiting electrons when exposed to an applied magnetic field. Diamagnetic substances are composed of atoms which have no net magnetic moments (i.e., all the orbital shells are filled and there are no unpaired electrons). However, when exposed to a field, a negative magnetization is produced and thus the susceptibility is negative. If we plot M vs H, we see (Fig. 2.8):

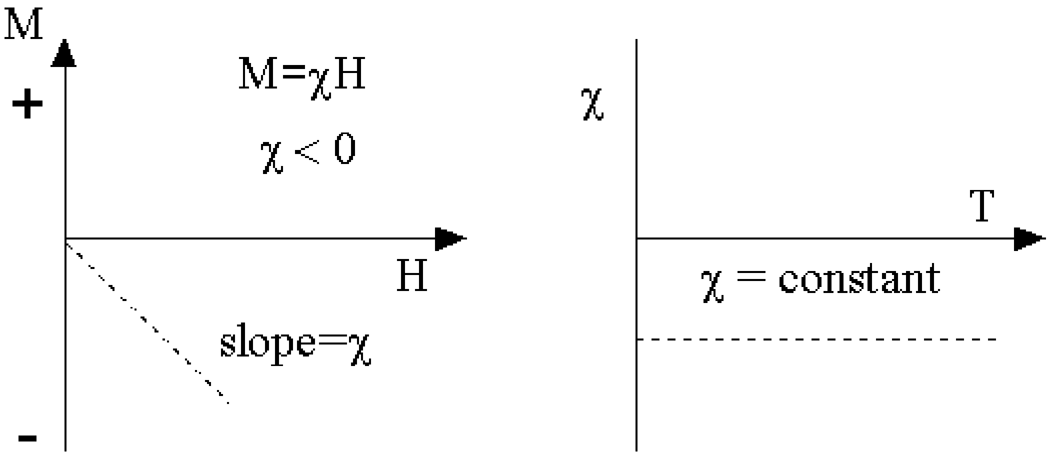

Fig. 2.8: M-H plot of diamagnetic material

When the field is zero the magnetization is zero. The other characteristic behavior of diamagnetic materials is that the susceptibility is temperature independent.

2) Paramagnetism:

This class of materials, some of the atoms or ions in the material have a net magnetic moment due to unpaired electrons in partially filled orbitals. One of the most important atoms with unpaired electrons is iron. However, the individual magnetic moments do not interact magnetically, and like diamagnetism, the magnetization is zero when the field is removed. In the presence of a field, there is now a partial alignment of the atomic magnetic moments in the direction of the field, resulting in a net positive magnetization and positive susceptibility.

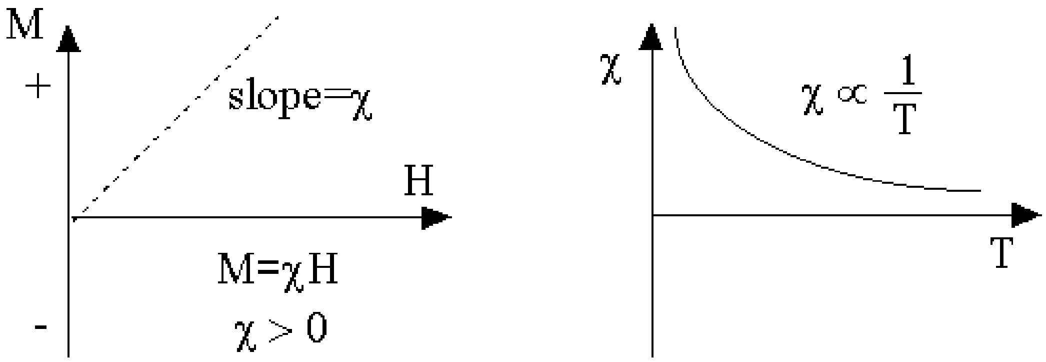

Fig. 2.9:M-H plot of paramagnetic material

In addition, the efficiency of the field in aligning the moments is opposed by the randomizing effects of temperature. This results in a temperature dependent susceptibility, known as the Curie Law.At normal temperatures and in moderate fields, the paramagnetic susceptibility is small (but larger than the diamagnetic contribution). Unless the temperature is very low (<<100 K) or the field is very high paramagnetic susceptibility is independent of the applied field. Under these conditions, paramagnetic susceptibility is proportional to the total iron content.

3) Ferromagnetism

Unlike paramagnetic materials, the atomic moments in these materials exhibit very strong interactions. These interactions are produced by electronic exchange forces and result in a parallel or antiparallel alignment of atomic moments. Exchange forces are very large, equivalent to a field on the order of 1000 Tesla, or approximately a 100 million times the strength of the earth's field. The exchange force is a quantum mechanical phenomenon due to the relative orientation of the spins of two electron. Ferromagnetic materials exhibit parallel alignment of moments resulting in large net magnetization even in the absence of a magnetic field.

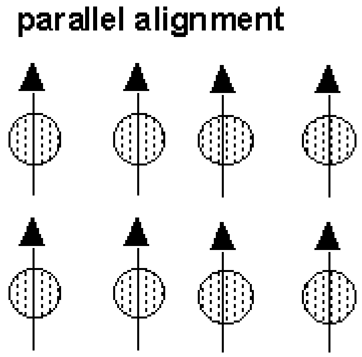

Fig. 2.10: Spin alignment in ferromagnetic material

Two distinct characteristics of ferromagnetic materials are their

(1) spontaneous magnetization and the existence of

(2) magnetic ordering temperature

Spontaneous Magnetization

The spontaneous magnetization is the net magnetization that exists inside a uniformly magnetized microscopic volume in the absence of a field. The magnitude of this magnetization, at 0 K, is dependent on the spin magnetic moments of electrons. A related term is the saturation magnetization which we can measure in the laboratory. The saturation magnetization is the maximum induced magnetic moment that can be obtained in a magnetic field (H_{sat}); beyond this field no further increase in magnetization occurs. The difference between spontaneous magnetization and the saturation magnetization has to do with magnetic domains (more about domains later). Saturation magnetization is an intrinsic property, independent of particle size but dependent on temperature. There is a big difference between paramagnetic and ferromagnetic susceptibility. As compared to paramagnetic materials, the magnetization in ferromagnetic materials is saturated in moderate magnetic fields and at high (room-temperature) temperatures:

4) Ferrimagnetism

In ionic compounds, such as oxides, more complex forms of magnetic ordering can occur as a result of the crystal structure. One type of magnetic ordering is call ferrimagnetism. A simple representation of the magnetic spins in a ferrimagnetic oxide is shown here. The magnetic structure is composed of two magnetic sub lattices (called A and B) separated by oxygens. The exchange interactions are mediated by the oxygen anions. When this happens, the interactions are called indirect or super exchange interactions. The strongest super exchange interactions result in an anti parallel alignment of spins between the A and B sublattice.In ferrimagnets, the magnetic moments of the A and B sub lattices are not equal and result in a net magnetic moment. Ferrimagnetism is therefore similar to ferromagnetism. It exhibits all the hallmarks of ferromagnetic behavior- spontaneous magnetization, Curie temperatures, hysteresis, and remanence. However, ferro- and ferrimagnets have very different magnetic ordering. Magnetite is a well-known ferrimagnetic material. Indeed, magnetite was considered a ferromagnet until Néel in the 1940's, provided the theoretical framework for understanding ferrimagnetism.

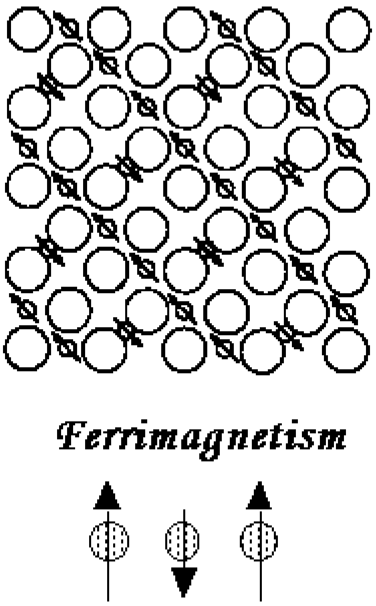

Fig. 2.11: Spin alignment in ferrimagnetic materials

2.5.2 Magnetization

The magnetization is a powerful tool to study the different parameters such as domain wall rotation, anisotropy, magnetic hardness or softness of material, magnetic ordering etc. Ferrites exhibit almost all the properties similar to that of ferromagnetic materials. When the magnetic field is applied to the ferromagnetic material, the magnetization may vary from zero to saturation value. This behaviour is expressed by Weiss [11] by introducing the idea of existence of domains. According to Weiss, though each domain is spontaneously magnetized in the direction of field, magnetization may vary from one domain to another domain. In general, specimen consists of many domains, in domain configuration i.e. a function of applied field. The magnetic moment of specimen is a vector sum of magnetic moment of each domain. As a result the magnetization or average magnetic moment per unit volume may have value between zero to saturation.

Studies on magnetic hysteresis of ferrite provide useful information of the magnetic parameter like saturation magnetization (Ms) coercive force (H_C) and remanence ratio (Mr/Ms). According to the values of these parameters, the ferrites can be classified as soft and hard ferrites. The ferrites with low coercive force are called soft ferrites and ferrites with high Hc are called hard ferrites. Soft ferrites are those material which do not retain permanent magnetism, which provide easy magnetic path. Hard ferrites retain permanent magnetism and are difficult to magnetize and demagnetize. According to Neel [12] the coercive force (H_C) is related to saturation magnetization, internal stress, porosity [13] and anisotropy [14]. The Hysteresis properties are highly sensitive to crystal structure, heat treatment, chemical composition, porosity and grain size.

2.5.3 Hysteresis

The lag or delay of a magnetic material known commonly as magnetic hysteresis, relates to the magnetisation properties of a material by which it firstly becomes magnetised and then de-magnetised. The magnetic flux generated by an electromagnetic coil is the amount of magnetic field or lines of force produced within a given area and that it is more commonly called "Flux Density". Given the symbol B with the unit of flux density being the Tesla, T.

The magnetic strength of an electromagnet depends upon the number of turns of the coil, the current flowing through the coil or the type of core material being used, and if we increase either the current or the number of turns we can increase the magnetic field strength, symbol H.

The relative permeability, symbol μ_r was defined as the product of the absolute permeability μ and the permeability of free space μ_o (a vacuum) and this was given as a constant. However, the relationship between the flux density, B and the magnetic field strength, H can be defined by the fact that the relative permeability, μ_r is not a constant but a function of the magnetic field intensity thereby giving magnetic flux density as: $B = \mu H$. Then the magnetic flux density in the material will be increased by a larger factor as a result of its relative permeability for the material compared to the magnetic flux density in vacuum, $\mu_o H$ and for an air-cored coil this relationship is given as:

$B = \Phi/A$ and $\mu 0 = B/H$

So for ferromagnetic materials the ratio of flux density to field strength (B/H) is not constant but varies with flux density. However, for air cored coils or any non-magnetic medium core such as woods or plastics, this ratio can be considered as a constant and this constant is known as μ_o, the permeability of free space, ($\mu_o = 4.\pi.10^{-7}$ H/m).

The magnetic hysteresis loop (Fig. 2.12), shows the behavior of a ferromagnetic core graphically as the relationship between B and H is non-linear. Starting with an unmagnetised core both B and H will be at zero, point 0 on the magnetisation curve.

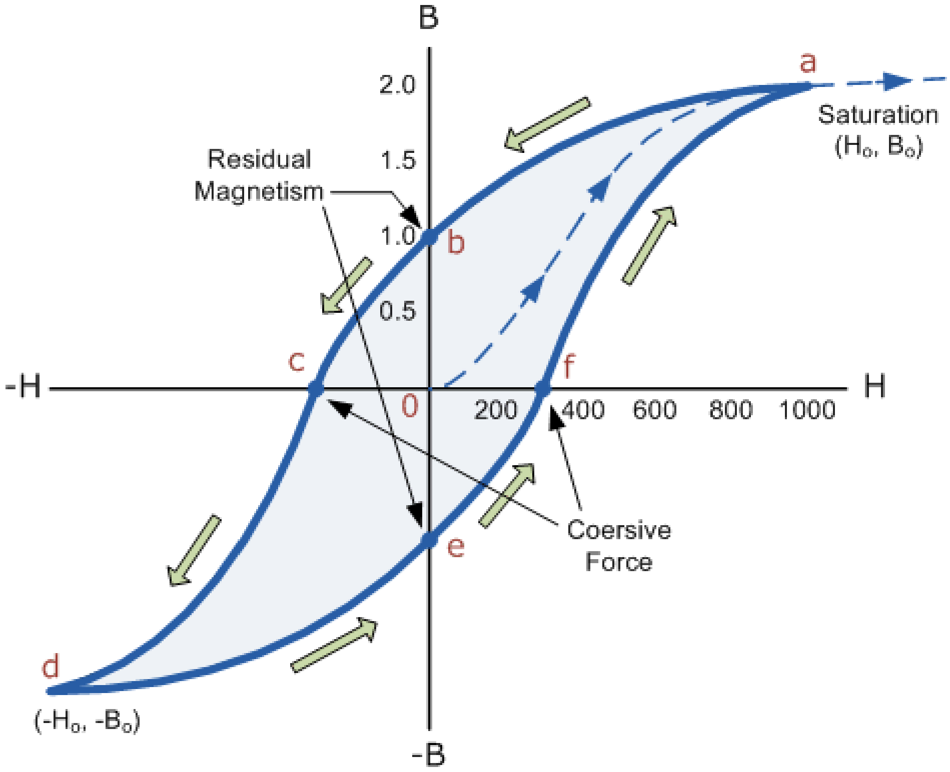

Fig. 2.12: Magnetic hysteresis loop

If the magnetisation current, i is increased in a positive direction to some value the magnetic field strength H increases linearly with i and the flux density B will also increase as shown by the curve from point 0 to point a as it heads towards saturation. Now if the magnetising current in the coil is reduced to zero the magnetic field around the core reduces to zero but the magnetic flux does not reach zero due to the residual magnetism present within the core and this is shown on the curve from point a to point b.To reduce the flux density at point b to zero we need to reverse the current flowing through the coil. The magnetising force which must be applied to null the residual flux density is called a "Coercive Force". This coercive force reverses the magnetic field re-arranging the molecular magnets until the core becomes unmagnetised at point c. An increase in the reverse current causes the core to be magnetised in the opposite direction and increasing this magnetisation current will cause the core to reach saturation but in the opposite direction, point d on the cure which is symmetrical to point b. If the magnetising current is reduced again to zero the residual magnetism present in the core will be equal to the previous value but in reverse at point e.

Again reversing the magnetising current flowing through the coil this time into a positive direction will cause the magnetic flux to reach zero, point f on the curve and as before increasing the magnetisation current further in a positive direction will cause the core to reach saturation at point a. Then the B-H curve follows the path of a-b-c-d-e-f-a as the magnetising current flowing through the coil alternates between a positive and negative value such as the cycle of an AC voltage. This path is called a magnetic hysteresis loop.

The effect of magnetic hysteresis shows that the magnetisation process of a ferromagnetic core and therefore the flux density depends on which part of the curve the ferromagnetic core is magnetised on as this depends upon the circuits past history giving the core a form of "memory". Then ferromagnetic materials have memory because they remain magnetised after the external magnetic field has been removed. However, soft ferromagnetic materials such as iron or silicon steel have very narrow magnetic hysteresis loops resulting in very small amounts of residual magnetism making them ideal for use in relays, solenoids and transformers as they can be easily magnetised and demagnetised. Since a coercive force must be applied to overcome this residual magnetism, work must be done in closing the hysteresis loop with the energy being used being dissipated as heat in the magnetic material. This heat is known as hysteresis loss, the amount of loss depends on the material's value of coercive force. By adding addictive's to the iron metal such as silicon, materials with a very small coercive force can be made that have a very narrow hysteresis loop. Materials with narrow hysteresis loops are easily magnetised and demagnetised and known as soft magnetic materials.

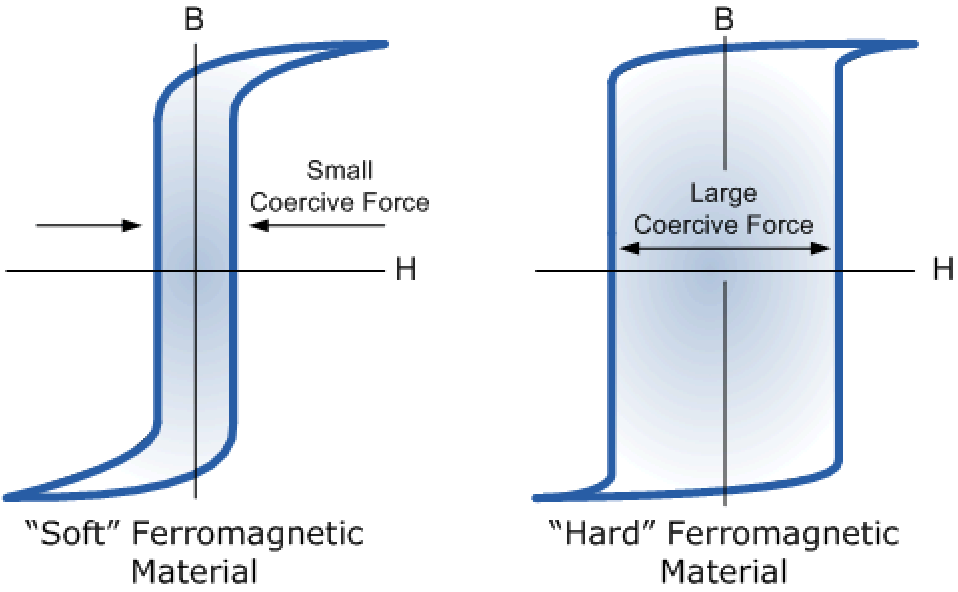

Fig. 2.13: Hysteresis loops of soft and hard magnetic material

Magnetic hysteresis results in the dissipation of wasted energy in the form of heat with the energy wasted being in proportion to the area of the magnetic hysteresis loop. Hysteresis losses will always be a problem in AC transformers where the current is constantly changing direction and thus the magnetic poles in the core will cause losses because they constantly reverse direction.Rotating coils in DC machines will also incur hysteresis losses as they are alternately passing north the south magnetic poles. The shape of the hysteresis loop depends upon the nature of the iron or steel used and in the case of iron which is subjected to massive reversals of magnetism, for example transformer cores, it is important that the B-H hysteresis loop is as small as possible.

2.5.4 Exchange interactions

Magnetism in transition metal oxides is observed to be rather complex than that of individual isolated atoms because of the presence of coupling of atomic moments. This coupling of moments is responsible for cooperative nature of magnetism in transition metal oxides. The statistical correlation for electrons of likes pin, with each surrounded by a void due to local depletion of parallel spin electrons, is called exchange. There exist three types of magnetic interactions direct exchange, double exchange and super-exchange.

2.5.4.1 Direct exchange interaction

When the individual moments are located close enough to allow sufficient overlap of their wave functions, the direct exchange can occur. In such conditions minimum Coulomb's interactions will be experienced when electrons are located between the nuclei. The electrons in such a condition should have opposite spins which results in anti-ferromagnetism. While ferromagnetism is observed when the moments are arranged parallel to each other, which is possible only when the electrons are located far from one another. Such a magnetic dipole-dipole interaction would be too small by a factor at least 103 to explain the observed Curie temperatures. The interaction can be explained on the basis of an exchange force, which is quantum mechanical in origin; according to Heisenberg. The exchange energy Eexbetween two atoms having spins Si and $Sj$is given simply by

$$\begin{aligned} Eex &= -2Jex\, S_i \cdot S_j \\ &= -2Jex\, Si\, .Sj\cos\theta \qquad (2.2) \end{aligned}$$

Where $Jex$is called exchange integral which occurs in the calculation of the exchange effect and it is a measure of the extent to which the electronic charge distributions of the two atoms concerned overlap one another, and θ is the angle between the spins. If Jexhas a positive value then the exchange energy $Eex$is minimum when electron spins are parallel i.e., $\theta = 0$ (ferromagnetism). If Jexhas negative value, then $Eex$is minimum when electron spins are anti-parallel; i.e., $\theta = 180^o$(antiferromagnetism).

2.5.4.2 Super-exchange interaction

The oxide ion has a very small interaction magnitude with metallic ions in its ground state because of a completely filled 2p orbital. The super exchange interaction has been proposed for the case in which there is a mechanism of excitation from this ground state as the interaction can only take place in the excited state with the metallic ion. The possible excitation mechanism involves the temporary transfer of one oxide *2p* electron to a neighboring metal ion. Qualitatively we can describe the superexchange interaction by considering the following example of ferric ions in an oxide (Fig 2.5). We go from a ground state of these ferric ions in which the five *3d*electrons according to Hand's rule are all aligned parallel to each other. The six *2p*electrons of the oxygen ion form three pairs. The spin of electrons in each of these pairs is paired and they reside in a dumb-bell shape *p*-orbital. In an excited state the electron from the nearby oxide ion leaves the *p*-orbital and becomes (temporarily) part of Fe^{3+} ion, which becomes Fe^{2+} on gaining Néel electron. The transfer process in which we have one Fe^{3+} ion on one side of the oxygen and another Fe^{3+} ion on the other side is given as shown in (Figure 2.14).

The one Fe^{3+} ion now becomes a Fe^{2+} ion. The unpaired electron of the oxygen *p* orbital which was directed toward the Fe^{3+} ions now can interact with theFe^{3+} ion present on the opposite side.

$Fe^{3+}(3d^5)$	$O^{2-}(2p^6)$	$Fe^{3+}(3d^5)$	→	$Fe^{3+}(3d^5)$	$O^{1-}(2p^5)$	$Fe^{2+}(3d^6)$
↓↓↓↓↓	↑↓	↓↓↓↓↓		↓↓↓↓↓	↑↓	↓↓↓↓↓
	↑↓				↑↓	↑
	↑↓				↓	

Fig.2.14. Super-exchange Interactions [15]

The overall coupling between the cationsdepends on a combination of direct exchange, excitation and intra-atomic (Hund'sRule) coupling, and is known as super exchange. If the *3d* orbital of the metal ions are less than half full, the super exchange should favour a positive interaction; for *3d*shells which are half filled or more than half filled, e.g. Fe^{3+} ion, a negative interaction with anti-parallel spin is probable. It is generally assumed that this super exchange interaction diminishes rapidly as the distance between the ions increases. The dumbbell shape of the *2p* orbital makes it reasonable to assume that the interaction for a given ionic separation is greatest when the metal oxygen-metal angle is 180° and is least when this angle is 90°. Thus in a spinel lattice the *A* interaction is relatively strong, the *A-A*interaction is relatively weak and the *B-B*interaction is probably intermediate [15].

2.5.5 Magnetic anisotropy

In most magnetic materials, to varying degree, the magnetization tends to align itself along one of the main crystal directions. That direction is called the easy direction of magnetization. All ferromagnetic and ferrimagnetic materials possess, to a lesser or greater degree, a crystal direction or a set of directions in which the magnetization prefers to be oriented [16].

This magnetic anisotropy can have various causes. The most important in magnetic materials are the shape and magneto crystalline anisotropies. Shape anisotropy is associated with the geometrical shape of a magnetized body, and refers to the preference that the polarization in a long body is for the direction of the major axis. The magneto crystalline anisotropy is associated with the crystal symmetry of thematerial. There are three situations that give rise to this anisotropy as an intrinsic crystal property. The first and most important one is that in which the atoms possess an electron-orbital moment in addition to an electron-spin moment. In such a situation the spin direction may be coupled to the crystal axis. This arises through the coupling between spin and orbital moments and the interaction between the charge distribution over the orbit and the electrostatic field of the surrounding atoms. There will then be one or more axes or surfaces along which magnetization requires relatively little work. The crystal will then be preferentially magnetized along such an easy axis or plane.he second situation is encountered in non-cubic crystal lattices. In these crystals the magneto-static interaction between the atomic moments is also anisotropic, which may give rise to easy directions or planes of magnetization. The third possibility of crystal anisotropy is found in the directional ordering of atoms as described by Néel [12]. This typically involves solid solutions of atoms of two kinds, A and B, linked by the atomic bonds *A-A*, *A-B* and *B-B*. In the presence of a strong external magnetic field the internal energy of these bonds may be to some extent direction-dependent. Given a sufficient degree of atomic diffusion-as a result of raising the temperature, for example-a certain ordering can be brought about in the distribution of the bonds; in this way it is possible to "bake" the direction of this field into the material as the easy axis of magnetization. In addition to these sources of magnet to crystalline anisotropy mechanical stresses may contribute through the magneto-elastic (magneto-strictive) properties ofthe crystal. This contribution, however, is considered to be negligible in hard magnetic materials [16].

2.6 Neel's theory

Neither ferromagnetism nor antiferromagnetism could explain the magnetic behavior of ferrite Material. If the situation is assumed as ferromagnetic, one Fe^{++} and the two Fe^{+++} ions per molecule were lined up parallel to one another would give 14 μ_B per molecule but the experimental value comes around 4.2 μ_B. To explain this observed behavior Neel assumed that a ferrimagnetic crystal lattice could be divided into two sub lattice such as would be formed by the A (tetrahedral) and B (octahedral) sites in the spinel structure [12]. He supposed the existence in the material of one type of magnetic ion only, of which a fraction λ appeared on A site and a fraction μ on B-sites. Thus,

$$\lambda + \mu = 1 \qquad 2.3$$

The remaining occupied lattice sites were assumed to have only ions of zero magnetic moment. Considering a simple ferrite of the form MFe_2O_4, which satisfies Neel`s assumption, the magnetic ions are trivalent ferric Fe^{3+}, M is non-magnetic and the formula might be written as,

$$Fe_{2\lambda}M_{(1-2\lambda)}[Fe_{2-2\lambda}M_{2\lambda}]\,O_4 \quad \text{or}$$

$$Fe_{2\lambda}M_{(1-2\lambda)}[Fe_{2\mu}M_{2\lambda}]\,O_4$$

Where the bracketed ions are those on the octahedral sites.

Since an A- ion has near neighbors of both A and B types, as has a B-ion, there are several interactions between magnetic ion to be considered and these may be classified as A-A, B-B, A-B and B-A (where A-A refers the interaction of an ion on an A site with its neighbors also on A site, with similar definitions of the other terms). In the Neel theory it is assumed that the A-B, B-A interactions are identical and predominant over A-A, B-B interactions, and are such as to favor the alignment of the magnetic moment of each A- on more or less anti-parallel with the moment of each B-ion. Thus, for the ferrite considered above, assuming each ferric ion to have a movement of 5 Bohr magnet on (μ_B), the moment of the ferrite "molecule" would be $2(\lambda-\mu)5\mu_B$ instead $2(\lambda+\mu)5\mu_B$, which would occur with parallel orientation of all the moments. The Neel theory predicts magnetic moments which may be much smaller than the sum of the moments of the constituent ions. This is experimentally observed. Clearly Neel's assumption that only one type of magnetic ion is present will rarely be met, but it has been found that the general features of ferrites may be adequately represented on the Neel model, with suitable qualitative modifications.

Neel defined the interactions within the material from the Weiss molecular field view point. The magnetic field action upon an ion is written in the form

$$H = H_0 + H_m \qquad 2.4$$

Where H_0 is the externally applied field andH_m is the internal or molecular field which arises due to interactions with other atoms or ions within the material.

When the molecular field concept is applied to a ferrimagnetic material, we have,

$$H_A = H_{AA} + H_{AB} \qquad 2.5$$

$$H_B = H_{BB} + H_{BA} \qquad 2.6$$

Here, the molecular field H_A acting on an ion on A-site is represented as the sum of the molecular field H_{AA} due to neighbouring A-sites, and H_{AB} due to its neighbours on B-Sites. A similar definition holds for the molecular field H_B, acting on a B-ion. The molecular field components may then be written as,

$$H_{AA} = \gamma_{AA} M_{A}, \quad H_{AB} = \gamma_{AB} M_{B} \qquad 2.7$$

$$H_{BB} = \gamma_{BB} M_{B}, H_{BA} = \gamma_{BA} M_{A} \qquad 2.8$$

where, the γ'sare the appropriate molecular coefficients and M_A, M_B are the magnetic moments of the A and B sub-lattices. It may be shown that,

$\gamma_{BA} = \gamma_{AB}$, but $\gamma_{AA} \neq \gamma_{BB}$,

Unless the two sub lattices were identical. Neel showed that $\gamma_{AB} < 0$, favouring anti parallel arrangement of M_A and M_B, gives rise to ferrimagnetism.

In the presence of an applied field H_O, the total magnetic fields acting on each sub lattice may be written, using equations (2.5) and (2.8)

$$H_a = H_o + H_A = H_o + \gamma_{AA} M_A + \gamma_{AB} M_B \qquad 2.9$$

$$H_b = H_o + H_B = H_o + \gamma_{BB} M_B + \gamma_{AB} M_A \qquad 2.10$$

2.7 Yafet-Kittel theory

Experimentally it is observed that the saturation magnetization of a ferrite initially increases up to certain value and then decreases rapidly. Neel's model successfully explains the initial rise in saturation magnetization, but fails to explain the further decrease in it. This discrepancy between observed and calculated values of saturation magnetization can be explained by Yafet-Kittel model. According to Yafet Kittel model, in spinel ferrites, nonmagnetic substitution in one sub-lattice could lead to non-collinear or canted spin arrangement. It is possible only if A-B magnetic interaction is equal to or smaller than that of A-A and B-B interactions. When non-magnetic ion like Zn^{2+} and Cd^{2+} is substituted in spinel ferrite the B sub-lattice splits into B_1 and B_2 with equal magnetic moments with an angle θ_{YK} with the direction of net magnetization of B sub-lattices at 0K. To calculate the uniform canting angle θ_{yk} a split sub-lattice model was developed by Yafet-Kittel.

Yafet-Kittel model can be understood from $Ni_{1-x}Zn_xFe_2O_4$ ferrite system. For pure nickel ferrite ($NiFe_2O_4$) the A-B interaction is dominant. As Zn concentration (x) is increased, magnetic moment on A site decreases to zero. The B-B interaction will give rise to anti-ferromagnetic order in B sub-lattice with Zn concentration, and then the intermediate arrangement is expected. At a particular value of (x), the A-A interaction and B-B interaction are comparable. The B-B interaction arranges magnetic moments on B lattice in anti-parallel direction whereas A-B interaction arranges them in parallel direction on B site. This leads to a canted spin arrangement on B-site. The Yafet-Kittel model splits B sub-lattice into B_1 and B_2 sub-lattices each making an angle θ_{yk} with the direction of net magnetization of B sub-lattices. The moment on B site is anti-parallel to moment on A site. The net magnetic moment for the system can be expressed as

$$\mu_{(x)} = M_B \mathrm{Cos}\theta_{YK} - M_A \quad 2.11$$

Where M_A is magnetic moment on A site, M_B is magnetic moment on B site.

References

[1] D. M. Smyth, the Defect Chemistry of Metal Oxides; Oxford University Press: New York, 2000.

[2] R. J. King, *Geology Today*, 2004, *20*, 194.

[3] A. R. West, *Solid State Chemistry and its Applications*; John Wiley & Sons: Singapore, 1989.

[4] A. Goldman, Modern Ferrite Technology, Van No strand Reinhold, New York, 1990.

[5] S. Geller, M. A. Gilleo, J. Phys. Chem. Solids, 3 (1957) 30.

[6] K. Enke, J. Fleischhauer, W. Gunser, P. Hansen, S. Nomura, W. Tolksdorf, G.Winkler, U. Wolfmeier, Garnets and Perovskites, Landolt-Bornstein, New series III/12a, 1978.

[7] H. Dotsch, N. Bahlmann, O. Zhuromskyy, M. Hammer, L. Wilkens, R. Gerhardt,P. Hertel, A. F. Popkov, J. Opt. Soc. Am. B, 22-1 (2005) 240.

[8] G. H. Jonker, J. H. Van Santen, Physica, 16 (1950) 337.

[9] J.M. Williams, J. Adetunji, M. Gregori, J. Magn. Magn.Mater. 220 (2000) 124.

[10] J.Smit, H. P. J. Wijn, *Ferrites-Physical Properties of Ferrimagnetic Oxides inRelation to their Technical Applications,* John Wiley and Sons, The Netherlands,1959.

[11] P. Weiss, J. Phys. 6 (1907) 667.

[12] L.Néel, Adv. Phys. 4 (1955) 191.

[13] C.M. Srivastava, M.J. Patani and T.T. Srinivasan, J. Appl. Phys. 53 (1983) 2107.

[14] A.M. Alpr, “High temperature oxides” Academic Press, New York, 25 (1971).

[15] K. J.Standley, Oxide Magn. Mater.Oxford University Press, London, 1962.

[16] D. J. Craik, (Ed.), Magnetic Oxides, John Willey and Sons, London, 1975.

Chapter 3

Preparation and characterization

3.1 Synthesis method

3.1.1 Solid state reaction

The most common method of preparing metal oxides and other solid materials is by the ceramic method which involves grinding powders oxides, carbonates, oxalates or other compounds containing the relevant metals and heating the mixture at a desired temperature. Several oxides, sulphides, phosphides etc. have been prepared by this technique. The most common method of preparing metal oxides and other solid materials is by the ceramic method .In the ceramic method very pure and fine grains constituents in oxide forms are taken. Then they are thoroughly and uniformly mixed. This mixture is sintered for prolonged time at specific temperature so as to facilitate solid-state chemical reaction among the oxides and the formation of chemical compound. Pre-sintering of the samples can be done at about 900°C and final sintering of the ferrite sample can be done at above 1200°C depending on the constituents.

3.1.2 Hydrothermal synthesis

Hydrothermal synthesis includes the various techniques of crystallizing substances from high-temperature aqueous solutions at high vapor pressures; also termed "hydrothermal method". The term "hydrothermal" is of geologic origin. Geochemists and mineralogists have studied hydrothermal phase equilibria since the beginning of the 20th century. George W. Morey at the Carnegie Institution and later, Percy W. Bridgman at Harvard University did much of the work to lay the foundations necessary to containment of reactive media in the temperature and pressure range where most of the hydrothermal work is conducted.

Hydrothermal synthesis can be defined as a method of synthesis of single crystals that depends on the solubility of minerals in hot water under high pressure. The crystal growth is performed in an apparatus consisting of a steel pressure vessel called an autoclave, in which a nutrient is supplied along with water. A temperature gradient is maintained between the opposite ends of the growth chamber. At the hotter end the nutrient solute dissolves, while at the cooler end it is deposited on a seed crystal, growing the desired crystal.

Possible advantages of the hydrothermal method over other types of crystal growth include the ability to create crystalline phases which are not stable at the melting point. Also, materials which have a high vapour pressure near their melting points can also be grown by the hydrothermal method. The method is also particularly suitable for the growth of large good-quality crystals while maintaining good control over their composition. Disadvantages of the method include the need of expensive autoclaves, and the impossibility of observing the crystal as it grows.

3.1.3 Micro emulsions synthesis

Micro emulsions are clear, thermodynamically stable, isotropic liquid mixtures of oil, water and surfactant, frequently in combination with a cosurfactant. The aqueous phase may contain salt(s) or other ingredients, and the "oil" may actually be a complex mixture of different hydrocarbons and olefins. In contrast to ordinary emulsions, micro emulsions form upon simple mixing of the components and do not require the high shear conditions generally used in the formation of ordinary emulsions. The three basic types of micro emulsions are direct (oil dispersed in water, o/w), reversed (water dispersed in oil, w/o) and bicontinuous.

In ternary systems such as micro emulsions, where two immiscible phases (water and 'oil') are present with a surfactant, the surfactant molecules may form a monolayer at the interface between the oil and water, with the hydrophobic tails of the surfactant molecules dissolved in the oil phase and the hydrophilic head groups in the aqueous phase

Much of the work done on these systems have been motivated by their possible use to mobilize petroleum trapped in porous sandstone for enhanced oil recovery A fundamental reason for the uses of these systems is that a micro emulsion phase sometimes has an ultra low interfacial tension with a separate oil or aqueous phase, which may release or mobilize them from solid phases even in conditions of slow flow or low pressure gradients. Microemulsions also have industrial applications, one of them being the synthesis of polymers. Microemulsion polymerization is a complex heterogeneous process where transport of monomers, free radicals and other species (such as chain transfer agent, co-surfactant and inhibitors) between the aqueous and organic phases, takes place. Compared with other heterogeneous polymerization processes (suspension or emulsion) microemulsion polymerization is a more complicated system. Polymerization rate is controlled by monomer partitioning between the phases, particle nucleation, and adsorption and desorption of radicals. Particle stability is affected by the amount and type of surfactant and pH of dispersing medium. It is also used in the process of creating nano particles. The kinetics of microemulsion polymerization has much in common with emulsion polymerization kinetics, the most characteristic feature of which is the compartmentalization, where the radicals growing inside the particles are separated from each other, thus suppressing termination to a high extent and, as a consequence, providing high rates of polymerization.

3.1.4 Citrate precursor synthesis

In the citrate precursor technique, the individual cations in the stoichio metric ratio are reacted with the poly functional organic acid, citric acid under controlled pH conditions to obtain a precursor at an atomic level bending of the constituent elements in the required stoichiometric ratio is achieved during the reaction in the solution state to form the citrate complex.

This precursor on proper thermal decomposition at right temperatures indicated by thermal analysis data loses all the organic moiety to give rise to the final ternary oxide It is important to note that the diffusion controlled solid state reaction between constituent compounds involved in ceramic method and co-precipitation method is not present in the precursor method. The final reaction is the decomposition process and it depend on the decomposition temperature of the precursor. The citrate precursors decompose at temperature less than 700°C and hence it has been possible to prepare barium hexaferrite and series of rare earth garnet at these relatively low temperatures [18].

Therefore in principle, if one can prepare precursor complexes using organic completing materials other than citrates, which decompose at lower temperatures than citrate, It may be possible to further reduce the preparation temperature .Lowering of preparation temperature will be extremely useful from the point of view of producing nano particles of the hexaferrite system.

3.1.5 Spray pyrolysis technique

The ferrite thin films can be prepared by spray pyrolysis technique using a citrate complex precursor. The preparation essentially consists of two stages, namely, the preparation of the citrate complex precursor and spray deposition of the "films using the precursor solution. At first aqueous solutions of stoichio metric amounts of nitrates of Ba and Fe were prepared. These solutions were reacted with 1:1 molar ratio of citric acid under controlled pH conditions. The reaction takes place in a slightly alkaline solution. Ammonia solution was added drop by drop to the reaction mixture with constant stirring until the desired pH is obtained. This solution was then refluxed for 6 h under controlled pH condition for completion of the reaction to form the citrate complex precursor. The preparation of the citrate complex is a crucial step in obtaining homogeneous single-phase films. Once the right complex was formed, ternary oxide phase could be obtained at relatively low temperatures by thermal decomposition of the complex at appropriate temperatures. Diluted precursor solution was sprayed onto the cleaned quartz plates previously heated to 350-400°C, using a sprayer and dry nitrogen as carrier gas. A highly adherent and homogeneous film of barium ferrite was formed by pyrolytic decomposition of sprayed precursor. For crystallization the films were annealed in a tubular furnace at a temperature ±70°C for about 3 h in air.

3.1.6. Co-precipitation technique

In chemistry, coprecipitation (CPT) or co-precipitation is the carrying down by a precipitate of substances normally soluble under the conditions employed. Analogously, in medicine, coprecipitation is specifically the precipitation of an unbound "antigen along with an antigen-antibody complex".Coprecipitation is an important issue in chemical analysis, where it is often undesirable, but in some cases it can be exploited. In gravimetric analysis, which consists on precipitating the analyte and measuring its mass to determine its concentration or purity, coprecipitation is a problem because undesired impurities often coprecipitate with the analyte, resulting in excess mass. This problem can often be mitigated by "digestion" (waiting for the precipitate to equilibrate and form larger, purer particles) or by redissolving the sample and precipitating it again.

On the other hand, in the analysis of trace elements, as is often the case in radiochemistry, coprecipitation is often the only way of separating an element. Since the trace element is too dilute (sometimes less than parts per trillion) to precipitate by conventional means, it is typically coprecipitated with a carrier, a substance that has a similar crystalline structure that can incorporate the desired element. An example is the separation of francium from other radioactive elements by coprecipitating it with caesium salts such as caesium perchlorate. Otto Hahn is credited for promoting the use of co precipitation in radiochemistry. There are three main mechanisms of co precipitation: inclusion, occlusion, and adsorption. An inclusion occurs when the impurity occupies a lattice site in the crystal structure of the carrier, resulting in a crystallographic defect; this can happen when the ionic radius and charge of the impurity are similar to those of the carrier. An adsorbate is an impurity that is weakly bound (adsorbed) to the surface of the precipitate. An occlusion occurs when an adsorbed impurity gets physically trapped inside the crystal as it grows. Besides its applications in chemical analysis and in radiochemistry, co precipitation is also "potentially important to many environmental issues closely related to water resources, including acid mine drainage, radionuclide migration in fouled waste repositories, metal contaminant transport at industrial and defense sites, metal concentrations in aquatic systems, and wastewater treatment technology". Co-precipitation is mainly used as a method of magnetic nano particle synthesis.

3.1.7 Sol-gel synthesis

In materials science, the sol-gel process is a method for producing solid materials from small molecules. The method is used for the fabrication of metal oxides, especially the oxides of silicon and titanium. The process involves conversion of monomers into a colloidal solution (sol) that acts as the precursor for an integrated network (or gel) of either discrete particles or network polymers.

The sol-gel process may be described as: Formation of an oxide network through polycondensation reactions of a molecular precursor in a liquid. A sol is a stable dispersion of colloidal particles or polymers in a solvent. The particles may be amorphous or crystalline. An aerosol is particles in a gas phase, while a sol is particles in a liquid, A gel consists of a three dimensional continuous network, which encloses a liquid phase, in a colloidal gel, the network is built from agglomeration of colloidal particles. In a polymer gel the particles have a polymeric sub-structure made by aggregates of sub-colloidal particles. Generally, the sol particles may interact by van der Wails forces or hydrogen bonds. A gel may also be formed from linking polymer chains. In most gel systems used for materials synthesis, the interactions are of a covalent nature and the gel process is irreversible. The gelation process may be reversible if other interactions are involved.

In this chemical procedure, the 'sol' (or solution) gradually evolves towards the formation of a gel-like diphasic system containing both a liquid phase and solid phase whose morphologies range from discrete particles to continuous polymer networks. In the case of the colloid, the volume fraction of particles (or particle density) may be so low that a significant amount of fluid may need to be removed initially for the gel-like properties to be recognized. This can be accomplished in any number of ways. The simplest method is to allow time for sedimentation to occur, and then pour off the remaining liquid. Centrifugation can also be used to accelerate the process of phase separation.

Removal of the remaining liquid (solvent) phase requires a drying process, which is typically accompanied by a significant amount of shrinkage and densification. The rate at which the solvent can be removed is ultimately determined by the distribution of porosity in the gel. The ultimate microstructure of the final component will clearly be strongly influenced by changes imposed upon the structural template during this phase of processing.

Afterwards, a thermal treatment, or firing process, is often necessary in order to favor further polycondensation and enhance mechanical properties and structural stability via final sintering, densification and grain growth. One of the distinct advantages of using this methodology as opposed to the more traditional processing techniques is that densification is often achieved at a much lower temperature.

The precursor sol can be either deposited on a substrate to form a film (e.g., by dip coating or spin coating), cast into a suitable container with the desired shape (e.g., to obtain monolithic ceramics, glasses, fibers, membranes, aerogels), or used to synthesize powders (e.g., microspheres, nanospheres). The sol-gel approach is a cheap and low-temperature technique that allows for the fine control of the product’s chemical composition. Even small quantities of do pants, such as organic dyes and rare earth elements, can be introduced in the sol and end up uniformly dispersed in the final product. It can be used in ceramics processing and manufacturing as an investment casting material, or as a means of producing very thin films of metal oxides for various purposes. Sol-gel derived materials have diverse applications in optics, electronics, energy, space, (bio) sensors, medicine (e.g., controlled drug release), reactive material and separation (e.g., chromatography) technology.

The interest in sol-gel processing can be traced back in the mid-1800s with the observation that the hydrolysis of tetraethyl or thosilicate (TEOS) under acidic conditions led to the formation of SiO_2 in the form of fibers and monoliths. Sol-gel research grew to be so important that in the 1990s more than 35,000 papers were published worldwide on the process.

The sol-gel process is a wet-chemical technique used for the fabrication of both glassy and ceramic materials. In this process, the sol (or solution) evolves gradually towards the formation of a gel-like network containing both a liquid phase and a solid phase. Typical precursors are metal alkoxides and metal chlorides, which undergo hydrolysis and polycondensation reactions to form a colloid. The basic structure or morphology of the solid phase can range anywhere from discrete colloidal particles to continuous chain-like polymer networks.

The term colloid is used primarily to describe a broad range of solid-liquid (and/or liquid-liquid) mixtures, all of which contain distinct solid (and/or liquid) particles which are dispersed to various degrees in a liquid medium. The term is specific to the size of the individual particles, which are larger than atomic dimensions but small enough to exhibit Brownian motion. If the particles are large enough, then their dynamic behavior in any given period of time in suspension would be governed by forces of gravity and sedimentation. But if they are small enough to be colloids, then their irregular motion in suspension can be attributed to the collective bombardment of a myriad of thermally agitated molecules in the liquid suspending medium, as described originally by Albert Einstein in his dissertation. Einstein concluded that this erratic behavior could adequately be described using the theory of Brownian motion, with sedimentation being a possible long term result. This critical size range (or particle diameter) typically ranges from tens of angstroms (10−10 m) to a few micrometres (10−6 m).

Under certain chemical conditions (typically in base-catalyzed sols), the particles may grow to sufficient size to become colloids, which are affected both by sedimentation and forces of gravity. Stabilized suspensions of such sub-micrometre spherical particles may eventually result in their self-assembly yielding highly ordered microstructures reminiscent of the prototype colloidal crystal: precious opal. Under certain chemical conditions (typically in acid-catalyzed sols), the interparticle forces have sufficient strength to cause considerable aggregation and/or flocculation prior to their growth. The formation of a more open continuous network of low density polymers exhibits certain advantages with regard to physical properties in the formation of high performance glass and glass/ceramic components in 2 and 3 dimensions.In either case (discrete particles or continuous polymer network) the sol evolves then towards the formation of an inorganic network containing a liquid phase (gel). Formation of a metal oxide involves connecting the metal centers with oxo (M-O-M) or hydroxo (M-OH-M) bridges, therefore generating metal-oxo or metal-hydroxo polymers in solution.In both cases (discrete particles or continuous polymer network), the drying process serves to remove the liquid phase from the gel, yielding a micro-porous amorphous glass or micro-crystalline ceramic. Subsequent thermal treatment (firing) may be performed in order to favor further polycondensation and enhance mechanical properties.With the viscosity of a sol adjusted into a proper range, both optical quality glass fiber and refractory ceramic fiber can be drawn which are used for fiber optic sensors and thermal insulation, respectively. In addition, uniform ceramic powders of a wide range of chemical composition can be formed by precipitation.

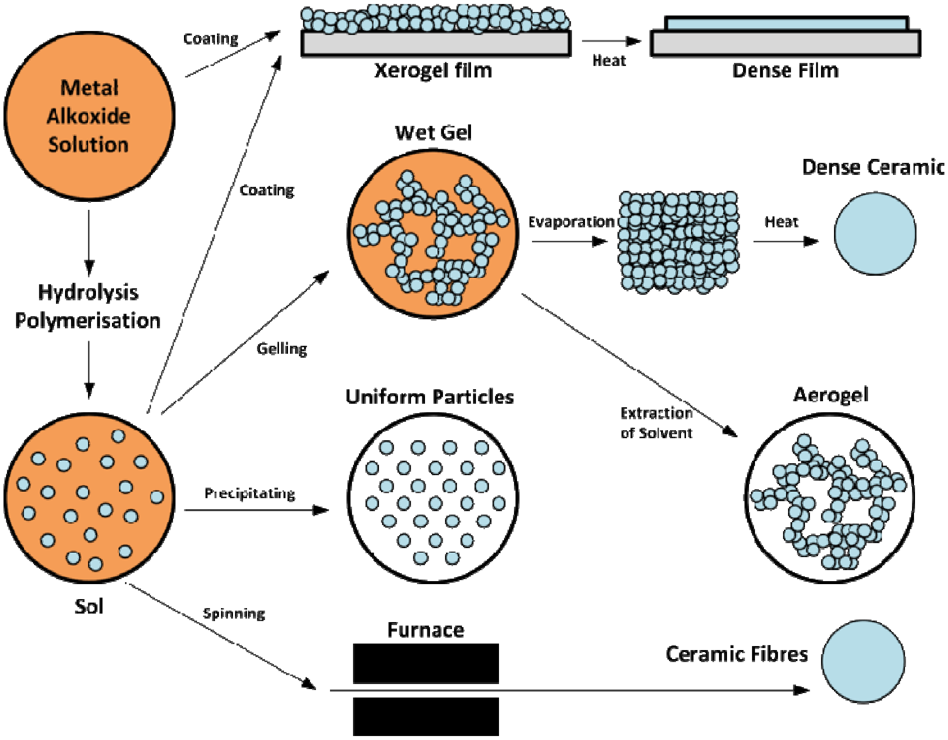

Fig. 3.1: Schematic representation of the different stages and routes of the sol-gel technology.

In the processing of fine ceramics, the irregular particle sizes and shapes in a typical powder often lead to non-uniform packing morphologies that result in packing density variations in the powder compact. Uncontrolled flocculation of powders due to attractive Vander Walls forces can also give rise to microstructural in homogeneities.

Differential stresses that develop as a result of non-uniform drying shrinkage are directly related to the rate at which the solvent can be removed, and thus highly dependent upon the distribution of porosity. Such stresses have been associated with a plastic-to-brittle transition in consolidated bodies, and can yield to crack propagation in the unfired body if not relieved.

In addition, any fluctuations in packing density in the compact as it is prepared for the kiln are often amplified during the sintering process, yielding inhomogeneous densification. Some pores and other structural defects associated with density variations have been shown to play a detrimental role in the sintering process by growing and thus limiting end-point densities. Differential stresses arising from inhomogeneous densification have also been shown to result in the propagation of internal cracks, thus becoming the strength-controlling flaws.

It would therefore appear desirable to process a material in such a way that it is physically uniform with regard to the distribution of components and porosity, rather than using particle size distributions which will maximize the green density. The containment of a uniformly dispersed assembly of strongly interacting particles in suspension requires total control over particle-particle interactions. Monodisperse colloids provide this potential.

Monodisperse powders of colloidal silica, for example, may therefore be stabilized sufficiently to ensure a high degree of order in the colloidal crystal or polycrystalline colloidal solid which results from aggregation. The degree of order appears to be limited by the time and space allowed for longer-range correlations to be established. Such defective polycrystalline structures would appear to be the basic elements of nano scale materials science, and, therefore, provide the first step in developing a more rigorous understanding of the mechanisms involved in micro structural evolution in inorganic systems such as sintered ceramic nano materials.

3.2 Characterization techniques

3.2.1 X-ray diffraction

A) Crystallography:

X-ray crystallography is a tool used for determining the atomic and molecular structure of a crystal, in which the crystalline atoms cause a beam of X-rays to diffract into many specific directions. By measuring the angles and intensities of these diffracted beams, a crystallographer can produce a three-dimensional picture of the density of electrons within the crystal. From this electron density, the mean positions of the atoms in the crystal can be determined, as well as their chemical bonds, their disorder and various other information.

Since many materials can form crystals such as salts, metals, minerals, semiconductors, as well as various inorganic, organic and biological molecules.

X-ray crystallography has been fundamental in the development of many scientific fields. In its first decades of use, this method determined the size of atoms, the lengths and types of chemical bonds, and the atomic-scale differences among various materials, especially minerals and alloys. The method also revealed the structure and function of many biological molecules, including vitamins, drugs, proteins and nucleic acids such as DNA. X-ray crystallography is still the chief method for characterizing the atomic structure of new materials and in discerning materials that appear similar by other experiments. X-ray crystal structures can also account for unusual electronic or elastic properties of a material, shed light on chemical interactions and processes, or serve as the basis for designing pharmaceuticals against diseases.

In an X-ray diffraction measurement, a crystal is mounted on a goniometer and gradually rotated while being bombarded with X-rays, producing a diffraction pattern of regularly spaced spots known as reflections. The two-dimensional images taken at different rotations are converted into a three-dimensional model of the density of electrons within the crystal using the mathematical method of Fourier transforms, combined with chemical data known for the sample. Poor resolution (fuzziness) or even errors may result if the crystals are too small, or not uniform enough in their internal makeup.

X-ray crystallography is related to several other methods for determining atomic structures. Similar diffraction patterns can be produced by scattering electrons or neutrons, which are likewise interpreted as a Fourier transform. If single crystals of sufficient size cannot be obtained, various other X-ray methods can be applied to obtain less detailed information; such methods include fiber diffraction, powder diffraction and small-angle X-ray scattering (SAXS). If the material under investigation is only available in the form of nano crystalline powders or suffers from poor crystallinity, the methods of electron crystallography can be applied for determining the atomic structure.

For all above mentioned X-ray diffraction methods, the scattering is elastic; the scattered X-rays have the same wavelength as the incoming X-ray. By contrast, inelastic X-ray scattering methods are useful in studying excitations of the sample, rather than the distribution of its atoms

B) Principle of technique

X-rays are electromagnetic radiation with wavelengths in the range 0.5-2.5 °A. Since this is of the same order of magnitude as the interatomic distances in solids, X-rays are frequently used to study the internal (crystalline) structure of materials. An X-ray beam impinging on a crystal will be scattered in all directions by the atoms of the crystal. In some directions, an increased intensity is observed due to the constructive interference of the scattered waves.

The conditions for constructive interference are easily derived from the simple geometrical picture for the scattering of an X-ray beam by planes of atoms in a crystal, shown in Fig. 3.2. Imagine the X-ray beam of wavelength λ, incident on the crystal at an angle θ with respect to equidistant *hkl* lattice-planes, with interplanar distance d_{hkl}. Constructive interference will be observed for X-rays that are reflected from the lattice planes at the specular angle, if the path length difference between X-rays scattered from different hkl-planes is an integer times the wavelength. This condition is summarized in the Bragg law:

$$n\lambda = 2d_{hkl} \sin(\theta) \tag{3.1}$$

where

d is the spacing between diffracting planes, θis the incident angle, *n* is any integer, and λ is the wavelength of the beam

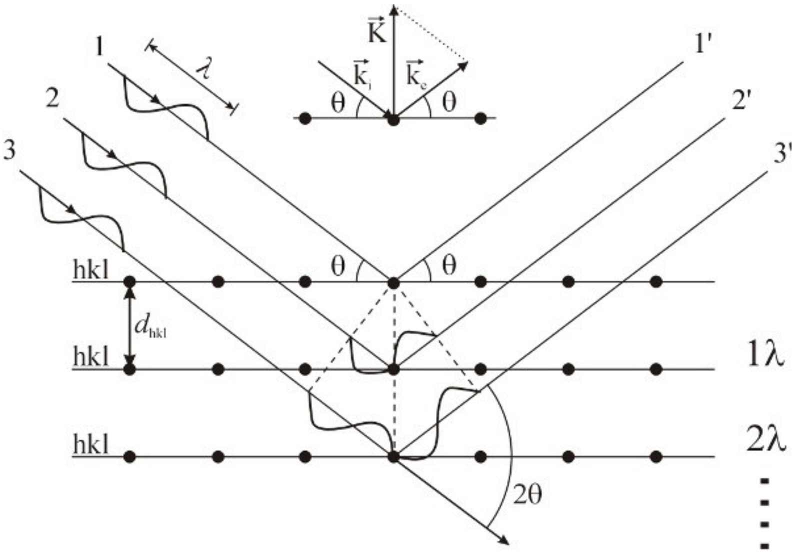

Fig. 3.2. Scheme of X-ray diffraction pattern

From Fig. 3.2, it is clear that diffraction from a set of planes will only occur if the normal to these planes is bisecting the angle between the incident and the scattered beam. Alternatively, one defines a scattering vector $\mathbf{K} = \mathbf{k_e} - \mathbf{k_i}$ as the difference between the wave vector $\mathbf{k_e}$ of the scattered wave, and the wave vector $\mathbf{k_i}$ of the incident X-ray, as shown in the inset of Fig. 3.2.Diffraction (i.e. constructive interference of the scattered X-rays) will occur if the Bragg condition (eq. 3.1) is fulfilled *and* of the scattering vector K is parallel to the normal of the hkl-planes. By scanning crystalline samples in search of interference peaks, one can obtain information about the lattice parameters, strain, texture, etc.

C) Principle of analysis:

A whole gamma of X-ray diffraction measurements can be performed with an X-ray setup. Each of these measurements reveals a different property of the specimen under investigation.

i) θ-2θmeasurement

A θ-2θ scan allows to determine the interplanar distance d. This can beachieved in several geometries, corresponding to the orientation of the set(s) of planes. A *symmetric θ-2θ scan* is used to determine the interplanar distance of the planes parallel to the sample surface [see Fig. 3.3(a)]. In this type of scan, the angle θ of the incoming beam with respect to the sample surface is varied, while simultaneously keeping the detector at an angle of 2θ with respect to the incoming beam. The angle θ at which a diffraction peak is observed, can then be inserted into (eq. 3.1) to give the interplanar distance.

In order to determine the interplanar distance of a set of planes that are tilted by an angle with respect to the sample surface, an asymmetric θ-2θ scan can be performed [see Fig. Eq. 3.3(b)]. As in the case of a symmetric scan, the detector is placed at an angle of 2θ with respect to the incoming beam. The incoming beam, however, makes an angle of Ψ with respect to the sample surface. Note that θ-Ψ is a fixed offset when scanning through θ values.

An alternative to the asymmetric scan method is the *skew-symmetric* measuring geometry [Fig. 3.3(c)]. As in the case of the symmetric scan, the incoming beam forms an angle Ψ with respect to the sample surface, while the detector is put at 2θ. The difference is that the sample is tilted over a fixed angle χ=Ψ around the axis that is parallel to the sample surface and the plane of the incoming and outgoing beam.

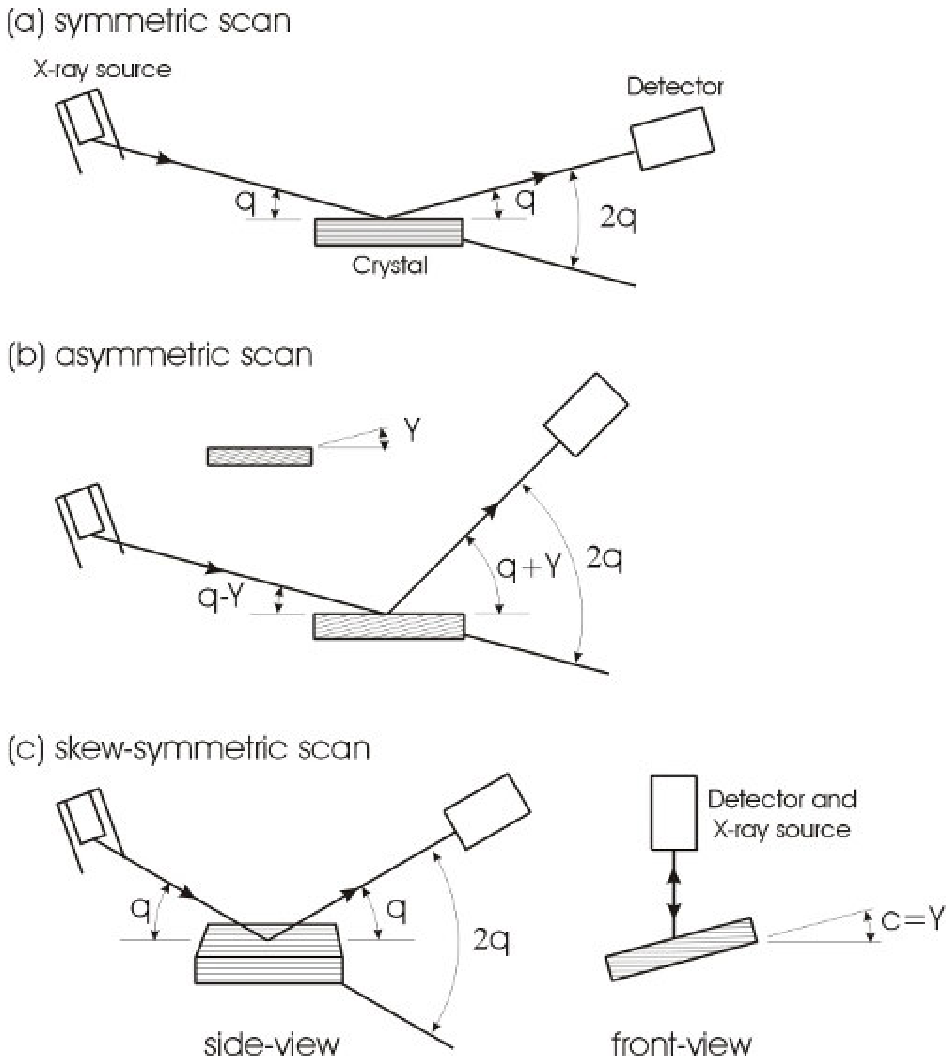

Fig. 3.3: Steps of asymmetric θ-2θ scan

The determination of the interplanar distance with a θ-2θ measurement does not only allow to identify the phases present in the specimen. In thin film studies in particular, this type of scan is used to determine stress and strain epitaxial or implatend layers. Stress and/or strain result in the deviation of the interplanar distances within a crystal from the situation for a completely relaxed thin film. This stress can be induced by the presence of implanted impurities, the match of an epitaxial thin film with a substrate of slightly different lattice parameter, etc. Not only the peak position in a θ-2θ measurement contains valuable information on the specimen under investigation, the width or full width at half maximum of the diffraction peak contains information on the as well. In case of a perfect crystal, the width of the interference peak (as a function of θ) is inversely proportional to the thickness of the crystalline layer. The full width at half maximum (FWHM) of the peak is given by the Scherer formula:

$$\mathrm{FWHM} = 0.9\, \lambda / t \cos(\theta_B) \qquad (3.2)$$

where the FWHM is expressed in radians, λ is the wavelength of the X-rays, t is the thickness of the layer and θ_B the Bragg angle of the reflection. A non-perfect crystal can be divided into different crystalline domains (crystallites) that all have a slightly different orientation. This will be the case when long-range stacking faults and other extended defects are present in the sample. The thickness t in the Scherer formula will, in that case, be related to the crystallite particle size.

ii) Reflectivity measurements

A special type of symmetric θ-2θ scan is the reflectivity measurement. In a normal θ-2θ measurement the distance between crystallographic planes, which is of the order of 0.5-5Å, is measured. In a reflectivity measurement one measures thickness of a thin film which is of the order of tens of nanometer. The principle of the measurement is the same as for the θ-2θ scan described above, apart that the measurement is now performed at much lower reflection angles, due to the larger thickness involved. Scattering of the X-rays now does not occur at the atomic planes, but at the interface between the layers in the film due to the difference in electron density between adjacent layers. This type of measurement does not only allow determining the distance between adjacent layers, it also enables the determination of the roughness of the films.

iii) Rocking curve measurement

Another type of scan that is closely related to a θ-2θ scan is a rocking curve (RC) scan. From a rocking curve measurement it is possible to determine the mean spread in orientation of the different crystalline domains of a non perfect crystal. If the crystalline particles are very small, it is also possible to determine their size by measuring a RC scan. In order to obtain a rocking curve scan, one first performs a θ-2θ scan. Note that this can be carried out in symmetric, asymmetric or skew-symmetric geometry. In the next step, the angle θ, and the detector position 2θ, is fixed at the Bragg angle of the corresponding reflection. A rocking curve scan is then acquired by varying the orientation of the sample by an angle Δω around its equilibrium position, while keeping the detector position fixed. The situation for a skew-symmetric geometry is schematically depicted in Fig. 3.4. For $\Delta\omega = 0$ the sample and detector are at the exact positions for constructive interference, so a peak will be observed. The width of this peak W will be determined by several factors. The first and most interesting contribution comes from the spread in crystalline orientation between the different domains. The corresponding rocking curve peak will have a full width at half-maximum (FWHM) W, where W_{tt} is the mean spread in orientation for the set of planes belonging to the chosen Bragg reflection. The second factor is based on the lateral size of the crystalline domains. This is similar to the Scherrer broadening described above for θ-2θ scans, but depends here on the lateral size of the crystallites instead of their thickness. It can be calculated that this leads to a broadening with FWHM W_{inc}:

$$W_{inc} = \lambda / 2b \sin(\theta_B) \qquad (3.3)$$

where b is the mean width of a crystalline particle. For example, for θB = 30°, b = 500 Å and λ = 1:54 Å, the rocking curve will have a width $W_{inc} = 0.2°$. A last contribution comes from the detector resolution W_d. Our D8 Discover from Bruker, has an angular resolution of < 0.005° when the monochromator is mounted. Since the other two contributions are usually far larger than the detector resolution, this factor can often be neglected. The total width of the rocking curve peak then depends on a combination of these three factors, and is given by the convolution.

iv) Pole figure measurements

In a θ-2θ scan only to the planes that are parallel to the surface will be detected. The number of peaks in an experimental θ-2θ XRD spectrum and their relative intensity give an indication of the texture, i.e. the statistical distribution of grain orientations, of the film. However, the complete texture of a thin film is accessible only with pole figure measurements.

In this kind of measurement, a certain set of hkl-planes is selected. This fixes dhkl in (eq. 3.1), which is achieved by fixing the detector (2θ) and incident beam (θ) angle. Hence, the scattering vector **K** is fixed in space, as can be seen from Fig. 3.4. Diffraction will only occur if the normal to the selected hkl-planes **N** is parallel to the diffraction vector. Therefore, the sample has to be tilted and rotated in space. The situation is shown for the middle grain in Fig. 3.4

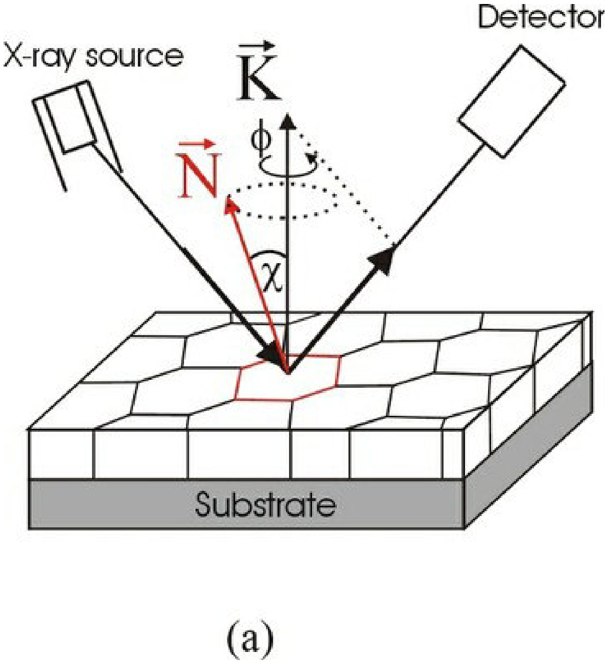

Fig. 3.4

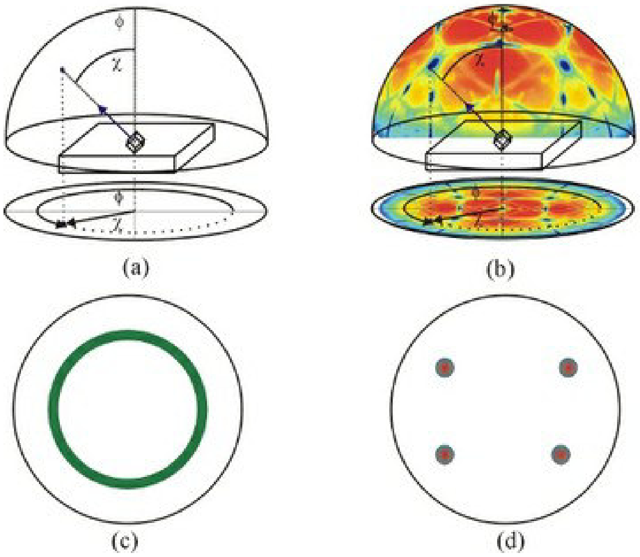

Fig. 3.5

$W^2 = W^2_{tt} + W^2_{inc} + W^2_d$

On the same figure, the tilt χ and the rotation angle Φ are defined. Pole figures can be interpreted by considering the intersections of the normal to the selected hkl-planes with an imaginary hemisphere, situated above the sample surface (see Fig. 3.5). The projection of this hemisphere on a planar surface results in a pole figure, for which the intensity in each point is proportional to the number of grains in the film that have their normal to the selected hkl-planes pointing to the point with coordinates (χ,Φ) on the hemisphere. For a random orientation of the grains in the thin film, the pole figure will be featureless. No preferred orientation for the normal to the hkl-planes is observed. *Fiber texture* can be identified by the occurrence of circles centered around the origin of the pole figure (Fig. 3.5 (c)). For an epitaxial thin film, only one grain orientation will be present in the film and the pole figure is characterized by a small, discrete number of spots (Fig. 3.5 (d)). In the case of axiotaxy, the pole figure shows a pattern of symmetrical lines (Fig. 3.5 (b)).

v) Contributions to chemistry and material science

X-ray crystallography has led to a better understanding of chemical bonds and non-covalent interactions. The initial studies revealed the typical radii of atoms, and confirmed many theoretical models of chemical bonding, such as the tetrahedral bonding of carbon in the diamond structure, the octahedral bonding of metals observed in ammonium hexachloroplatinate (IV), and the resonance observed in the planar carbonate group and in aromatic molecules. Kathleen Lonsdale's 1928 structure of hexamethyl benzene established the hexagonal symmetry of benzene and showed a clear difference in bond length between the aliphatic C–C bonds and aromatic C–C bonds; this finding led to the idea of resonance between chemical bonds, which had profound consequences for the development of chemistry. Her conclusions were anticipated by William Henry Bragg, who published models of naphthalene and anthracene in 1921 based on other molecules, an early form of molecular replacement.

Also in the 1920s, Victor Moritz Goldschmidt and later Linus Pauling developed rules for eliminating chemically unlikely structures and for determining the relative sizes of atoms. These rules led to the structure of brookite (1928) and an understanding of the relative stability of the rutile, brookite and anatase forms of titanium dioxide.

The distance between two bonded atoms is a sensitive measure of the bond strength and its bond order; thus, X-ray crystallographic studies have led to the discovery of even more exotic types of bonding in inorganic chemistry, such as metal-metal double bonds, metal-metal quadruple bonds, and three-center, two-electron bonds. X-ray crystallography or, strictly speaking, an inelastic Compton scattering experiment has also provided evidence for the partly covalent character of hydrogen bonds. In the field of organometallic chemistry, the X-ray structure of ferrocene initiated scientific studies of sandwich compounds, while that of Zeise's salt stimulated research into "back bonding" and metal-pi complexes. Finally, X-ray crystallography had a pioneering role in the development of super a molecular chemistry, particularly in clarifying the structures of the crown ethers and the principles of host-guest chemistry.

In material sciences, many complicated inorganic and organ metallic systems have been analyzed using single-crystal methods, such as fullerenes, metalloporphyrins, and other complicated compounds. Single-crystal diffraction is also used in the pharmaceutical industry, due to recent problems with polymorphs. The major factors affecting the quality of single-crystal structures are the crystal's size and regularity; recrystallization is a commonly used technique to improve these factors in small-molecule crystals. The Cambridge Structural Database contains over 500,000 structures; over 99% of these structures were determined by X-ray diffraction.

3.2.2 Transmission Electron Microscopy (TEM)

Transmission Electron Microscopy (TEM) is a well-known technique for imaging solid materials at atomic resolution. Structural information can be acquired both by (high resolution) imaging as well as by electron diffraction. Additional detectors allow for elemental and chemical analysis down to this sub-nanometer scale.

Basic principles

The design of a transmission electron microscope (TEM) is analogous to that of an optical microscope. In a TEM high-energy (>100 kV) electrons are used instead of photons and electromagnetic lenses instead of glass lenses. The electron beam passes an electron-transparent sample and a magnified image is formed using a set of lenses. This image is projected onto a fluorescent screen or a CCD camera. Whereas the use of visible light limits the lateral resolution in an optical microscope to a few tenths of a micrometer, the much smaller wavelength of electrons allows for a resolution of 0.2 nm in a TEM.

Imaging

Image contrast is obtained by interaction of the electron beam with the sample. Several contrast effects play a role. In the resulting TEM image denser areas and areas containing heavier elements appear darker due to scattering of the electrons in the sample. In addition, scattering from crystal planes introduces diffraction contrast. This contrast depends on the orientation of a crystalline area in the sample with respect to the electron beam. As a result, in a TEM image of a sample consisting of randomly oriented crystals each crystal will have its own grey-level. In this way one can distinguish between different materials, as well as image individual crystals and crystal defects. Because of the high resolution of the TEM, atomic arrangements in crystalline structures can be imaged in large detail.

Electron Diffraction

By adjusting the magnetic lenses such that the back focal plane of the lens rather than the imaging plane is placed on the imaging apparatus a diffraction pattern can be generated. For thin crystalline samples, this produces an image that consists of a pattern of dots in the case of a single crystal, or a series of rings in the case of a polycrystalline or amorphous solid material. For the single crystal case the diffraction pattern is dependent upon the orientation of the specimen and the structure of the sample illuminated by the electron beam. This image provides the investigator with information about the space group symmetries in the crystal and the crystal's orientation to the beam path. This is typically done without utilising any information but the position at which the diffraction spots appear and the observed image symmetries.

Diffraction patterns can have a large dynamic range, and for crystalline samples, may have intensities greater than those recordable by CCD. As such, TEMs may still be equipped with film cartridges for the purpose of obtaining these images, as the film is a single use detector.

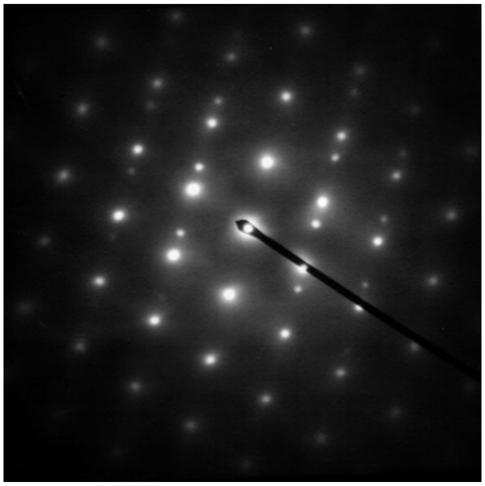

Fig. 3.6 (a): Crystalline diffraction pattern from a twinned grain of FCC Austenitic steel

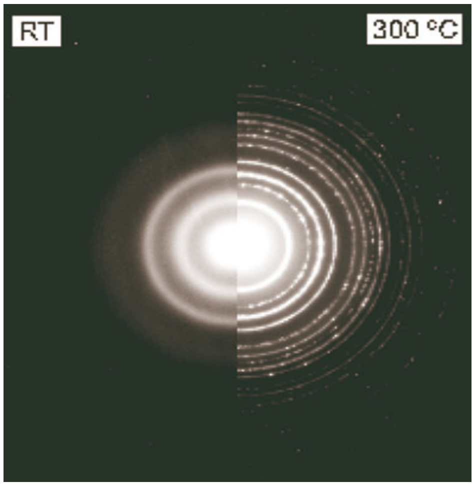

Fig. 3.6 (b): Electron diffraction patterns of an as-deposited (room temperature) and an annealed (300 ºC) Al-Ge film. The left part shows a set of a few, broad rings, characteristic of an amorphous film. The right part shows a large number of sharp rings. The diameters of these rings are characteristic for the crystal structure present. In this case a mixture of crystalline Al and crystalline Ge.

In case of a crystalline material, electron diffraction will only occur at specific angles, which are characteristic for the crystal structure present. As a result, a diffraction pattern of the irradiated area is created that can be projected onto the CCD camera. In this way, electron diffraction can provide crystallographic information from thin films, bulk materials as well as from nanometer sized particles (figure 3.6).

Chemical analysis

As a result of the interaction of the electron beam with the specimen, some energy is transferred from the electrons to the sample. The excitation and de-excitation of atoms and molecules in the sample allow (local) chemical analysis. This analysis can either be performed using the broad beam used for normal imaging, or by focusing the beam size down to 0.2 nm. The combination of Scanning TEM (STEM), a mode in which this narrow beam scans a selected area of the specimen, with chemical analysis techniques such as Electron Energy Loss Spectroscopy (EELS) and Energy Dispersive X-Ray analysis (EDX) allows for mapping of the lateral distribution of elements with high spatial resolution.

3.2.3 Scanning electron microscope (SEM)

A scanning electron microscope is a type of electron microscope that images a sample by scanning it with a high-energy beam of electrons in a raster scan pattern. The electrons interact with the atoms that make up the sample producing signals that contain information about the sample's surface topography, composition, and other properties such as electrical conductivity.

The types of signals produced by the SEM include secondary electrons, back-scattered electrons (BSE), characteristic X-rays, light (cathode), specimen current and transmitted electrons. Secondary electron detectors are common in all SEMs, but it is rare that a single machine would have detectors for all possible signals. The signals result from interactions of the electron beam with atoms at or near the surface of the sample. In the most common or standard detection mode, secondary electron imaging or SEI, the SEM can produce very high-resolution images of a sample surface, revealing details about less than 1 to 5 nm in size. Due to the very narrow electron beam, SEM micrographs have a large depth of field yielding a characteristic three-dimensional appearance useful for understanding the surface structure of a sample. This is exemplified by the micrograph of pollen shown to the right. A wide range of magnifications is possible, from about 10 times (about equivalent to that of a powerful hand-lens) to more than 500,000 times, about 250 times the magnification limit of the best light microscopes. Back-scattered electrons (BSE) are beam electrons that are reflected from the sample by elastic scattering. BSE are often used in analytical SEM along with the spectra made from the characteristic X-rays. Because the intensity of the BSE signal is strongly related to the atomic number (Z) of the specimen, BSE images can provide information about the distribution of different elements in the sample. For the same reason, BSE imaging can image colloidal goldimmuno-labels of 5 or 10 nm diameter which would otherwise be difficult or impossible to detect in secondary electron images in biological specimens. Characteristic X-rays are emitted when the electron beam removes an inner shell electron from the sample, causing a higher energy electron to fill the shell and release energy. These characteristic X-rays are used to identify the composition and measure the abundance of elements in the sample.

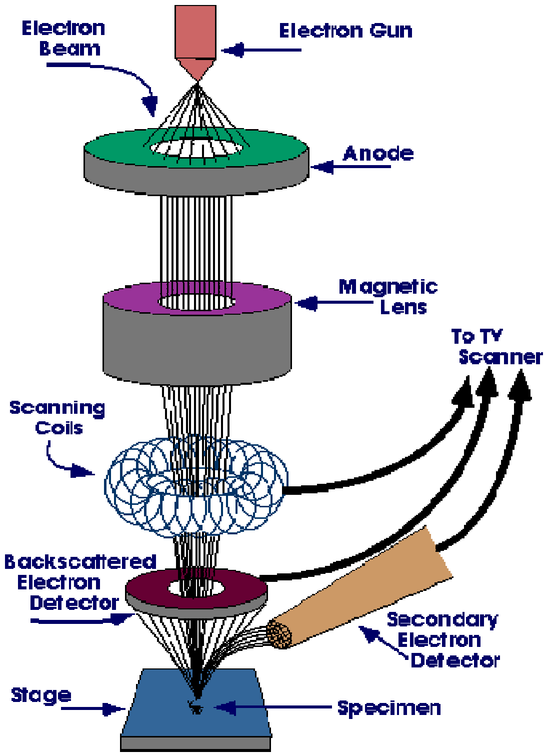

Fig. 3.7: Schematic diagram of scanning electron microscope.

The electron beam comes from a filament, made of various types of materials. The most common is the Tungsten hairpin gun. This filament is a loop of tungsten which functions as the cathode. A voltage is applied to the loop, causing it to heat up. The anode, which is positive with respect to the filament, forms powerful attractive forces for electrons. This causes electrons to accelerate toward the anode. Some accelerate right by the anode and on down the column, to the sample. Other examples of filaments are Lanthanum hexaboride filaments and field emission guns.

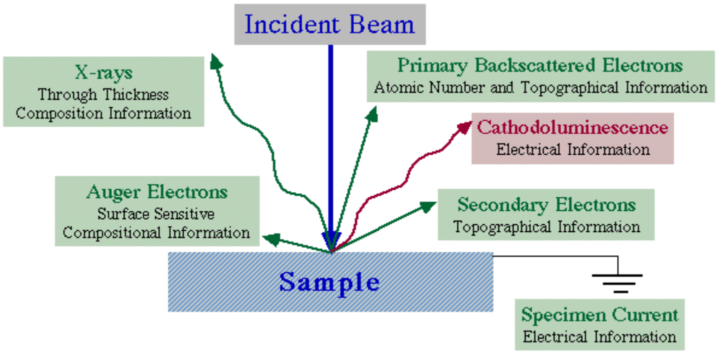

Fig 3.8: Electron specimen interaction.

The SEM uses electrons instead of light to form an image. A beam of electrons is produced at the top of the microscope by heating of a metallic filament. The electron beam follows a vertical path through the column of the microscope. It makes its way through electromagnetic lenses which focus and direct the beam down towards the sample. Once it hits the sample, other electrons (backscattered or secondary) are ejected from the sample. Detectors collect the secondary or backscattered electrons, and convert them to a signal that is sent to a viewing screen similar to the one in an ordinary television, producing an image.

3.2.4 Infrared Spectroscopy (IR)

Infrared spectroscopy is the method of choice of qualitative analysis of organic material and it has wide application to inorganic substances as well. The infrared spectrum of a material has aptitude for the fingerprint, a unique property of that material and of its physical state. The spectrum is unique because it reflects the vibration between atoms within the molecule, and even slight changes in geometry or bond strength between atoms cause noticeable shift in the infrared absorption pattern.

When a molecule interacts with the radiation of the proper frequency, it absorbs energy and molecule is set into vibration. By measuring the transmitted energy as a function of radiation frequency, we can determine which frequency has been absorbed by the sample. The resulting plots of energy versus frequency are the infrared spectrum of the sample.

The infrared spectra of all the samples of the present series were recorded at room temperature in the range 300 - 800cm^{-1} on a Perkin Elemer spectrometer (Model 783). To study the IR spectra of all the samples, about one gram of fine powder of each sample was mixed with KBr in the ratio 1:250 by weight to ensure uniform distribution in the KBr pellet. The mixed powder was then pressed in a cylindrical die to obtain clean disc of approximately 1 mm thickness. The IR spectra were used to locate the band position. The IR spectra were used to determine bond length R_A and R_B, in a cubic crystal for tetrahedral (A) and octahedral [B] site using formula given by Gorter [1]. Using the analysis of Waldron [2], the force constant K_0 and K_t were calculated.

3.2.5 Vibrating sample magnetometer (VSM)

A vibrating sample magnetometer or VSM is a scientific instrument that measures magnetic properties invented in 1955 by Simon Foner at Lincoln Laboratory MIT. The paper about his work was published shortly afterward in 1959 [3]. A sample is placed inside a uniform magnetic field to magnetize the sample. The sample is then physically vibrated sinusoidally, typically through the use of a piezoelectric material. Commercial systems use linear actuators of some form and historically the development of these systems was done using modified audio speakers, though this approached was dropped due to the interference through the in-phase magnetic noise produced, as the magnetic flux through a nearby pickup coil varies sinusoidally. The induced voltage in the pickup coil is proportional to the sample's magnetic moment, but does not depend on the strength of the applied magnetic field. In a typical setup, the induced voltage is measured through the use of a lock-in amplifier using the piezoelectric signal as its reference signal. By measuring in the field of an external electromagnet, it is possible to obtain the hysteresis curve of a material.

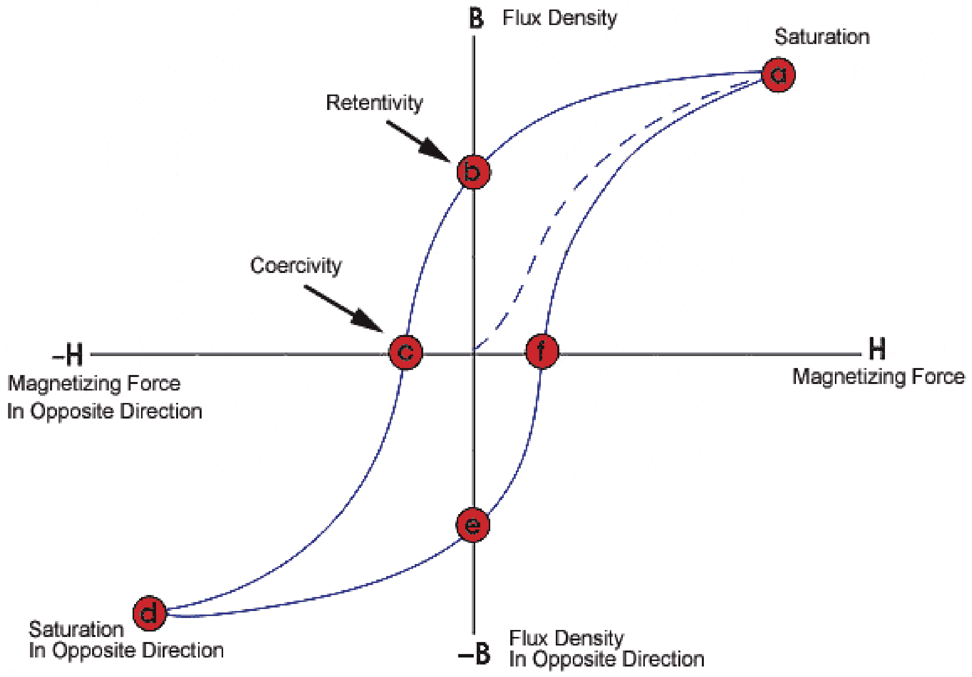

Fig. 3.9: A typical hysteresis curve of a spinel ferrite.

A typical hysteresis curve of a spinel ferrite is also shown in Fig. 3.9. A great deal of information can be learned about the magnetic properties of a material by studying its hysteresis loop. A hysteresis loop shows the relationship between the induced magnetic flux density **(B)** and the magnetizing force **(H).** It is often referred to as the B-H or M-H loop. From the hysteresis loop, a number of primary magnetic properties of a material can be determined such as magnetization (Ms), coercivity (H_C), remanence magnetization (Mr) etc.

References

[1] E.W. Gorter, Philips Res. Rep. 9 (1954) 295.

[2] R.D. Waldron, Phys. Rev. 99 (1955) 1727.

[3] S. Foner, "Versatile and Sensitive Vibrating-Sample Magnetometer".Rev. Sci. Instrum 30 (7) (1959) 548.

Chapter 4

Results and discussion on$CoMn_{1-x}Al_xFeO_4$

4.1 Introduction

Magnetic nano particles have received increasing attention recently due to their unusual properties, while the interest in hard magnetic materials is growing because of the various technological applications in microwave devices, high-density magnetic recording, electronic devices and medical instruments [1-4]. The field of spinel ferrites magnetic nano particles is well cultivated because of their various potential applications and the interesting physics and chemistry involved in it. Even after more than half of the century the scientist, researchers, technologist, and engineers are still excited in various types of bulk as well as nano crystalline ferrite materials. The recent trend is focused on the doped ferrites prepared using various synthesis techniques with different cation concentrations which in turn affects the various properties like, electrical, dielectric, and magnetic behavior[5-8].

Ferrite materials are important magnetic materials, which have various applications in power conditioning and conversion. Due to their distinct magnetic properties, ferrite materials have been widely used to prepare many electromagnetic devices such as inductors, converters, phase shifters and electromagnetic wave absorbers [9,10].Nano sized ferrite particles exhibit unusual magnetic properties which are not observed in the bulk material, e.g. single domain behavior, super paramagnetism, and reduced Curie temperature and magnetization. The spatial confinement at nano scale enhances the role of surface atoms with reduced symmetry and the consequent larger number of broken exchange bonds can result in surface anisotropy, frustration and spin disorder [11-14].

The magnetic and structural properties of soft ferrites could be easily turned by incorporation and suitable addition of divalent or trivalent cations in the spinel structure. Cobalt ferrite ($CoFe_2O_4$), a well-known hard ferri magnetic material, in its bulk form crystallizes in mixed spinel structure with space group Fd3m. Since the $Fe_A^{3+} - Fe_B^{3+}$ super exchange interactions differs from the $Co_A^{2+} - Co_B^{3+}$ interactions, variation of the cation distribution over the A and B sites in the spinel leads to different magnetic properties of this ferrite even though the chemical compositions of the compounds do not change $CoFe_2O_4$has large magneto crystalline anisotropy energy with positive anisotropy constant. It has six easy directions along the cube edges of the crystal represented as <100>,four hard directions across the body diagonals denoted as <111> and twelve saddle points across the face diagonals, which lead to positive magneto crystalline anisotropy constant [15-17].The large magneto crystalline anisotropy energy of cobalt ferrite is mainly attributed to the Co^{2+}ions on the B-sites of the spinel. As the crystal field is not capable to quench the orbital magnetic moment, there is a strong spin–orbit coupling (L-S coupling) and due to this coupling there is large magneto crystal- line anisotropy energy (MAE) [18].Thus large multi axial positive magneto crystalline anisotropy constant makes it a hard magnetic material. This magneto crystalline anisotropy is a very important parameter in connection with the characterisation of the materials utilised in technological applications, particularly magnetic recording media and, it can be tuned by replacing a site and/or B site by different transition elements.

Manganese doped cobalt ferrites are promising ones for magnetic stress sensors, non contact torque sensing, magnet optical, magneto mechanical, and high magnetostriction applications [19–22].The magnetization in Mn doped cobalt ferrites is expected to depend on the cation distribution of the magnetic Fe^{3+}, $Mn^{2+}$and Co^{2+} ions among the A- and B-sites. Recently, the temperature dependence of the magnetic anisotropy of a series of mixed cobalt ferrites has been investigated and it was found that substituting M for Fe in cobalt ferrite allows adjustment of the Curie temperature (Tc) of the material,there by influencing the temperature dependence of its stress sensitivity and magneto mechanical response of these materials. It has been shown that manganese substituted cobalt ferrites, are excellent candidates for stress sensors due to a large magneto mechanical effect and high sensitivity to stress. This is because weakening of the exchange coupling results in a decrease of the magneto crystalline anisotropy which also results in a steeper response of strain to applied magnetic field [23]. From the studies on the magnetic and magnetostrictive properties of Mn substituted cobalt ferrites it has been found that substitution of Mn enhances the saturation magnetization as well as the magnetostrictive properties of the cobalt ferrite; when Mn is substituted byCo^{2+} in the B-site as compared to the displacement of Co^{2+} from the B- to A-sites when $Mn^{3+}$is substituted by Fe^{3+}in the Co–Mn ferrite system. This is because; the high magneto crystalline anisotropy of the cobalt ferrite is due to the Co^{2+} at B-site. It has also been reported [24] that the direct substitution of Mn^{2+}/ Mn^{3+} for Co^{2+} in the cobalt ferrite, showed a comparatively higher magnetostriction and strain derivative at relatively low magnetic fields for a peculiar composition, which depicts the importance of Mn^{2+}/Mn^{3+} substitution for Co^{2+} in tuning the magneto elastic response of cobalt ferrite [25].

Since, the temperature dependence of the magneto elastic properties is strongly dependent on the magnetostriction and magnetic anisotropy, as well as coercivity, permeability, and chemical composition of the material. As the per the literature review these properties appeared excellent with Co-Mn ferrite, therefore in our present study we have kept $Co\text{-}MnFeO_4$ as a basic composition for further investigation.

Al^{3+}ionic size is comparable to Fe^{3+}ions. Hence, doping on magnetic Al^{3+}in place of Fe^{3+}ion will even the material with magnetic defects without changing the crystal structure. The magnetic properties of Al^{3+}substituted ferrites have been reported by various groups. The structural and magnetic studies on nano size aluminum substituted ferrites synthesized by aerosol route were carried out in the literature and the results revealed that the lattice parameter and saturation magnetisation decrease with increase of the Al^{3+}substitution [26].N. Ravah et al. [27] synthesized the Al^{3+} substituted cobalt ferrite by ceramic route and found that the magneto crystalline anisotropy constant decreased with the increasing magnetic annealing temperature. The magneto- crystalline anisotropic constant is highly size dependent.

The properties of this magnetic material depend on the purity, size and morphology of the precursor powder. Thus obtaining fine, high chemical homogeneity and mono dispersed particles is the most important process in material manufacturing. Conventional ceramic powder preparation using mixed oxides presents various disadvantages, including the introduction of impurities during the grinding process, low-chemical homogeneity and high sintering temperatures. A variety of techniques have been used to prepare ferrite materials of nano-scale including co-precipitation method [28-32], sol–gel process [33–35], glass crystallization[36], the mechanical alloying method [37–39], self-propagation[40,41], micro emulsion [42], microwave [43–45], hydrothermal [46] and ultrasound-assisted synthesis [47].

Keeping the importance of Co-Mn ferrite and the need to prepared these samples in nanometer dimensions it was decided to synthesized $CoMn_{1-x}Al_xFeO_4$ (x = 0.0, 0.25, 0.5, 0.75, 1.0) ferrite system. The structural and magnetic changes in the Co-Mn ferrite brought by the Al^{3+} substitution synthesized via sol-gel auto-combustion method is discussed here.

4.2 Experimental

Sol-gel auto-combustion route was adopted to achieve the homogeneous mixing of the chemical constituents at the atomic scale and better sinter ability. AR grade cobalt nitrate ($Co(NO_3)_2{\cdot}3H_2O$), aluminum nitrate ($Al(NO_3)_3{\cdot}9H_2O$), manganese nitrate ($Mn(NO_3)_2{\cdot}6H_2O$),iron nitrate ($Fe(NO_3)_3{\cdot}9H_2O$) and citric acid ($C_6H_8O_7{\cdot}H_2O$),were used to prepare the $CoMn_{1-x}Al_xFeO_4$ (x = 0.0, 0.25, 0.5, 0.75, 1.0) ferrite compositions. Reaction procedure was carried out in air atmosphere without protection of inert gases. The molar ratio of metal nitrates to citric acid was taken as 1:3. The metal nitrates were dissolved together in a minimum amount of double distilled water to get a clear solution. An aqueous solution of citric acid was mixed with metal nitrates solution, then ammonia solution was slowly added to adjust the pH at 7. Then the solution was heated at 90 ºC to transform into gel. When ignited at any point of the gel, the dried gel burnt in a self-propagating combustion manner until all gels were completely burnt out to form a fluffy loose powder. The auto-combustion was completed within a minute, yielding the brown-colored ashes termed as a precursor. Finally, the as prepared ferrite powder was annealed at 600 ºC for 4 h in order to complete the crystallization. Theoretical percentage of the elements in the finally synthesized $CoMn_{1-x}Al_xFeO_4$ ferrite sample is shown in Table 4.1.

The crystal structure of the as prepared samples was characterized by X-ray diffraction technique using Phillips X-ray diffract meter (Model 3710) equipped with Cu-K_α radiation (λ=1.5405Å). The microstructure was examined on the fracture surfaces of the samples using thermal field emission scanning electron microscope (SEM). Transmission electron microscope (TEM) measurements were recorded on Philips (Model CM 200). The samples were prepared by dispersing the powders in acetone and dropping the suspension on a lacey carbon film supported on a 300-mesh copper grid. The infrared spectra of all the samples were recorded at room temperature in the range 300 cm^{-1} to 800 cm^{-1} using Perkin Elmer infrared spectrophotometer. Room temperature magnetization of the samples was measured using the pulse field magnetization set-up.

4.3 Results and discussion

4.3.1 Structural Analysis

Prepared samples were tested by X-ray diffraction. Fig. 4.1 (a-c) shows the XRD patterns of the samples with different doping levels of Al^{3+} substitution. The reflection from the planes, (2 2 0), (3 1 1), (2 2 2), (4 0 0), (4 2 2), (333) and (4 4 0) appeared for all samples. The patterns indicate well-defined peaks of crystalline FCC phase which confirm spinel cubic structure formation for the samples and belong to the (Fd3m) cubic spinel space group. No additional impurity reflections were observed ensuring the phase purity which indicates the formation of the single-phase spinel ferrite structure.

The lattice parameters have been computed using the d-spacing values and the respective (h k l) parameters from the classical formula given in Eq.4.1 [48]:

$$a = \frac{\lambda}{2}\frac{\sqrt{(h^2+k^2+l^2)}}{\sin\theta} \qquad \textbf{4.1}$$

Where

d is the inter-planer spacing and (*hkl*) is the index of the XRD reflection peak. The lattice constant is affected by the cationic stoichiometry. The lattice parameters are found to decrease almost linearly by increasing Al^{3+} substitution. The values of the lattice parameter exhibit an almost linear dependence, thus obeying Vegard's law [49] as shown in Table 4. 2 and Fig. 4.2.

The X-ray density (dx) of all the samples of the series was obtained by the following relation:

$$dx = \frac{8M}{Na^3} \qquad \textbf{4.2}$$

where '8' is the number of molecules per unit cell, 'M' is the molecular weight of sample, 'N' is the Avogadro's number and 'a' is lattice constant. It can be observed from Table 4.2and Fig. 4.3 that the value of dx decreases with Al^{3+} substitution. This may be due to the fact that the density and atomic weight of Al^{3+} are smaller than that of Mn^{3+} ions. The density and atomic weight of Al^{3+} is 2.70 $g{\cdot}cm^{-3}$ and 26.98 respectively whereas it is 7.23 $g{\cdot}cm^{-3}$ and 54.93 respectively for Mn^{3+} ion.

However, the bulk density (d_B) calculated from the Archimedes principle depicted in Table 4.2and Fig. 4.4 shows the smaller value as compared to that of dx. The smaller value of dB than that of the dx is due to the existence of pores that depend on the sintering and pressing conditions. The peaks of (2 2 0), (3 1 1), (2 2 2), (4 0 0), (4 2 2), (333) and (4 4 0) have been deconvoluted to Lorentzian curves for the determination of the crystallite size using full-width at half maximum value. The crystallite size of the nano crystalline samples were measured from XRD line broadening analysis applying Scherrer's formula [48]:

$$D_{XRD} = \frac{k\lambda}{\beta\cos\theta} \qquad \textbf{4.3}$$

Where

D_{XRD} is the dimension of the crystallites, λ the wavelength of the X-ray radiation, θ the Bragg angle, k is a shape factor taken to be 0.94 and β the peak width measured at half of the maximum intensity.

The variation of D_{XRD} is shown in Fig. 4.5 and the values are presented in Table 4.2.The values of the D_{XRD} is in the range of 18 to 9 nm and showed reasonable decreasing trend with the increase in Al^{3+} substitution in Co-Mn ferrite.

The percentage porosity (P) is calculated using the following relation:

$$P = \left(\frac{d_X - d_B}{d_X}\right) \times 100 \qquad \textbf{4.4}$$

Where

dx and d_B are the X-ray density and bulk density respectively.

Table 4.2 and Fig. 4.6 shows that the porosity of the samples increases with Al^{3+} substitution; this may be due to the release of oxygen from the samples during interring i.e., the decrease in oxygen ion (anion) diffusion would retard the densification. The increase in porosity with Al^{3+} substitution is also related to the decrease in bulk density and decrease in crystallite size.

L_A and L_B i.e. the hopping length for tetrahedral A- and octahedral B-sites respectively were calculated using the following relation:

$$L_A = a\sqrt{\frac{3}{4}} \qquad \textbf{4.5}$$

$$L_A = a\sqrt{\frac{2}{4}} \qquad \textbf{4.6}$$

The variation of hopping lengths L_A and L_B with Al^{3+}substitution is depicted in Fig. 4.7 and Table 4.3. It is observed from Table 4.3 and Fig. 4.7 that the distance between the magnetic ions (hopping length) decreased with Al^{3+} substitution. This behavior of hopping lengths with Al^{3+} substitution is in agreement with the variation in lattice constant with Al^{3+} substitution. The variation of L_A and L_B may be related to the difference in the ionic radii between Al^{3+} and Mn^{3+} ions. The substitution of Al^{3+} ions instead of Mn^{3+} ions makes the magnetic ions become smaller to each other and the hopping length decreased.

Transmission electron microscopy

The shape, size and morphology of the particles were examined by direct observation via transmission electron microscopy (Figs. 4.8(a) and 4.9 (a)). The observations reveal that the particles are approximately spherical in shape and agglomerated. The selected area diffraction pattern (SAED) collected from agglomerates is shown in Figs. 4.8(b) and 4.9 (b).Rings in SAED correspond to lattice plains and reveal presence of spinel phase. It was not possible to distinguish two similar ferrites from SAED and XRD.

Scanning electron microscopy

Fig. 4.10 (a and b) shows the SEM micrographs of the samples with x = 0.0 and 1.0 respectively. It is observed that majority of grains are spherical in shape. The SEM micrograph for x = 0.0 shows well dispersed grains with identical shape and size. It is interesting to note that, as the amount of Al^{3+}content increases, the nature of microstructure gets modulated. In the case of x = 1.0 the grains are non-identical in size and grains are slightly agglomerated. Nano particles are dense and distributed regularly on the whole area. In addition to this, although these smaller crystallites are so closely arranged together, a clear boundary between neighboring crystallites can yet be observed.

Using the experimental values of lattice constant '*a*', oxygen positional parameter '*u*' (0.375 Å) and substituting using the following equations, the allied parameters such as tetrahedral and octahedral bond length (d_{Ax} and d_{Bx}), tetrahedral edge, shared and unshared octahedral edge (d_{AXE}, d_{BXE} and d_{BXEU}) were calculated.

$$d_{AX} = a\sqrt{3}\left(u - \frac{1}{4}\right) \qquad \textbf{4.7}$$

$$d_{BX} = a\left[3u^2 - \left(\frac{11}{4}\right)u + \frac{43}{64}\right]^{\frac{1}{2}} \qquad \textbf{4.8}$$

$$d_{AXE} = a\sqrt{2}\left(2u - \frac{1}{2}\right) \qquad \textbf{4.9}$$

$$d_{BXEshaired}=a\sqrt{2}\left(1-2u\right) \tag{4.10}$$

$$d_{BXEunshair\ ed}=a\left(4u^{2}-3u+\frac{11}{16}\right)^{\frac{1}{2}} \tag{4.11}$$

Table4.4 and Figs. 4.11-4.15shows that tetrahedral bond length and octahedral bond length decreases as Al^{3+} ion substitution increases. The tetrahedral edge, shared and unshared octahedral edge decreases as Al^{3+} content 'x' increases. This could be related to the smaller radius of Al^{3+} ion as compared to Mn^{3+} ion.

4.3.2 Infrared spectroscopy (IR)

The IR spectra in the range of 200 to 1000 cm^{-1}at room temperature are shown in Figs. 4.16 (a-c). The band positions are listed in Table 4.5.The two wide bandsν_1 and ν_2 are characteristic of spinel ferrites, where their existence reveals that these samples are a single- phase spinel ferrites. The band ν_1 lies in the range 742 cm^{-1} to 816 $cm^{-1}$and is assigned to the complexes Fe^{3+}–O^{2-} on the A-sites and ν_2 lies in the range of 299 cm^{-1} to 364 $cm^{-1}$and is assigned to Fe^{3+}–O^{2-}on the B-sites vibration modes [50]. The difference in the position of the two strong bands ν_1 and ν_2 could be related to the difference in Fe^{3+}–O^{2-}distance for A-sites and B-sites. It was found that Fe–O distance of A-site (0.189 nm) is smaller than that of the B-site (0.199 nm). The bandν_3 appeared around 527-550 cm^{-1}can be attributed to the divalent metal oxygen complexes Fe^{3+}–O^{2-}, Co^{3+}–$O^{2}$and Mn^{3+}–O^{2-} on the A-sites. The band ν_4 appeared around 229-283 cm^{-1}may be assigned to the lattice vibrations of the system and is dependent on the A-site complexes Fe^{3+}–O^{2-}, Co^{3+}–O^{2} [51, 52]. The existence of Fe^{2+}ions amongst the sub lattice causes a splitting of its band producingν_3 at $\nu_1$and ν_4 at ν_2. This results from the distortion of the Jan-teller effect of Fe^{2+}ions [53,54]. The Fe^{2+} ions may result from the hopping process;$Co^{2+}+Fe^{3+}\leftrightarrow Co^{3+}+Fe^{2+}$, $Mn^{2+}+Fe^{3+}\leftrightarrow Mn^{3+}+Fe^{2+}$ whereCo^{3+} may migration to the A-sites and Fe^{2+}ions remains in their sites.

4.3.3 Cation distribution

The ideal spinel structure, AB_2O_4 can be described as a cubic closed-packed array of oxygen ions. There are eight molecules per unit cell and oxygen is located at the (32e) position of the space group (Fd3m). The A cations occupy the tetrahedral sites (8a) and the B cations occupy the octahedral sites (16d). The anions occupy the general positions 32e, which require an additional parameter, generally designated as u and known in oxide spinels as the oxygen parameter [55].

The cation distribution in spinel ferrite can be obtained from the analysis of X-ray diffraction pattern. In the present work, the Bertaut method [56] is used to determine the cation distribution. This method selects a few pairs of reflections according to the expression:

$$(I_{\downarrow}hkl^{\uparrow}(Obs.))/(I_{\downarrow}h(k(l(^{\uparrow}(Obs.)) = (I_{\downarrow}hkl^{\uparrow}(Calc.))/(I_{\downarrow}h(k(l(^{\uparrow}(Calc.)) \qquad 4.12$$

Where

$I_{hkl}^{Obs.}$ and $I_{hkl}^{Calc.}$ are the observed and calculated intensities for reflection (hkl), respectively.

The best information on cation distribution is achieved when comparing experimental and calculated intensity ratios for reflections whose intensities (i) are nearly independent of the oxygen parameter, (ii) vary with the cation distribution in opposite ways and (iii) do not differ significantly.

The distribution of divalent and trivalent cations among octahedral and tetrahedral sites in the presently investigated samples were determined from the ratio of XRD lines I_{220}/I_{440} and I_{422}/I_{400}.These planes are assumed to be sensitive to the cation distribution. The temperature and absorption factors are not taken into account in our calculations as they do not affect the intensity calculation. If an agreement factor (R) is defined as in Eq. (4.13), the best-simulated structure which matches the actual structure of the sample will lead to a minimum value of R and the corresponding cation distribution is obtained for each hkl and $h(k(l($ reflection pair considered:

$$\frac{I_{hkl}^{Calc.}}{\left(I_{h\left(k\left(l\left(^{Calc.}\right)\right)\right.}\right|} \qquad 4.13$$

For the calculation of the relative integrated intensity (I_{hkl}) of a given diffraction line from powder specimens as observed in a diffract meter with a flat-plate sample holder, the following formula is valid,

$$I_{hkl} = |F|^2_{hkl} P L_P \tag{4.14}$$

Where F is the structure factor, P is the multiplicity factor, L_P is the Lorentz-polarization factor and

$$L_P = \frac{1 + cos^2 2\theta}{sin^2\theta cos\theta} \tag{4.15}$$

The atomic scattering factors for various ions were taken from the literature [49].

It should be added that the calculated integrated intensities are valid at 0 K. Because the observed values are obtained at room temperature, a suitable correction is in principle necessary for precise comparison. However, the spinels are high-melting compounds, the thermal vibration of the atoms at room temperature should not differ greatly from that at absolute zero. Therefore, in our intensity calculations no temperature correction was deemed necessary.

The estimated cation distribution is shown in Table 4.6. The estimated cation distributions show that the structure is really that of a mixed spinel phase where Co^{2+}, Fe^{3+}, Mn^{3+} and Al^{3+} ions are distributed in a non statistic way over the A- and B-sites. However, as light difference in the estimated values of cation distributions attributed to the different production method and also on heat treatment procedure. Therefore, the cation distribution produces a significant effect on the magnetic properties, which is discussed in the magnetic section.

Theoretical lattice parameter (a_{th}) were calculated using the following equation [57]:

$$a_{th} = \frac{8}{3}\sqrt{3}\left[(r_A + R_0) + \sqrt{3}(r_B + R_0)\right] \tag{4.16}$$

Wherer

r_A and r_B are radii of tetrahedral (A) site and octahedral [B] site, R_O is radius of oxygen i.e. ($R_O = 1.32$ Å).

The values of a_{th} for various Al^{3+}substitution is presented in Table 4.7 and their variation is shown in Fig. 4.17. The variation of a_{th} with Al^{3+} substitution is in conformity with the variation of lattice constant ‘a’ calculated from XRD data.

The mean ionic radius of the tetrahedral A- and octahedral B-sites (r_A and r_B) were be calculated using the estimated cation distribution. The values are given in Table 4.7 and its variation is shown in Figs. 4.18 and 4.19. It is observed that the ionic radii of B-sites decreased with the increase in Al^{3+} substitution. The ionic site radii of B site (r_B) is decreased due to the increasingly occupation of the smaller Al^{3+}ions of ionic radii of 0.51 Å (Fig. 4.19).This Al^{3+}ions replaced Mn^{3+}ions of 0.66 ´. Further, it is observed from Fig. 4.18 that the mean ionic radii of tetrahedral A-site (r_A) increased with the increase in Al^{3+} substitution in Co-Mn ferrite. This increase in r_A is associated with the migration of some of the Co^{2+} ions from B site to A site with the Al^{3+}substitution.

Table 4.7and Fig. 4.20 shows the calculated values of oxygen positional parameter ‘u’. The value of oxygen position parameter were calculated using the relation [58]:

$$u = \left[(r_A + R_0)\frac{1}{\sqrt{3}a} + \frac{1}{4} \right] \qquad \textbf{4.17}$$

Where

‘a’ is the lattice constant, R_O= 1.32 ´ is the radius of oxygen ion and r_A is the mean ionic radii of tetrahedral A-site.

The oxygen parameter ‘u’depends on the chemical composition, preparation conditions and sintering procedure. The ideal ‘u’ value is close to 0.375Å in spinel ferrites.The values of ‘u’ for the investigated samples were higher than the ideal one. This indicates that the crystal lattice deviates from the ideal spinel ferrite because of the difference in the chemical composition. However, the deviation from the ideal crystal structure (Δ) found to vary with Al^{3+} substitution.

4.3.4 Magnetization

Magnetic hysteresis loops for $CoMn_{1-x}Al_xFeO_4$with amaximum applied field of 0.9 T is shown in Figs. 4.21 (a-c).All data of the magnetization parameters are included in Table 4.8 and Figs. 4.22-4.26.The values of saturation magnetization (Ms) is appeared to be lower as compared to that of bulk values of Co-Mn ferrite. Lower saturation magnetisation can be considered as a consequence of the smaller crystallite size, which leads to structural distortion in the external surface. This structural distortion occurs because at the external surface the surface spins have nearest neighbours only on one side and none on the other side (broken exchange bonds)

The variation of saturation magnetization with Al^{3+} substitution is presented in Fig. 4.22. Decrease of saturation magnetization with the Al^{3+}concentration depends upon the three facts:

(1) In spinel ferrite the saturation magnetisation (Ms) depends upon strongest super- exchange coupling (anti parallel coupling) between the tetrahedral A and octahedral B site. The strength of super exchange coupling depends on the bond angles and bond lengths between the cations. The exchange coupling decreases with the decrease of effective bond lengths. In the present samples we have observed from XRD analysis the effective bond lengths. Decrease with the increase of Al^{3+}concentration, which leads to weakening the exchange coupling and hence saturation magnetisation decreases.

(2) $Al^{3+}$is a nonmagnetic ion, which does not take part in the exchange interaction to the nearest neighbour ions and hence the saturation magnetisation affects with the increase of Al^{3+}concentration.

(3) Porosity affects the magnetization process because the pore works as a generator of the demagnetization field. The pores tend to hinder the free movement of the magnetic walls during the magnetization process [59]. As a consequence, the intensity of the effective magnetic field applied to the material is reduced [60]. Increased density reduces the material's porosity. Therefore, a homogeneous and denser microstructure should favor the flow of the magnetic field through the material, improving its magnetic induction. The increase in porosity of the presently investigated samples with Al^{3+} substitution may also play the role in declining the Ms of $CoMn_{1-x}Al_xFeO_4$spinel ferrite.

The observed variation in the saturation magnetization can also be explained due to the difference in the contributions from the magnetic moment of the substituted ion on the A- and B-sites of the $CoMn_{1-x}Al_xFeO_4$spinel ferrite i.e.

$$n_{Bcal.} = M_B - M_A \qquad \textbf{4.18}$$

Where

M_B and M_A are the B and A sub-lattice magnetic moments in μ_B, n_{Bcal}. is termed as calculated magnetic moment.

In the presently investigated ferrite system, decrease in the n_{Bcal}.(Fig. 4.23) is expected after the substitution of Al^{3+} for Mn^{3+} ions, since $Al^{3+}$is a non-magnetic ion with magnetic moment of $0\mu_B$ as compared magnetic Mn^{3+} ion with a large magnetic moment of $4\mu_B$.

The observed magnetic moment ($n_B$obs.) per formula unit in the Bohr magneton (μ_B) was calculated using a relation 4.20 [61]:

$$n_{B_{Obs.}} = \frac{(Mw) \times (Ms)}{5585} \qquad \textbf{4.19}$$

Where

MW is molecular weight of the sample and Ms is the saturation magnetization. It is obvious from Table 4.8 and Fig. 4.23 that the calculated and observed values of the magneton number are in good agreement with each other.

Remanence magnetization (Mr) is also decline (Fig. 4.24) due to Al^{3+} has no remanence; again since it is a soft magnetic material. So, the remanence magnetization comes from the Co, Mn and Fe ions present in the samples.

Fig. 4.25 depicts the compositional variation of the ratio of remnant magnetization (Mr) over saturation magnetization (Ms) at room temperature measurement. In other words, this ratio (Mr/Ms) is called square ness ratio or remanence ratio (R). Remanence ratio is a characteristic parameter of the material and is dependent on the anisotropy, indicating the ease with which the magnetization direction is reoriented to the nearest easy axis magnetization direction after the magnetic field is removed. The lower the *R* value is, the more isotropic the material will be. The values of *R* varied from 0.28 (x = 0.00) to 0.62(x = 1.0) with increasing Al^{3+} substitution. This high remanent ratio is desirable for magnetic recording and memory devices.

Coercivity (Hc) in a ferrite system is known to depend on several parameters such as anisotropy constant, lattice imperfections, internal strains and grain size etc. It can be seen from Fig. 4.26 that the coercivity decreased for x = 0.25, which may be attributed to some extrinsic parameters such as microstructure sand large grain size. However, it should be mentioned here that the observed coercivity variation invariably points out that the variation in the net anisotropy in the system due to the presence of Co^{2+} and ions is the dominant mechanism responsible for determining the coercivity parameters. Further it can be concluded that the substitution of Al^{3+}in Co-Mn ferrite changing material to a soft magnetic materials, which means that Al^{3+} has almost no coercivity.

4.4 Conclusions

- Al^{3+}substituted Co-Mn ferrites nano particles with a chemical formula $CoMn_{1-x}Al_xFeO_4$where x = 0.0, 0.25, 0.5, 0.75, 1.0 were synthesized via the sol-gel auto-combustion method.
- Co-Mn ferrites nano particles synthesized by sol-gel auto-combustion method has been characterized to be single phased cubic spinel belonging to the space group Fd3m.
- The lattice constant of Co-Mn ferrite decreased linearly with the increase of Al^{3+}substitution and may be related to the smaller ionic radii of Al^{3+} ions as compared to that of Mn^{3+} ions.
- The surface morphology were investigated by scanning electron microscopy, shows uniform grain growth of nanometer dimension grains.

- Transmission electron microscopy confirmed the Al^{3+} substituted Co-Mn ferrite particles are in nanometer dimensions.
- Selected area electron diffraction patterns evident the synthesized samples are well crystallized.
- Particle and crystallite size decreased with the Al^{3+} substitution. This eventually increases the porosity and declined the bulk density.
- The occupation number of Co^{2+}, Mn^{3+}, Al^{3+} and Fe^{3+} ions over the tetrahedral A- and octahedral B-sites are affected by the substitution of Al^{3+} ions. Co^{2+} and Al^{3+} ions preferentially occupy octahedral B site. Mn^{3+} ions shows their marked preference towards tetrahedral A-site whereas Fe^{3+} ions are randomly distributed over both A and B sites.
- The variation in occupancies of Co^{2+}, Mn^{3+}, Al^{3+} and Fe^{3+} ions affect the mean ionic radii of tetrahedral (r_A) and octahedral (r_B) site.
- The distribution of the magnetic Co^{2+}, Mn^{3+} and Fe^{3+} ions thus affected by Al^{3+} substitution has interesting effects on magnetic structure. The system maintains ferrimagnetic ordering at room temperature for the whole range of the composition studied. The strength of the magnetic coupling, however, decreases monotonously with increasing Al^{3+} substitution. The increase in non-magnetic Al^{3+} for magnetic Mn^{3+} ions led to a considerable reduction in the saturation magnetization of Co-Mn ferrite.
- Magnetic parameters; remanent magnetization, magnet on number and coercivity is strongly affected with the Al^{3+}substitution. These variations in magnetic parameters were co-related to magnetic structure of Al^{3+} ions and their site occupancies.

References

[1] M.H. Sousa, F.A. Tourinho, J. Depeyrot, G.J. da Silva, M.C.F.L. Lara, J. Phys. Chem.B 105 (2001) 1168–1175.

[2] Sagar E. Shirsath, Mahesh L. Mane, Yukiko Yasukawa, Xiaoxi Liu and Akimitsu Morisako, Phys. Chem. Chem. Phys. 16 (2014) 2347-2357.

[3] Ali Ghasemi, Sagar E. Shirsath, Xiaoxi Liu, and Akimitsu Morisako, J. Appl. Phys. 109 (2011) 07A507

[4] Y.F. Lu, W.D. Song, Appl. Phys. Lett. 76 (2000) 490–492.

[5] A. Baykal, N. Kasapogul, Y. Koseoglu, A.C. Basaran, H. Kavas, M.S. Toprak, Cent.Eur. J. Chem. 6 (1) (2008) 125–130.

[6] C. Venkataraju, G. Sathishkumar, K. Sivakumar, J. Magn. Magn.Mater. 322(2010) 230–233.

[7] Sagar E. Shirsath, Yukiko Yasukawa, Ali Ghasemi, Xiaoxi Liu, and Akimitsu Morisako, J. Appl. Phys. 115 (2014) 17A515.

[8] M.R. Bhandare, H.V. Jamadar, A.T. Pathan, B.K. Chougule, A.M. Shaikh, J. Alloys Compd.509 (2011) L113–L118.

[9] Alex Goldman, Modern Ferrite Technology, 2nd ed. (Springer, New York, 2006).

[10] Zhijian Peng, XiuliFu, HuilinGe, ZhiqiangFu, ChengbiaoWang, LonghaoQi, HezhuoMiao, J.Magn.Magn.Mater. 323 (2011) 2513–2518

[11] C. Breschignag, P. Houdy, M. Lahmani (Eds.), Nano materials and Nano chemistry, Springer-Verlag, 2006 (Chapter 5).

[12] J.P. Chen, C.M. Sorensen, K.J. Klabunde, G.C. Hadjipanayis, E. Devlin, A. Kostikas,Phys. Rev. B 54 (9) (1996) 9288.

[13] Sagar E. Shirsath, R. H. Kadam, Anil S. Gaikwad, Ali Ghasemi, Akimitsu Morisako, J.Magn.Magn.Mater.323 (2011) 3104–3108.

[14] R.H. Kodama, A.E. Berkowitz, E.J. McNiff, S. Goner, Phys. Rev. Lett. 77 (4) (1996)394.

[15] H. Shenker, Phys. Rev. 107 (1957) 1246.

[16] T. Hyeon, Chem. Commun. 8 (2003) 927.

[17] M. Walker, P.I. Mayo, K. O’Grady, S.W. Charles, R.W. Chantrell, J. Phys. Condens. Matter 5 (1993) 2779

[18] S. Chikazumi, Physics of Ferromagnetism, second ed., Oxford University Press, New York, 1997.

[19] Y. Koseoglu, H. Kavas, B. Aktas¸, Phys. Status Solidi (a) 203(2006) 1595–1601.

[20] R.D. Mc Michael, R.D. Shull, L.J. Swartzendruber, L.H. Bennett, R.E.Watson, Magnet ocaloric effect in super paramagnets, J. Magn. Magn.Mater. 111 (1992) 29–33.

[21] A. Ghasemi, A. Hossienpour, A. Morisako, A. Saatchi, M. Salehi, J. Magn. Magn.Mater. 302 (2006) 429–435.

[22] Y. Sahoo, M. Cheon, S. Wang, H. Luo, E.P. Furlani, P.N. Prasad,J. Phys. Chem. B 108(2004) 3380–3383.

[23] J.A. Paulsen, C.C.H. Lo, J.E. Snyder, A.P. Ring, L.L. Jones, D.C. Jile , J. Appl. Phys. 97 (2005) 044502.

[24] M. Atif,R.Sato-Turtelli,R.Grössinger, F.Kubel , J. Appl. Phys. 113 (2013) 153902.

[25] S.D. Bhame,P.A.Joy, J. Phys. D:Appl. Phys. 40(2007)3263–3267.

[26] S. J. Haralkar, R. H. Kadam, S. S. More, Sagar E. Shirsath, M. L. Mane, Swati Patil, D. R. Mane, Mater. Res. Bull. 48 (2013) 1189–1196

[27] N. Ravah, I.C. Nlebedim, Y. Melikhov, J.E. Snyder, P.I. Williams, A.J. Moses, D.C. Jiles, IEEE Trans. Magn. 45 (10) (2009) 4261–4264.

[28] D.H. Chen, Y.Y. Chen, Mater. Res. Bull. 37 (2002) 801–810.

[29] S. M. Patange, Sagar E. Shirsath, G. S. Jangam, K. S. Lohar, S. S. Jadhav, K. M. Jadhav, J. Appl. Phys. 109 (2011) 053909

[30] V. Uskokovi´ c1, D. Makovec, M. Drofenik, Mater. Sci. Forum 494 (2005) 155–160.

[31] Z.F. Zi, Y.P. Sun, X.B. Zhu, Z.R. Yang, J.M. dai, W.H. Song, J. Magn. Magn.Mater.320 (2008) 2746–2751.

[32] M.M. Hessien, M.M. Rashad, K. El-Barawy, J. Magn. Magn.Mater. 320 (2008)336–343.

[33] Sagar E. Shirsath, R. H. Kadam, S. M. Patange, M. L. Mane, Ali

Ghasemi, Akimitsu Morisako, Appl. Phys.Lett.100 (2012) 042407.

[34] Y. Wang, Q. Li, C. Zhang, H. Jing, J. Alloys Compd. 467 (2009) 284–287.

[35] Y. Wang, Q. Li, C. Zhang, B. Li, J. Magn. Magn.Mater. 321 (2009) 3368–3372.

[36] H. Sato, T. Umeda, J. Mater. Trans. 34 (1993) 76–81.

[37] J. Ding, W.F. Miao, P.G. McCormick, R. Street, J. Alloys Compd. 281 (1998) 32–36.

[38] W.A. Kaczmarek, B. Idzikowski, K.H. Muller, J. Magn. Magn.Mater. 177 (1998)921–922.

[39] S.V. Ketov, Y.D. Yagodkin, A.L. Lebed, Yu.V. Chernopyatova, K. Khlopkov, J. Magn.Magn.Mater. 300 (2006) 479–481.

[40] X. Yang, Q. Li, J. Zhao, B. Li, Y. Wang, J. Alloys Compd. 475 (2009) 312–315.

[41] L. You, L. Qiao, J. Zheng, M. Jiang, L. Jiang, J. Sheng, J. Rare Earth 26 (2008) 81–84.

[42] S. Chaudhury, S.K. Rakshit, S.C. Parida, Z. Singh, K.D.S. Mudhera, V. Venugopal,J. Alloys Compd. 455 (2008) 25–30.

[43] Y.P. Fu, C.H. Lin, K.Y. Pan, J. Alloys Compd. 349 (2003) 228–231.

[44] Y.P. Fu, C.H. Lin, J. Alloys Compd. 386 (2005) 222–227.

[45] F. Tabatabaie, M.H. Fathia, A. Saatchia, A. Ghasemia, J. Alloys Compd. 470 (2009)332–335.

[46] J.F. Wang, C.B. Ponton, R. Grossinger, I.R. Harris, J. Alloys Compd. 369 (2004)170–177.

[47] I. Perelshtein, N. Perkas, S. Magdassi, T. Zioni, M. Royz, Z. Maor, A. Gedanken, J.Nanopart. Res. 10 (2008) 191–195.

[48] B. D. Cullity, Elements of X-ray diffraction, Addison-Wesley, London, 1959.

[49] A. R.Denton, N. W.Ashcroft, Phys. Rev. B. 43 (1991) 3161–3164.

[50] R.D. Waldron, Phys. Rev. 99 (1955) 1727.

[51] M.A. Amer, Phys. Status Solidi B 237/2 (2003) 459.

[52.] V.I. Nikolaev, V.S. Rusakov, N.I. Chistyakova, Phys. Status Solidi A 91 (1982) K139.

[53] V. Potakova, N. Zvera, V. Romanov, Phys. Status Solidi A 12 (1972) 623.

[54] H.A. Dawoud, S.K. Shaat, J. Al-Aqsa Univ. 10 (2006) 247.

[55] Hugh St.C. O’Neill, Alexandra Navrotsky,American Mineralogist 68 (1983) 181–194.

[56] L. Weil, F.Bertaut, L.Bochirol, J. Phys. Radium, 11 (1950) 208.

[57] R.Valenzuela, Magnetic ceramics, Cambridge University Press, 1994.

[58] K.J. Standley, Oxide magnetic materials, (Clarendon Press, Oxford, 1972).

[59] A. Globus, J. Phys. (38) (1977) (C1)1–(C1)15.

[60] H. Igarashi, K. Okazaki, J. Am. Ceram. Soc. 60 (1–2) (1976) 51–54.

[61] L. Néel, Ann. Phys. Paris, 3 (1948) 137.

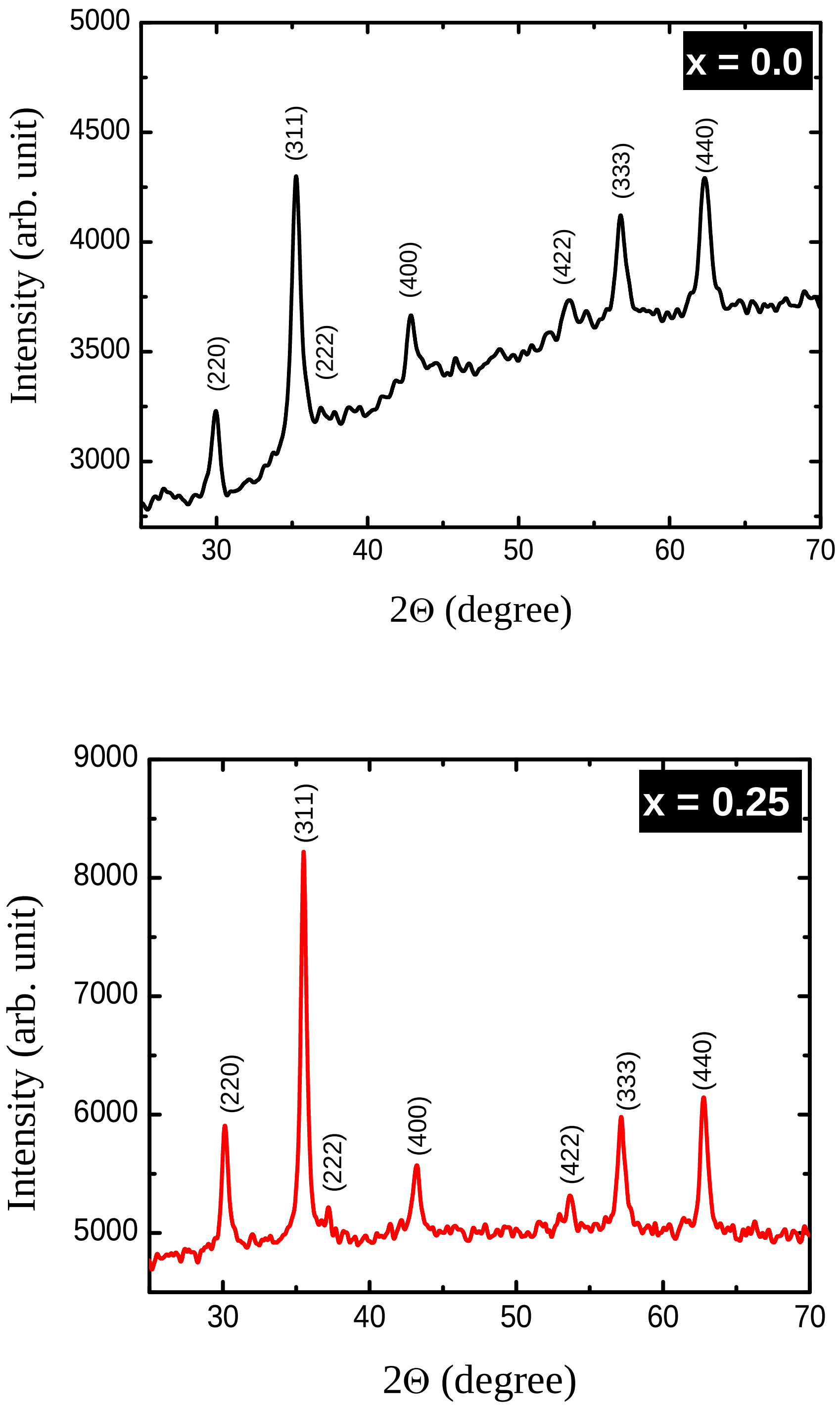

Fig. 4.1 (a): X-Ray diffraction patterns of x = 0.0 and x = 0.025 for $CoMn_{1-x}Al_xFeO_4$

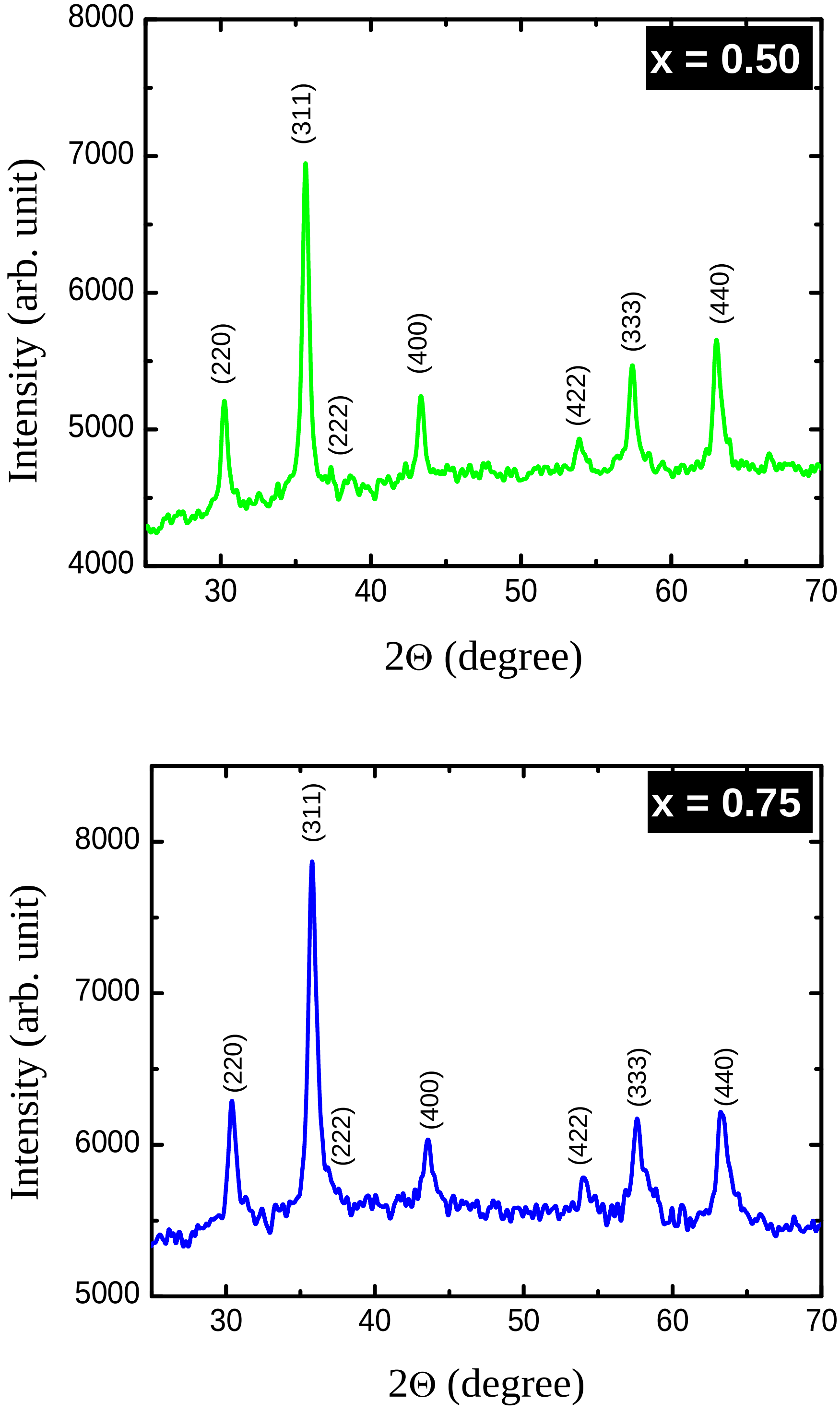

Fig. 4.1 (b): X-Ray diffraction patterns of x = 0.50 and x = 0.075 for $CoMn_{1-x}Al_xFeO_4$

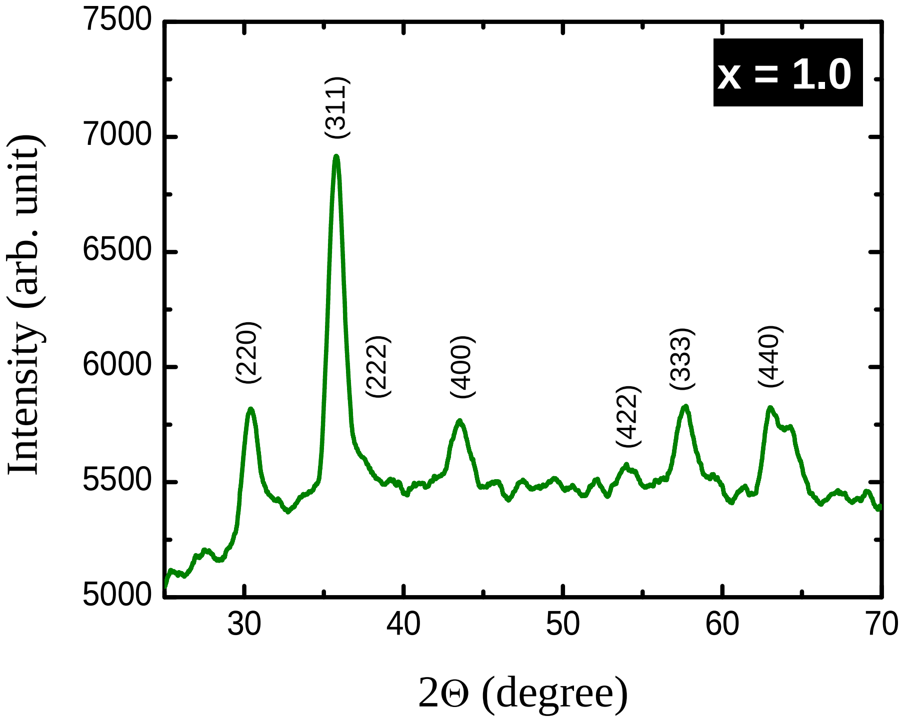

Fig. 4.1 (c): X-Ray diffraction patterns of x = 1.00 for $CoMn_{1-x}Al_xFeO_4$

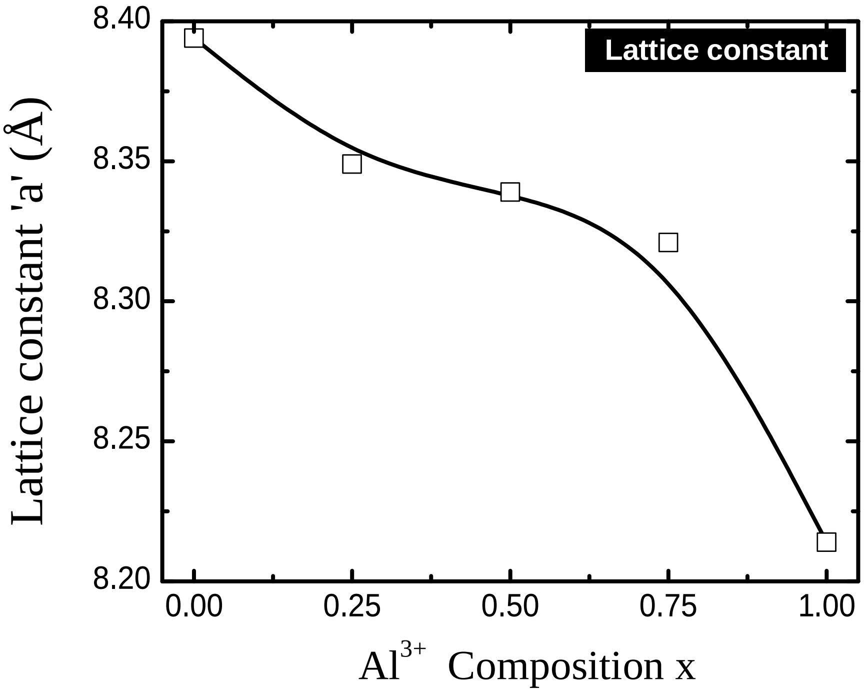

Fig. 4.2: Variation of lattice constant with Al^{3+} composition x for $CoMn_{1-x}Al_xFeO_4$.

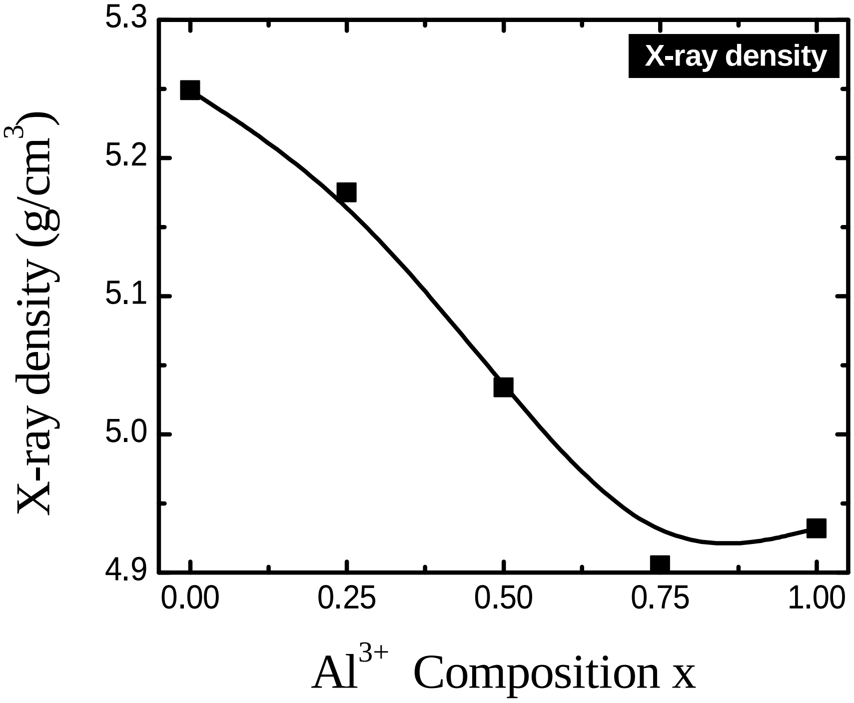

Fig. 4.3: Variation of X-ray density Al^{3+} composition x for $CoMn_{1-x}Al_xFeO_4$.

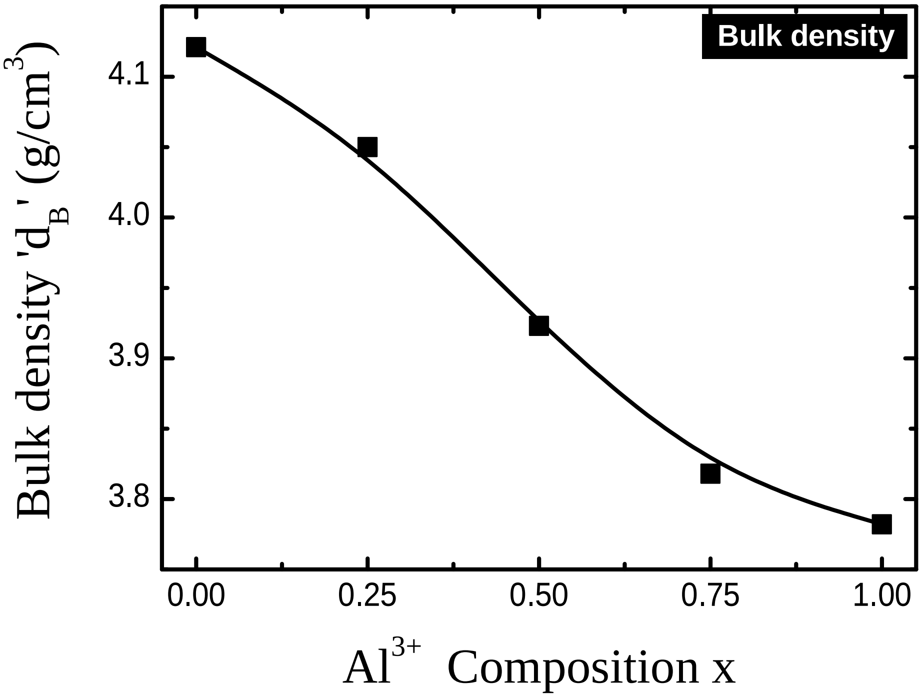

Fig. 4.4: Variation of bulk density (d_B) with Al^{3+} composition x for $CoMn_{1-x}Al_xFeO_4$.

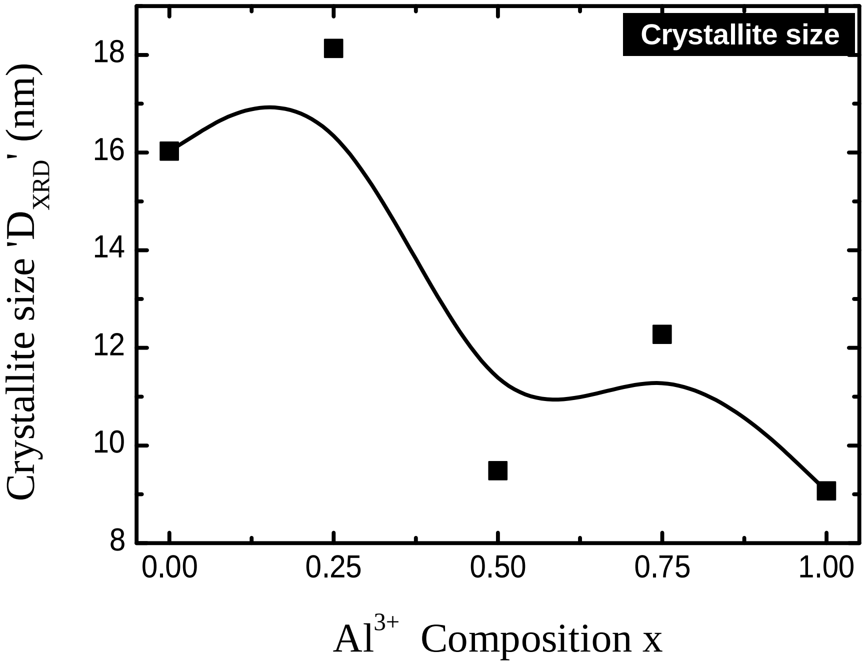

Fig. 4.5: Variation of crystallite size (D_{xrd}) with Al^{3+} composition x for $CoMn_{1-x}Al_xFeO_4$.

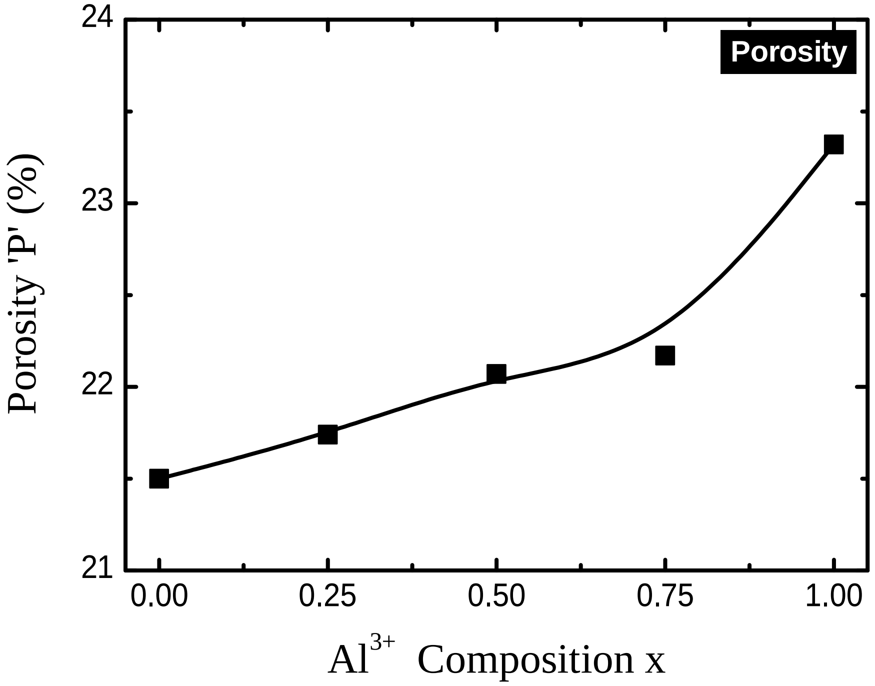

Fig. 4.6: Variation of porosity (P) with Al^{3+} composition x for $CoMn_{1-x}Al_xFeO_4$.

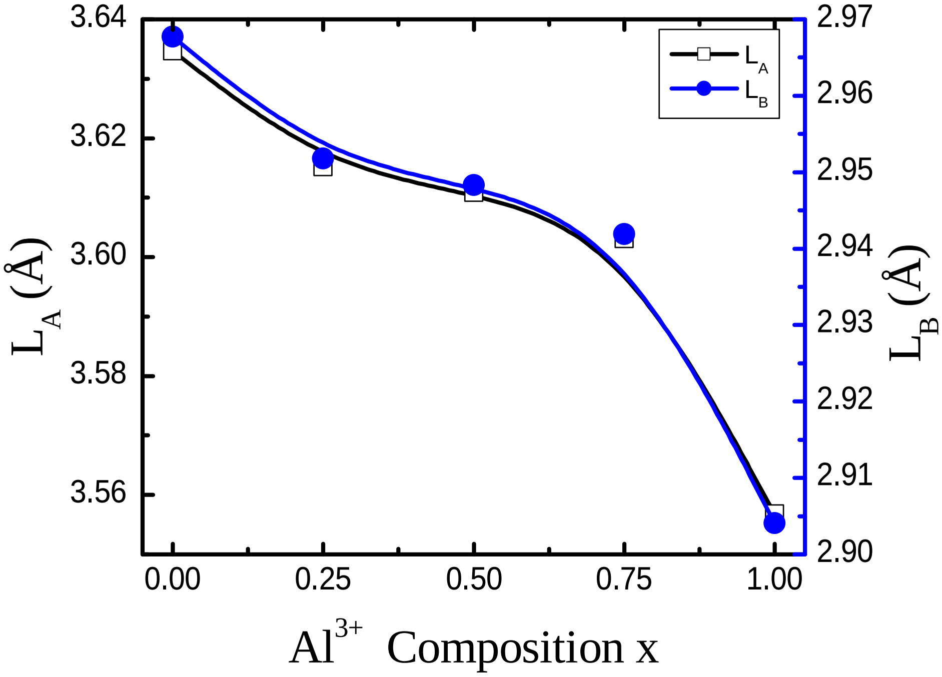

Fig. 4.7: Variation of hopping lengths (L_A and L_B) with Al^{3+} composition x for $CoMn_{1-x}Al_xFeO_4$.

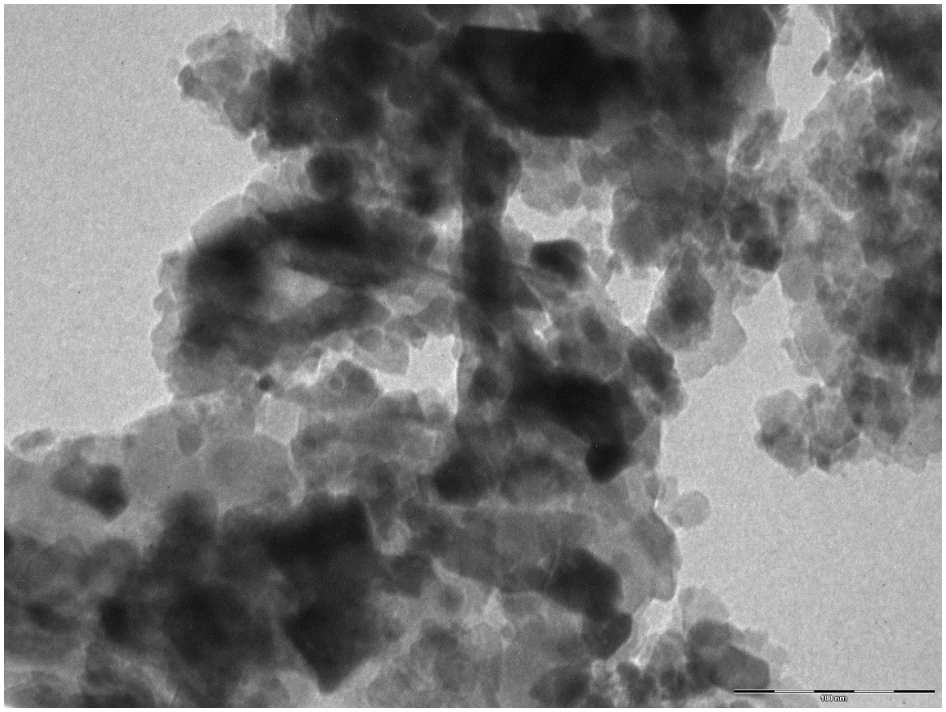

Fig. 4.8 (a). Transmission electron micrograph (TEM) image of x = 0.0 for $CoMn_{1-x}Al_xFeO_4$

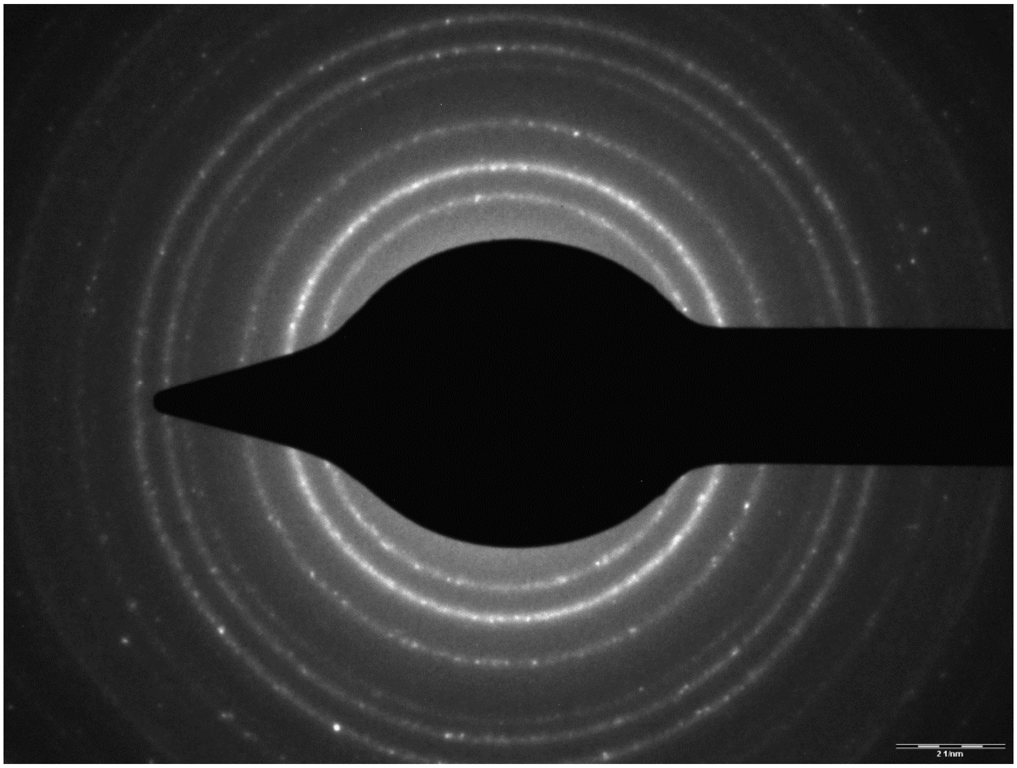

Fig. 4.8 (b). Selected area electron diffraction (SAED) image of x = 0.0 for $CoMn_{1-x}Al_xFeO_4$

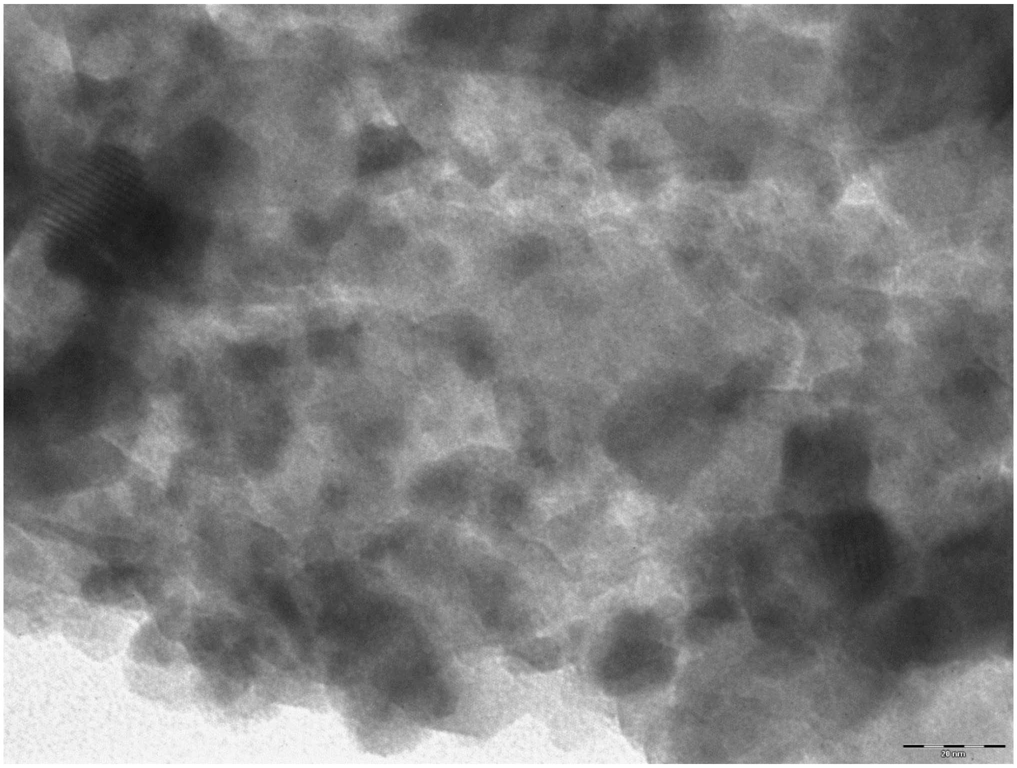

Fig. 4.9 (a). Transmission electron micrograph (TEM) image of x = 1.0 for $CoMn_{1-x}Al_xFeO_4$

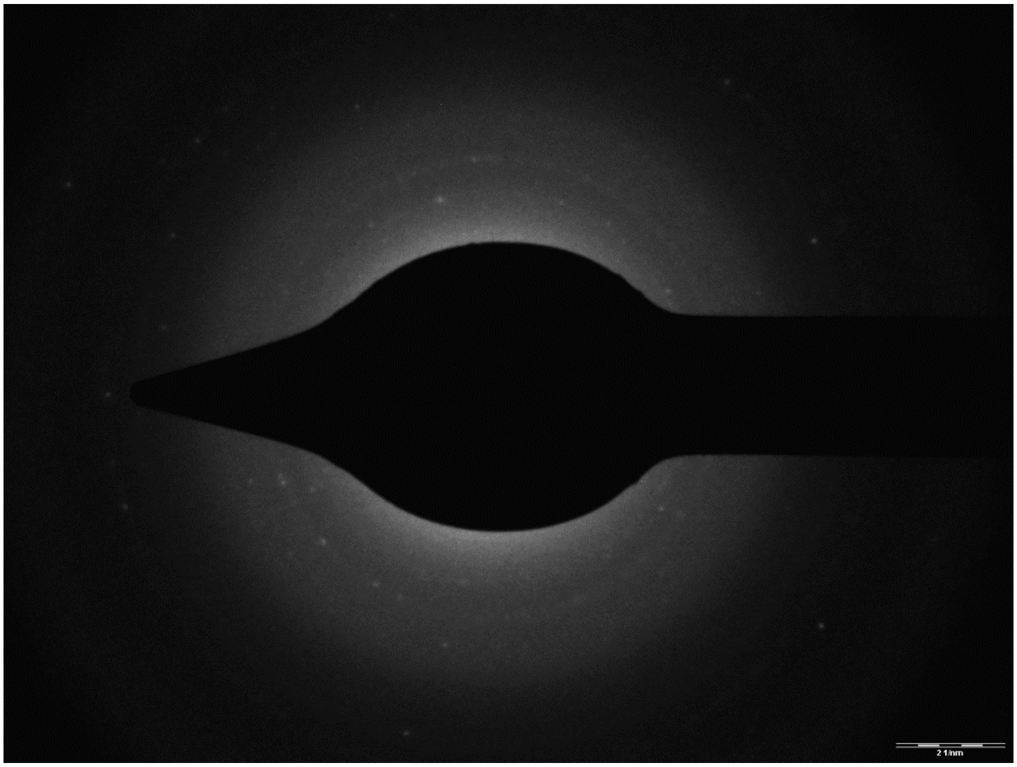

Fig. 4.9 (b). Selected area electron diffraction (SAED) image of x = 1.0 for $CoMn_{1-x}Al_xFeO_4$

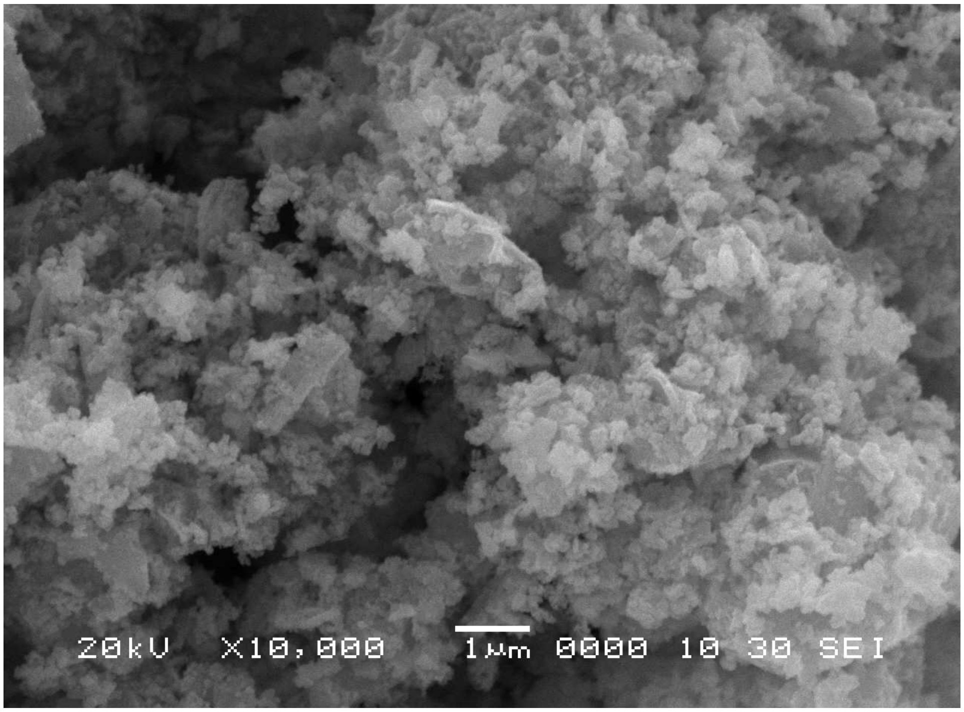

Fig. 4.10 (a). Scanning electron micrograph (SEM) image of x = 0.0 for $CoMn_{1-x}Al_xFeO_4$

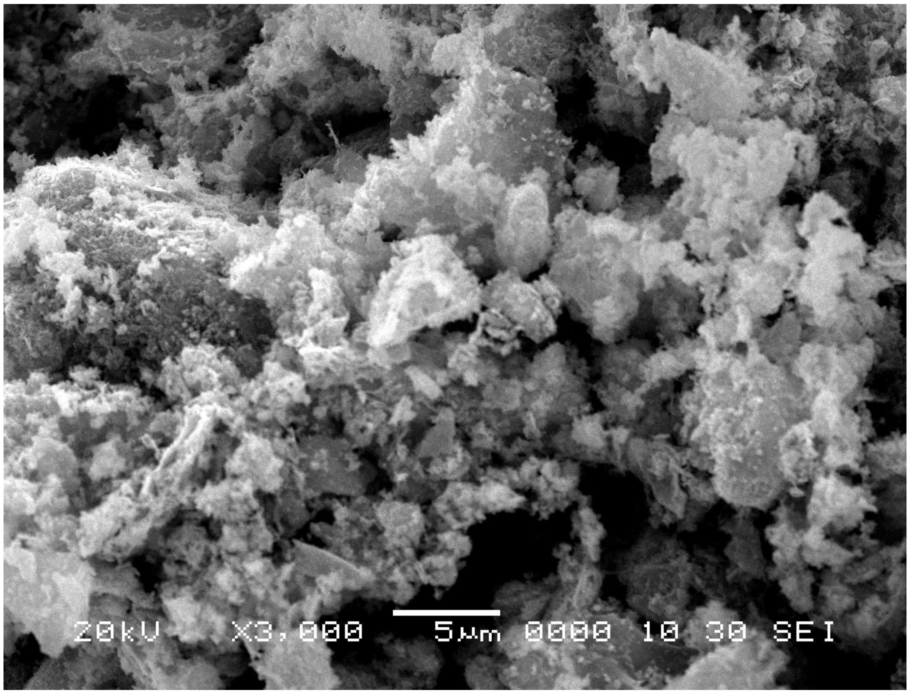

Fig. 4.10 (b). Scanning electron micrograph (SEM) image of x =1.0 for $CoMn_{1-x}Al_xFeO_4$

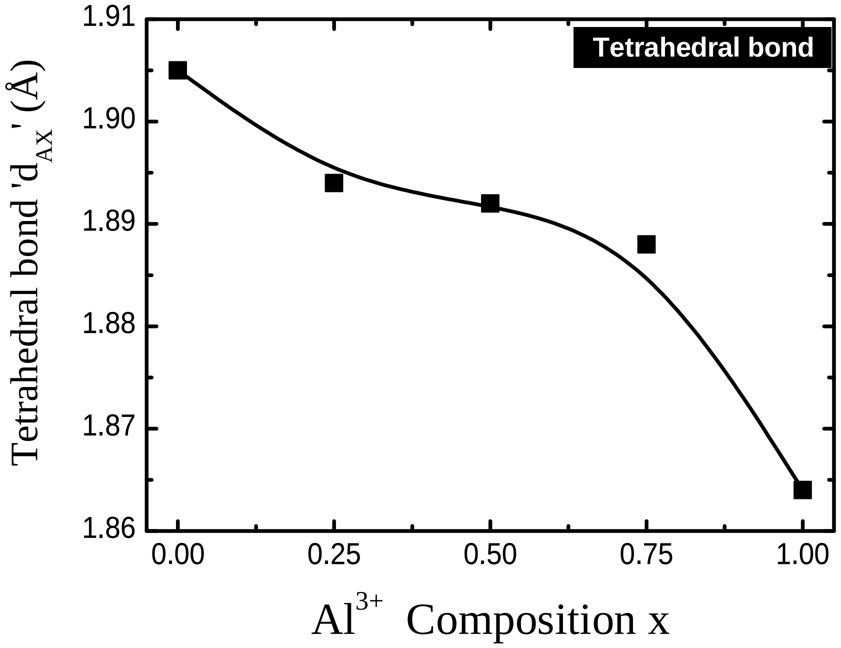

Fig. 4.11: Variation of Tetrahedral bond (d_{AX}) with Al^{3+} composition x for $CoMn_{1-x}Al_xFeO_4$.

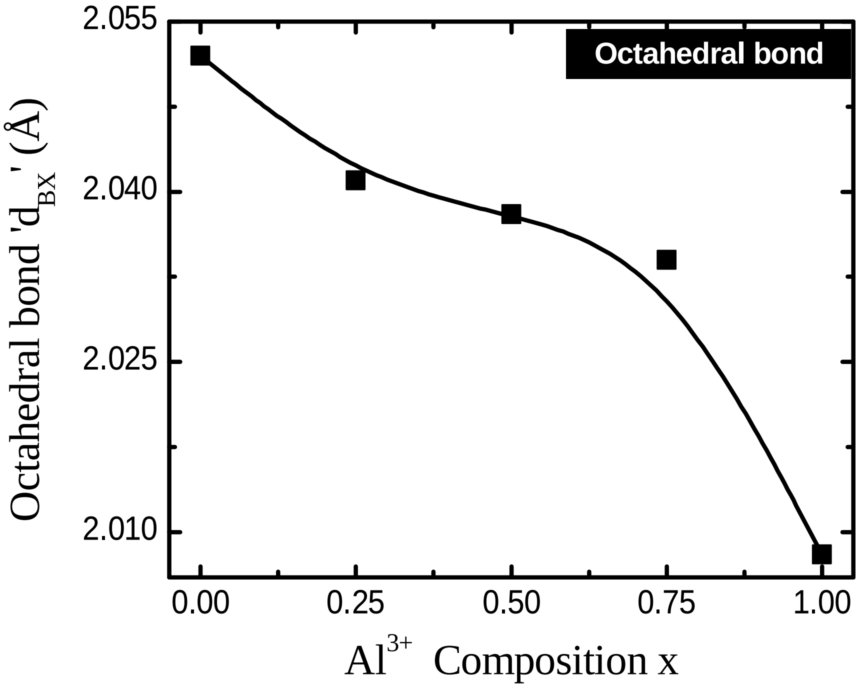

Fig. 4.12: Variation of octahedral bond (d_{BX}) with Al^{3+} composition x for $CoMn_{1-x}Al_xFeO_4$.

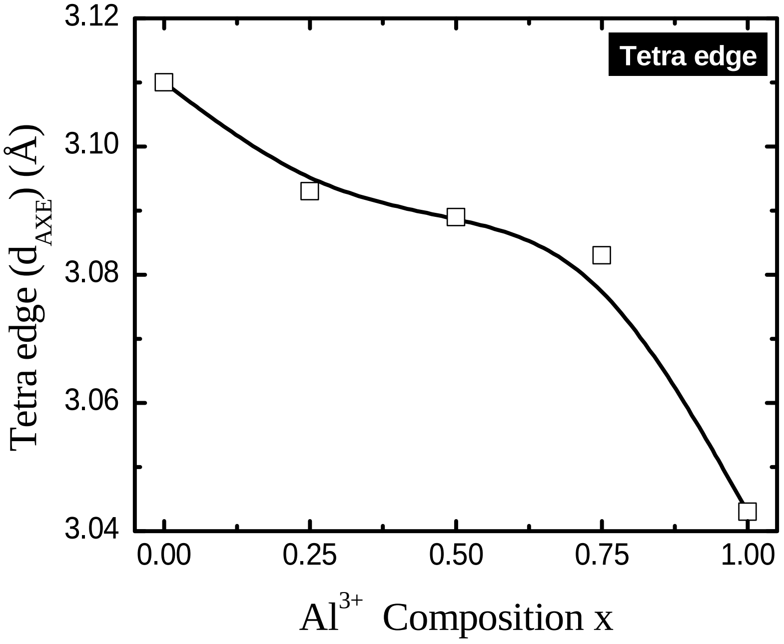

Fig. 4.13: Variation of tetra edge (d_{AXE}) with Al^{3+} composition x for $CoMn_{1-x}Al_xFeO_4$.

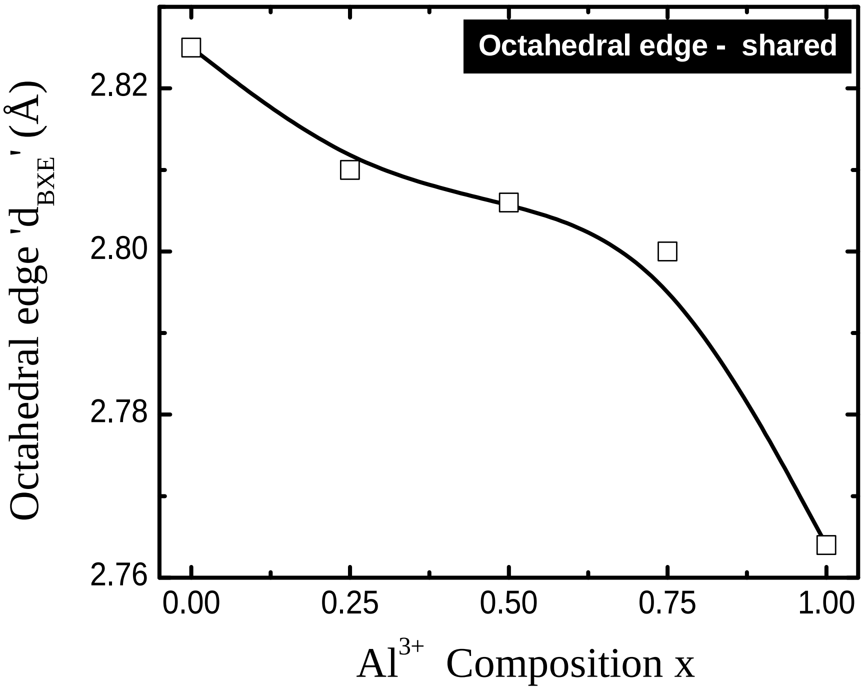

Fig. 4.14: Variation of octahedral edge- *shared* (d_{BXE}) with Al^{3+} composition x for $CoMn_{1-x}Al_xFeO_4$.

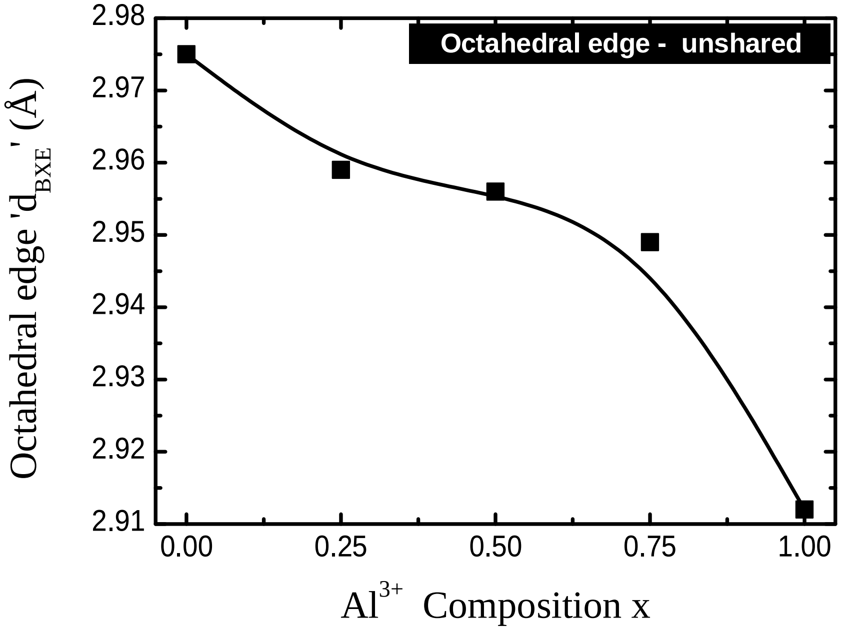

Fig. 4.15: Variation of octahedral edge- *unshared* (d_{BXE}) with Al^{3+} composition x for $CoMn_{1-x}Al_xFeO_4$.

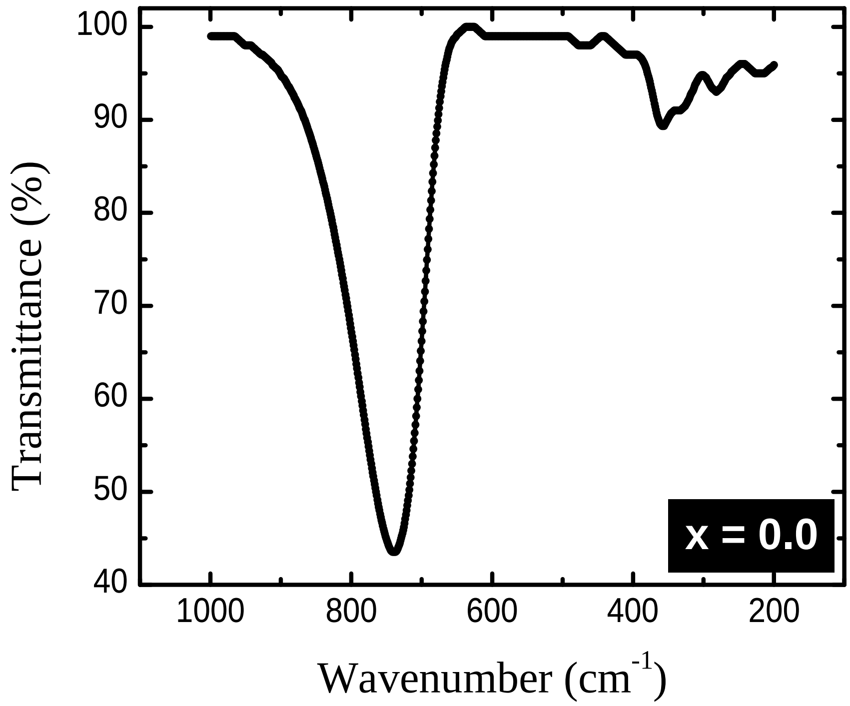

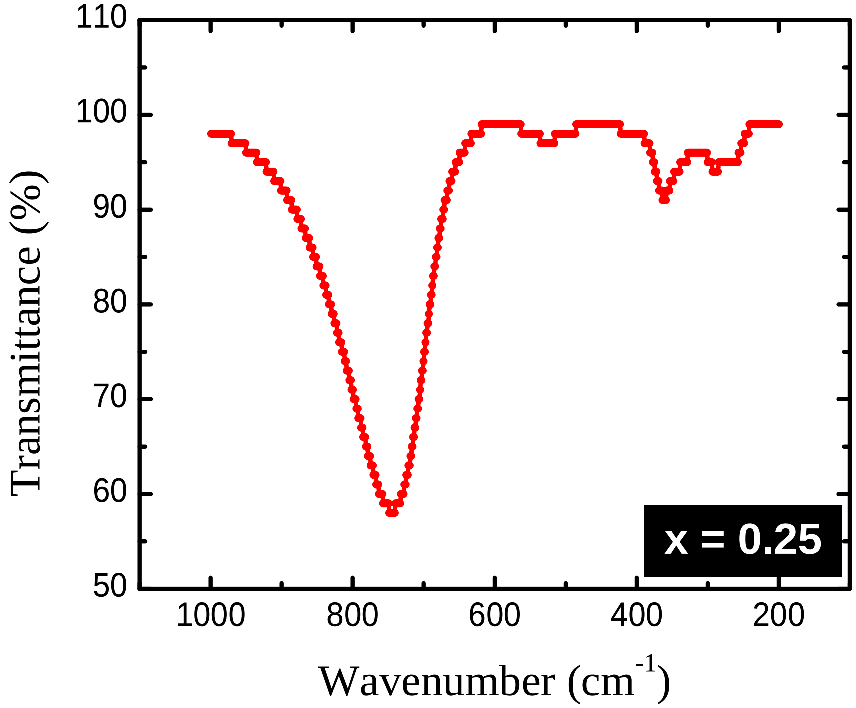

Fig. 4.16 (a): Infrared spectra of x = 0.00 and x = 0.25 for $CoMn_{1-x}Al_xFeO_4$

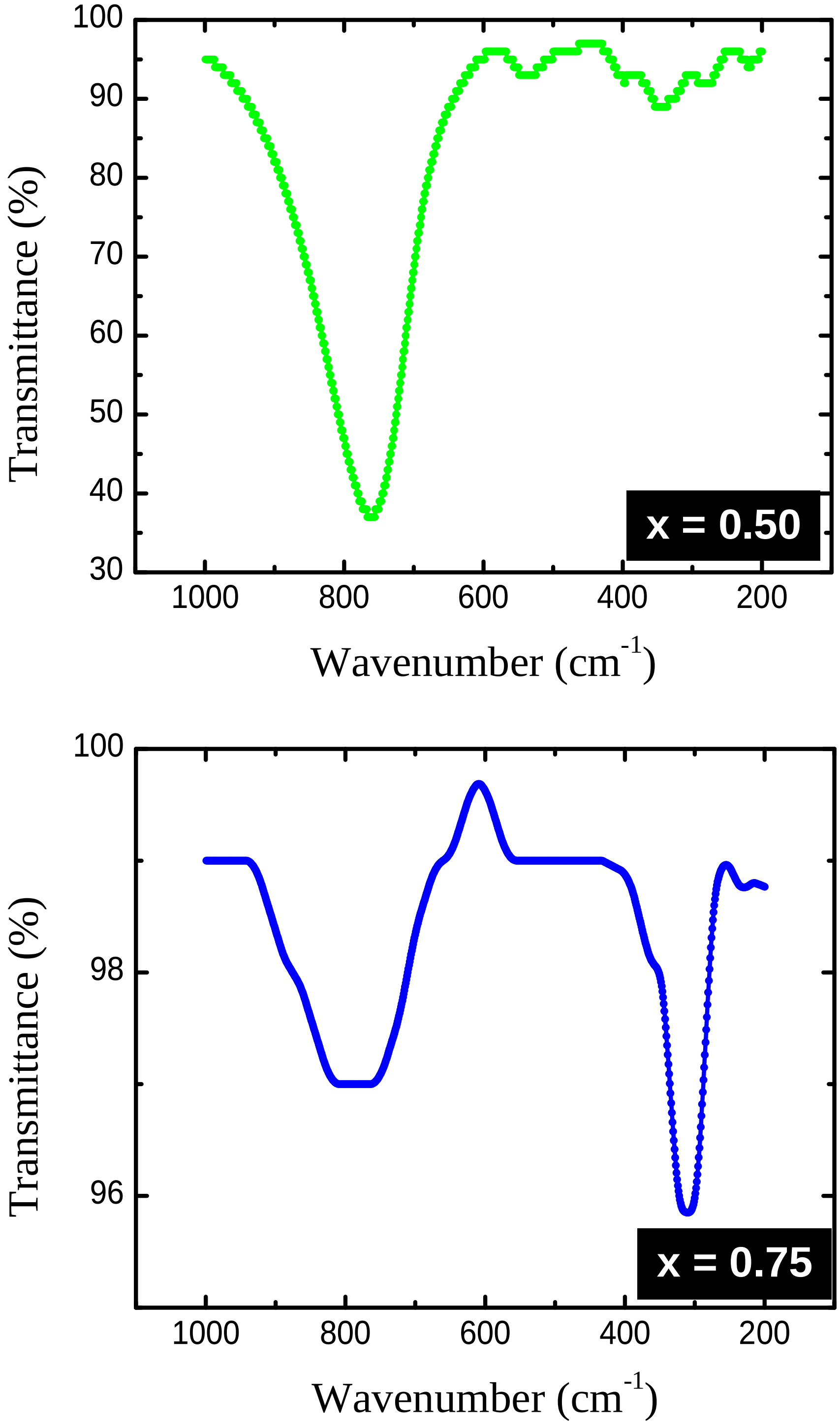

Fig. 4.16 (b): Infrared spectra of x = 0.50 and x = 0.75 for $CoMn_{1-x}Al_xFeO_4$

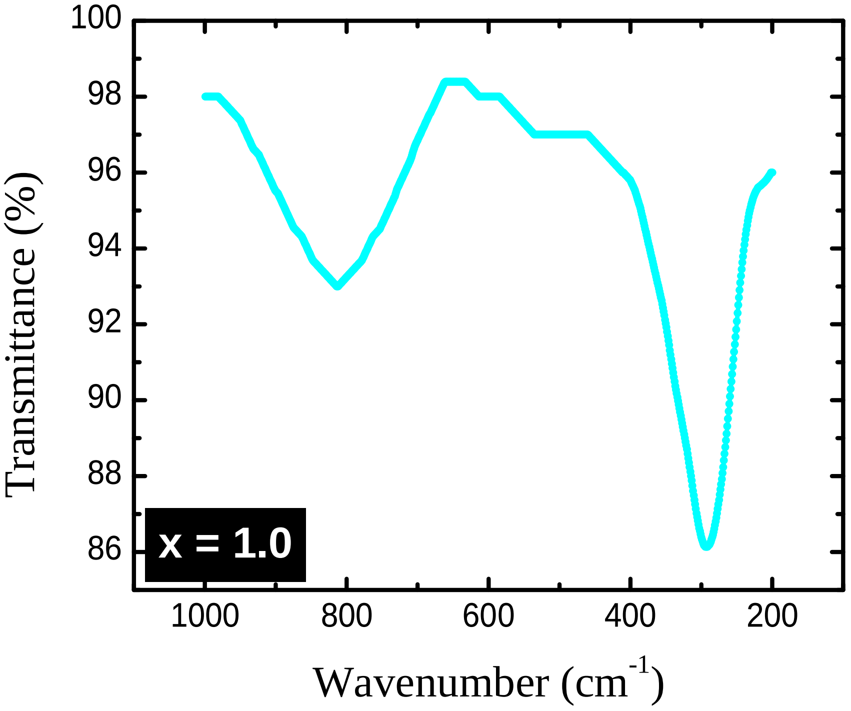

Fig. 4.16 (c): Infrared spectra of x = 1.0 for $CoMn_{1-x}Al_xFeO_4$

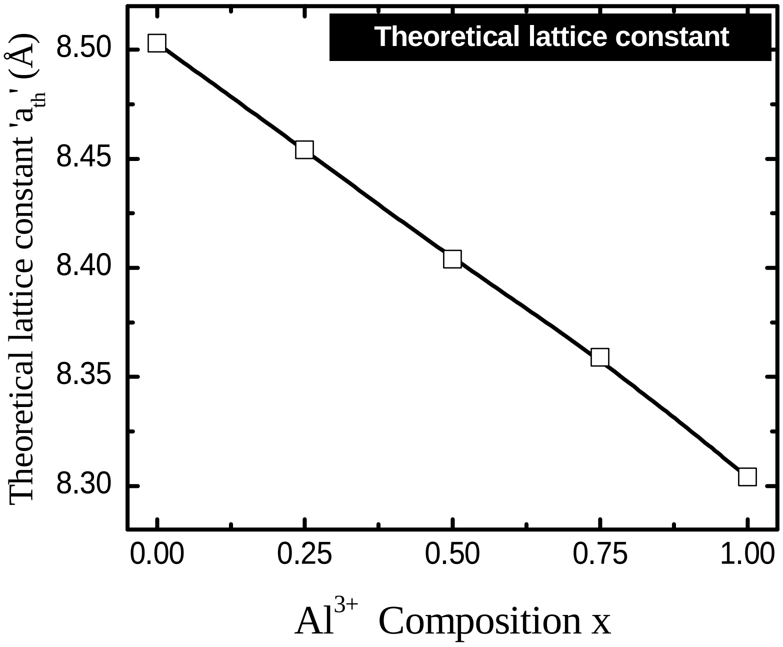

Fig. 4.17: Variation of theoretical lattice constant (a_{th}) with Al^{3+} composition x for $CoMn_{1-x}Al_xFeO_4$.

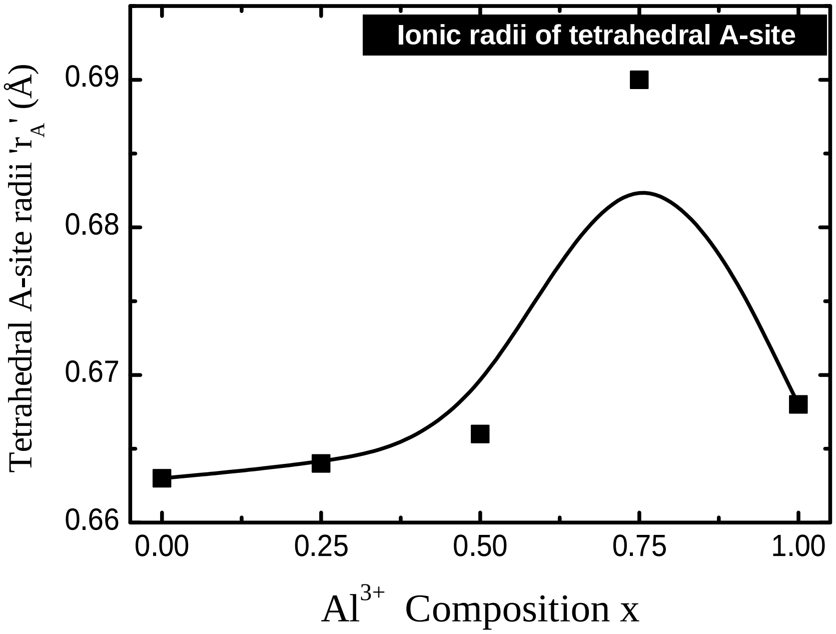

Fig. 4.18: Variation of site tetrahedral A-site ionic radii (r_A) with Al^{3+} composition x for $CoMn_{1-x}Al_xFeO_4$.

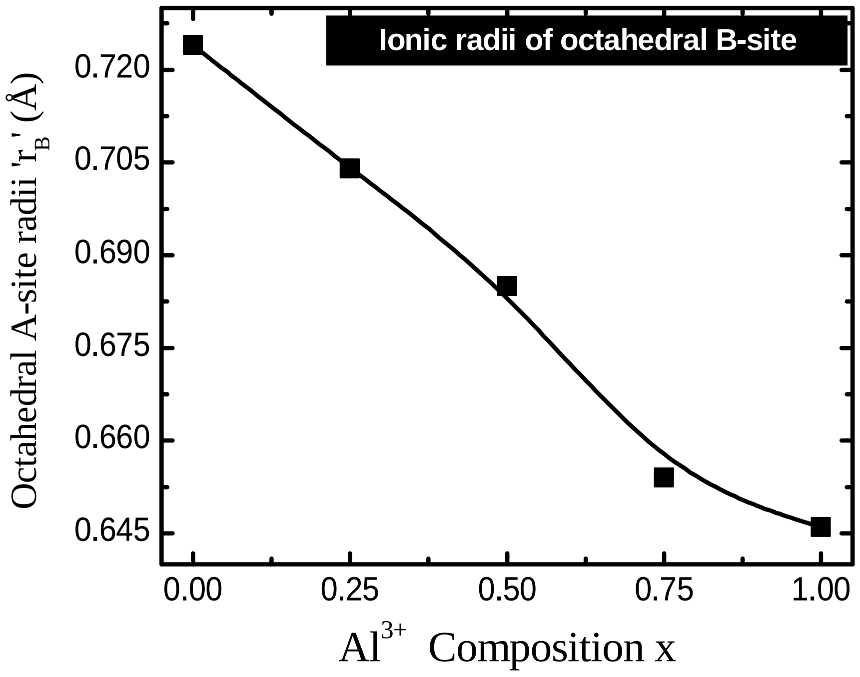

Fig. 4.19: Variation of site octahedral B-site ionic radii (r_B) with Al^{3+} composition x for $CoMn_{1-x}Al_xFeO_4$.

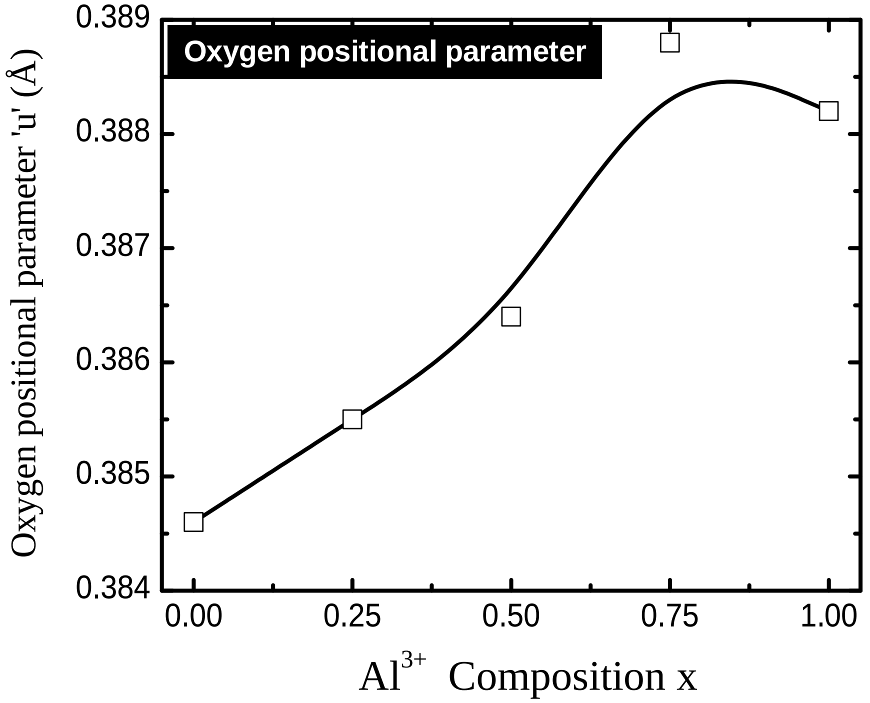

Fig. 4.20: Variation of oxygen parameter (u) with Al^{3+} composition x for $CoMn_{1-x}Al_xFeO_4$.

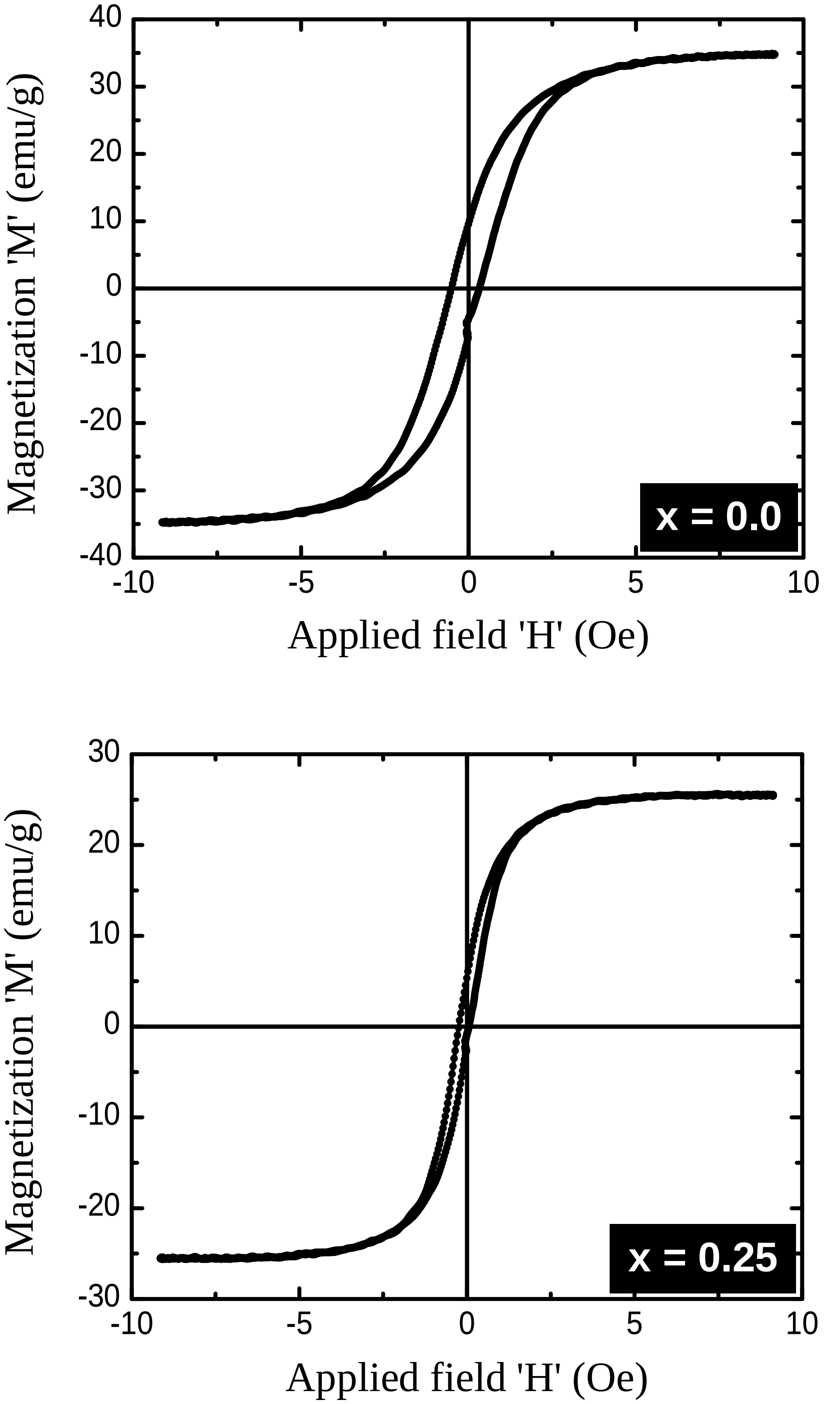

Fig. 4.21 (a): Variation of magnetization (M) with applied field (H) of x = 0.00 and x = 0.25 for $CoMn_{1-x}Al_xFeO_4$

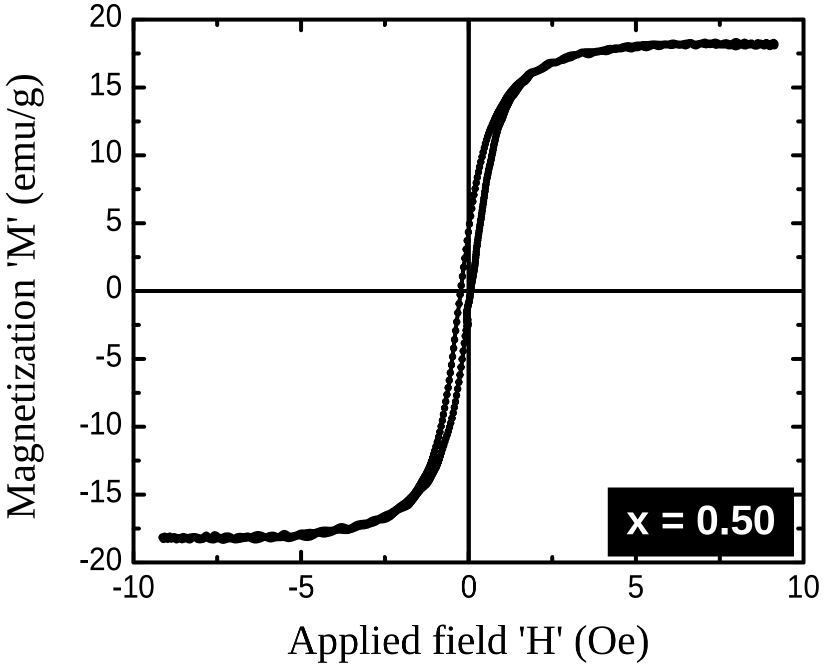

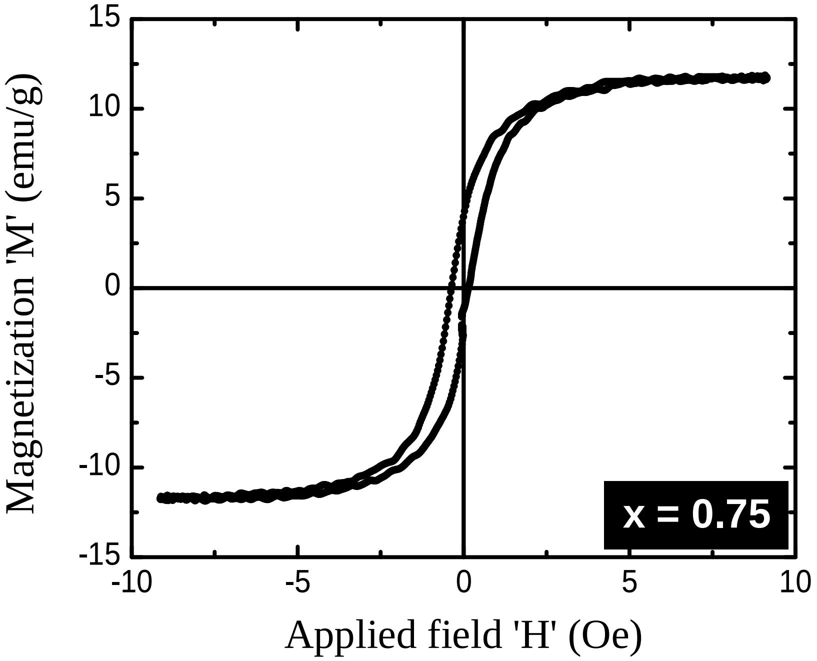

Fig. 4.21 (b): Variation of magnetization (M) with applied field (H) of x = 0.50 and x = 0.75 for $CoMn_{1-x}Al_xFeO_4$

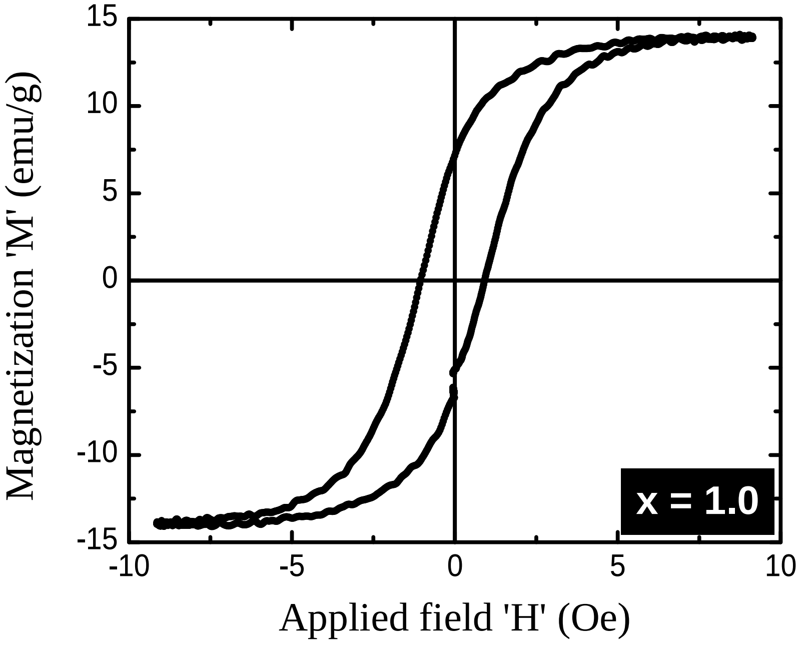

Fig. 4.21 (c): Variation of magnetization (M) with applied field (H) of x = 1.00 for $CoMn_{1-x}Al_xFeO_4$

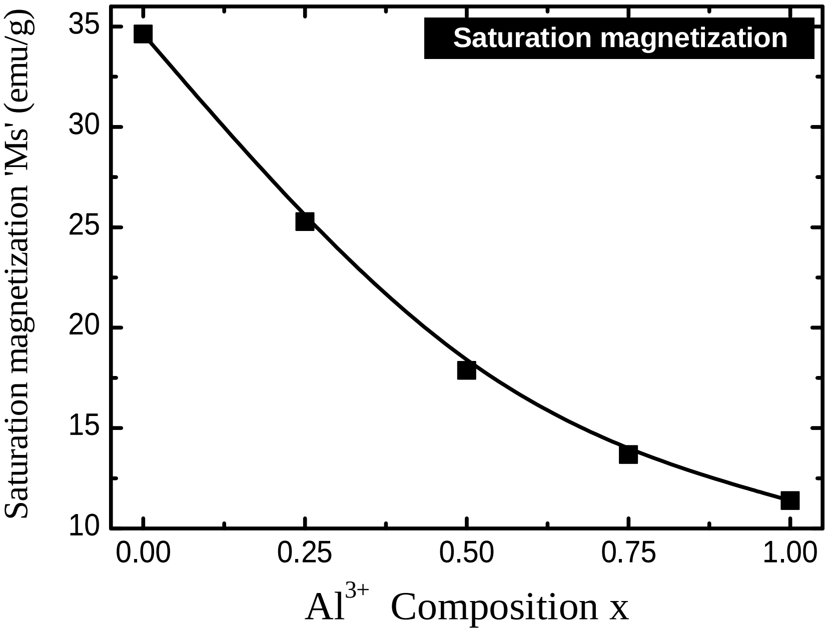

Fig. 4.22: Variation of saturation magnetization (Ms) with Al^{3+} composition x for $CoMn_{1-x}Al_xFeO_4$.

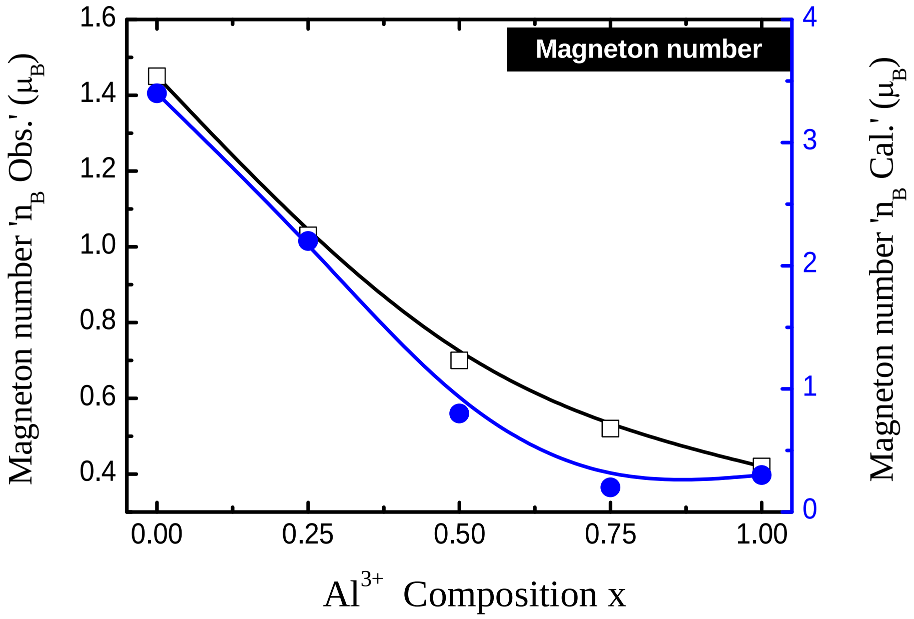

Fig. 4.23: Variation of observed (n_B Obs.) and calculated (n_B Cal.) magneton number with Al^{3+} composition x for $CoMn_{1-x}Al_xFeO_4$.

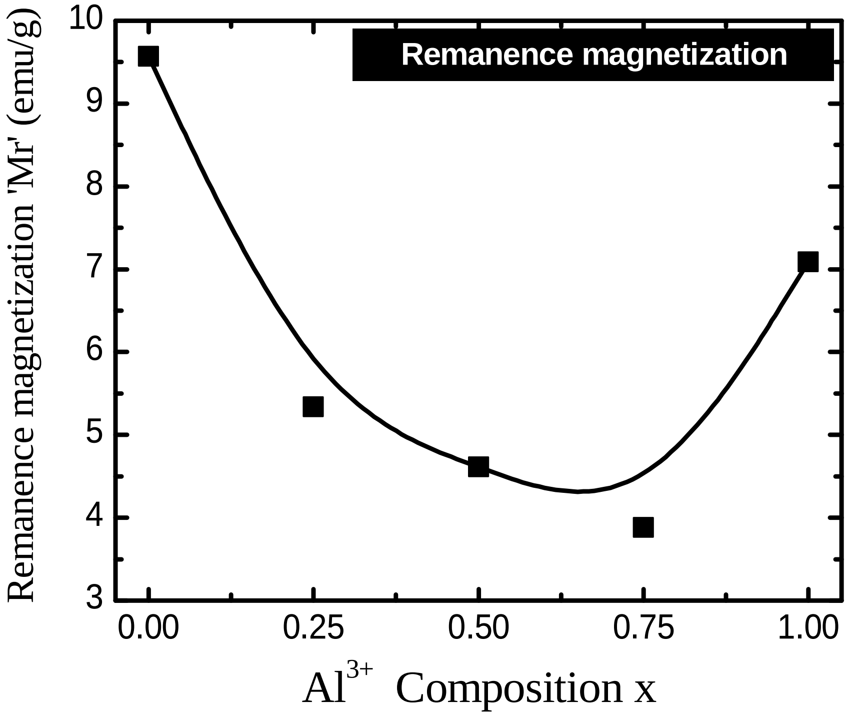

Fig. 4.24: Variation of remanence magnetization (Mr) with Al^{3+} composition x for $CoMn_{1-x}Al_xFeO_4$.

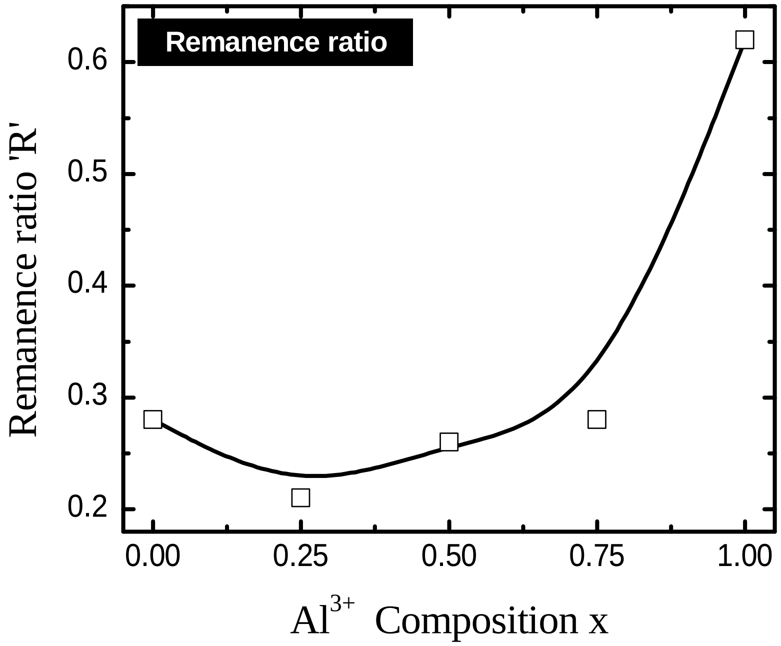

Fig. 4.25: Variation of remanence ratio (R) with Al^{3+} composition x for $CoMn_{1-x}Al_xFeO_4$.

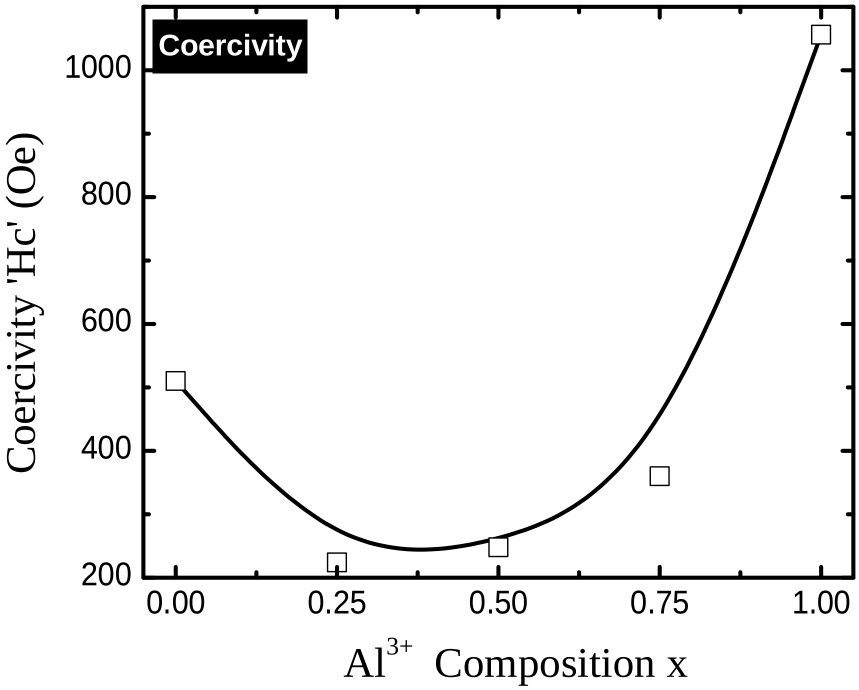

Fig. 4.26: Variation of coercivity (Hc) with Al^{3+} composition x for $CoMn_{1-x}Al_xFeO_4$.

Table 4.1

Theoretical percentage of element in $CoMn_{1-x}Al_xFeO_4$ ferrites.

Comp. x	Theoretical %				
	Co	**Mn**	**Al**	**Fe**	**O**
0.00	25.2159	23.506	0.0000	23.8954	27.3822
0.25	25.2955	17.686	5.5795	23.9709	27.4686
0.50	25.3756	11.828	11.1943	24.0468	27.5556
0.75	25.4563	5.933	16.8448	24.1232	27.6431
1.00	25.5374	0.000	22.5313	24.2001	27.7312

Table 4.2

Lattice constant (a), X-ray density (d_x), crystallite size (D_{XRD}), bulk density (d_B) and porosity (P) of $CoMn_{1-x}Al_xFeO_4$

Comp. x	a (Å)	dx (g/cm^3)	D_{XRD} (nm)	d_B (g/cm^3)	P (%)
0.00	8.394	5.249	16.028	4.121	21.50
0.25	8.349	5.175	18.132	4.050	21.74
0.50	8.339	5.034	9.482	3.923	22.07
0.75	8.321	4.905	12.276	3.818	22.17
1.00	8.214	4.932	9.070	3.782	23.32

Table 4.3

Hopping lengths (L_A and L_B) of $CoMn_{1-x}Al_xFeO_4$

Comp. x	Hopping length	
	L_A (Å)	L_B (Å)
0.00	3.6347	2.9677
0.25	3.6152	2.9518
0.50	3.6109	2.9483
0.75	3.6031	2.9419
1.00	3.5568	2.9041

Table 4.4

Tetrahedral bond (d_{AX}), octahedral bond (d_{BX}), tetra edge (d_{AXE}) and octahedral edge (d_{BXE}) (shared and unshared) of $CoMn_{1-x}Al_xFeO_4$

Comp. x	d_{AX} (Å)	d_{BX} (Å)	Tetra edge (Å) d_{AXE}	Octa edge d_{BXE} (Å)	
				Shared	unshared
0.00	1.905	2.052	3.110	2.825	2.975
0.25	1.894	2.041	3.093	2.810	2.959
0.50	1.892	2.038	3.089	2.806	2.956
0.75	1.888	2.034	3.083	2.800	2.949
1.00	1.864	2.008	3.043	2.764	2.912

Table 4.5

IR absorption bands of $CoMn_{1-x}Al_xFeO_4$

Comp. x	□$_1$ (cm^{-1})	□$_2$ (cm^{-1})	□$_3$ (cm^{-1})	□$_4$ (cm^{-1})
0.00	742	358	533	283
0.25	746	364	527	280
0.50	763	349	539	278
0.75	787	320	550	229
1.00	816	299	534	---

Table 4.6

Cation distribution of $CoMn_{1-x}Al_xFeO_4$

Comp. x	Cation distribution	
	A-site	**B-site**
0.00	$Mn_{0.7}Fe_{0.3}$	$Co_{1.0}Mn_{0.3}Fe_{0.7}$
0.25	$Mn_{0.6}Fe_{0.4}$	$Co_{1.0}Mn_{0.15}Al_{0.25}Fe_{0.6}$
0.50	$Mn_{0.4}Fe_{0.6}$	$Co_{1.0}Mn_{0.1}Al_{0.5}Fe_{0.4}$
0.75	$Co_{0.2}Mn_{0.2}Fe_{0.6}$	$Co_{0.8}Mn_{0.05}Al_{0.75}Fe_{0.4}$
1.00	$Co_{0.2}Al_{0.15}Fe_{0.65}$	$Co_{0.8}Al_{0.85}Fe_{0.35}$

Table 4.7

Ionic radii of tetrahedral A-site (r_A), octahedral B-site (r_B), theoretical lattice constant (a_{th}) and oxygen positional parameter (u) of $CoMn_{1-x}Al_xFeO_4$

Comp. ‘x’	r_A (Å)	r_B (Å)	a_{th} (Å)	u (Å)
0.00	0.663	0.724	8.503	0.3846
0.25	0.664	0.704	8.454	0.3855
0.50	0.666	0.685	8.404	0.3864
0.75	0.690	0.654	8.359	0.3888
1.00	0.668	0.646	8.304	0.3882

Table 4.8

Saturation magnetization (Ms), remanence magnetization (Mr), remanence ratio (R), magneton number (η_B) and coercivity (Hc) of $CoMn_{1-x}Al_xFeO_4$

Comp. x	Ms (emu/g)	M_r (emu/g)	R	η_B (μ_B) Obs.	η_B (μ_B) Cal.	Hc (Oe)
0.00	34.63	9.57	0.28	1.45	3.40	510
0.25	25.28	5.34	0.21	1.03	2.20	224
0.50	17.87	4.61	0.26	0.70	0.80	248
0.75	13.68	3.88	0.28	0.52	0.20	360
1.00	11.39	7.09	0.62	0.42	0.30	1056

Chapter 5

Results and discussion on $CoMn_{1-x}Cr_xFeO_4$

5.1 Introduction

Application and synthesis of nano materials is the subject of intense research now a days because of their unique physical and chemical properties, which makes them very appealing from the point of view of the scientific value of understanding their properties along with the technological significance of enhancing the performance of existing materials [1–9]. There are two main factors which make nano materials to behave significantly different than that of bulk materials:

(i) surface effects that causing smooth properties scaling due to the fraction of atoms at the surface, and

(ii) Quantum effects (showing discontinuous behavior due to quantum confinement effects in materials with delocalized electrons) [10].

These above two factors dominantly affect the chemical reactivity of nano materials and physical properties such as; mechanical, optical, electrical and magnetic properties.

Research into the synthesis and characterization of magnetic materials has been conducted for more than a century. The importance of magnetic materials in our daily life ranges from electric motors and magnetic storage devices to Brio toy trains. Recently, the ability to produce nanometer-scale magnetic materials has opened new applications for magnetic materials [11].

Magnetic nano particles exhibit unique properties and have promising technological applications in high density recording, color imaging, Ferro fluids, high frequency devices and magnetic refrigerators [12, 13]. Nano particles of magnetic ceramic materials are also widely used as contrasting agents in magnetic resonance imaging (MRI), replacement of radioactive materials used as tracers and delivery of drugs to specific areas of the human body. From the application point of view, the most significant properties of magnetic ceramic materials namely; magnetic saturation,coercivity and magnetization, change drastically as the size of the particles move down into the nano metric range [14–17].

Magnetic spinel ferrites nano particles having general formula AB_2O_4 are of vital importance from both basic science point of view and technological applications point of view. In ferrite ‘A’ is divalent metal ion and ‘B’ is trivalent metal ion. The structural and electrical properties are very much sensitive to the methodology adopted for the synthesis and synthesis parameters. Normally, in AB_2O_4 structure divalent ion is bigger in size than that of trivalent ion. Former occupies octahedral site while latter occupies tetrahedral site with some exceptions. Spinel ferrites are commercially important materials because of their excellent magnetic and electrical properties. Interesting physical and chemical properties of the magnetically diluted ferrites arise from the ability of these compounds to distribute the cations amongst the available tetrahedral A- and octahedral B-sites. Ferrites are able to fulfill a wide range of applications from microwave to radio frequencies, are of great importance from both fundamental and applied research points of view [18-21]

Polycrystalline soft ferrite are magnetic semi-conductors which cannot be replaced by any other magnetic material, because ferrites are stable, relatively inexpensive, easily manufactured and have widespread applications in electronics and communications industries due to their interesting electrical and magnetic properties [22]. Ferrites are also used for magnetic application such as transformer cores, noise filters and recording heads, etc. due to their excellent magnetic properties such as high initial permeability and high saturation magnetization. However, ferrites have certain limitation for magnetic applications at high frequencies because of their low resistively and therefore high eddy current losses.

Cobalt ferrite ($CoFe_2O_4$) corresponds to the group of spinel-type ferrites, which are compounds with a cubic oxygen lattice of the general formula $Me_xFe_{3-x}O_4$ [23],where Me is usually a divalent metal cation. Fe_3O_4 (magnetite) is the prototype of an inverse spinel ferrite, with a cation distribution of (Fe^{3+}) $[Fe^{3+}Fe^{2+}]$ O_4. In this structural formula, the parentheses denote tetrahedral oxygen coordinated sites (A sites) and the square brackets denote the octahedral sites (B sites). The interstices of the coordination tetrahedral are too small for the larger Fe^{2+} ions, thus these sites are occupied by Fe^{3+}ions only. In $CoFe_2O_4$, it has been found that a certain percentage of Co^{2+} ions (up to 24% of the ions in the tetrahedral site), being smaller than Fe^{2+}, may replace theFe^{3+} ions at the tetrahedral sites, while the majority of the Co^{2+} ions occupy the octahedral sites. It is thus impossible to refer to the cobalt ferrite lattice as having either the normal or the inverse spinel structure [24]. The rest of the Co^{2+} ions replace the Fe^{2+} ions in the octahedral sites [25].

The properties of ferrites are mainly depending upon chemical composition, method of preparation, sintering time and temperature [26]. Introducing small amount of a foreign ion can change the electrical and magnetic properties of the ferrite [27].$CoMn_{1-x}Cr_xFeO_4$spinel ferrite nano particulate system may offers an opportunity to study the roles of Co^{2+}, Mn^{3+} and Fe^{3+} in spinel ferrites through the variation of Cr^{3+} ion concentration. Cr^{3+} ions usually occupy the octahedral B sites in spinels. A decrease in total magnetic moment at B sites is expected as Cr^{3+} with a magnetic moment of $3\mu_B$ replaces the stronger Mn^{3+} ($4\mu_B$) cation. Cr^{3+} ion has an electron configuration of $t_{2g}{}^3e_g{}^0$ in spinel structure, which theoretically has a relatively large orbital angular momentum. The Mn^{3+} ion at the B site has $t_{2g}{}^3e_g{}^1$ electron configuration in spinel structure, which theoretically has a zero orbital angular momentum. Therefore, the substitution of Mn^{3+} by Cr^{3+} in$CoMn_{1-x}Cr_xFeO_4$nanoparticles should also offer certain information on the contribution from the orbital angular momentum toward magnetic properties.Cr^{3+} substitution could be complicated since the exchange couplings between Cr^{3+} ions display a large negative exchange constant (J_{B-B}) [28]. A strong negative J_B Interaction favors antiparallel alignment. Although such an arrangement is hindered in mixed spinel ferrites, it could disrupt the parallel alignment of spins on the B site to various extents and lead to spin canting. When $x = 1$ ($CoCrFeO_4$), magnetic frustration has been observed in bulk samples [29, 30]. Therefore, it is also fundamentally interesting to see if the magnetic order has been altered in nano particles by Cr^{3+} substitution.

5.2 Experimental

5.2.1 Synthesis methodology

The wide applications of nano sized ferrites lead to the development of various synthesis methods, which include hydrothermal, ultrasonically assisted hydrothermal, mechanical alloying, pulsed wire discharge, shockwave, reverse micelle co-precipitation, freeze drying, spray drying, precursor and sol–gel [31–41]. The sol–gel method, in particular, is one of the most useful and attractive techniques for the synthesis of nano sized ferrite materials because of its advantages such as; good stoichio metric control and the production of ultra fine particles with a narrow size distribution in a relatively short processing time at very low temperature. Sol–gel methods generally refer to the hydrolysis and condensation of metalalkoxides or alkoxide precursors, leading to dispersions of oxide particles in a “sol”. The “sol” is then dried or “gelled” by solvent removal or by chemical reaction. In general water is used as the solvent, but the precursors can also be hydrolyzed by an acidic or basic medium. The catalysis process induces the formation of colloidal swell as polymeric form of the gel [42,43]. The properties of final products depend upon the rates of hydrolysis and condensation reactions. Smaller particles can be obtained at slower and more controlled hydrolysis rates. The size of the particle can be varied by changing the solution composition, pH, and temperature [sagar].

Analytical reagent grade cobalt nitrate ($Co(NO_3)_2·3H_2O$), chromium nitrate ($Cr(NO_3)_3·9H_2O$), manganese nitrate ($Mn(NO_3)_2·6H_2O$),iron nitrate ($Fe(NO_3)_3·9H_2O$) and citric acid ($C_6H_8O_7·H_2O$),were used to synthesize the $CoMn_{1-x}Cr_xFeO_4$ (x = 0.0, 0.25, 0.5, 0.75, 1.0) ferrite nano particles. In the presented study sol-gel auto-combustion method was adopted to synthesize the ferrite nanoparticles. Reaction procedure was carried out in air atmosphere without protection of inert gases. The molar ratio of metal nitrates to citric acid was taken as 1:3. The metal nitrates were dissolved together in a minimum amount of double distilled water to get a clear solution. An aqueous solution of citric acid was mixed with metal nitrates solution, then ammonia solution was slowly added to adjust the pH at 7. Then the solution was heated at 90 ºC to transform into gel. When ignited at any point of the gel, the dried gel burnt in a self-propagating combustion manner until all gels were completely burnt out to form a fluffy loose powder. The auto-combustion was completed within a minute, yielding the brown-colored ashes termed as a precursor. It has been observed that the calcinations temperature is an important parameter during the synthesis of ferrite nano particles via sol–gel method which affects the physical and magnetic properties of ferrites nano particles. Therefore, the as prepared ferrite powder was annealed at 600 ºC for 4 h in order to compete the crystallization. Theoretical percentage of the elements in the finally synthesized $CoMn_{1-x}Cr_xFeO_4$ferrite sample is shown in Table 5.1.

5.2.2 Characterizations techniques

The crystal structure of the as-prepared samples was characterized by X-ray diffraction technique using Phillips X-ray diffract meter (Model 3710) equipped with Cu-K_α radiation (λ=1.5405Å). The microstructure was examined on the fracture surfaces of the samples using thermal field emission scanning electron microscope (SEM). Transmission electron microscope (TEM) measurements were recorded on Philips (Model CM 200). The samples were prepared by dispersing the powders in acetone and dropping the suspension on a lacey carbon film supported on a 300-mesh copper grid. The infrared spectra of all the samples were recorded at room temperature in the range 300 cm^{-1} to 800 cm^{-1} using Perkin Elmer infrared spectrophotometer. Room temperature magnetization of the samples was measured using the pulse field magnetization set-up.

5.2.1 Formulae

The lattice parameters have been computed using the d-spacing values and the respective (h k l) parameters from the classical formula given in Eq.5.1 [45]:

$$a = \frac{\lambda}{2}\frac{\sqrt{(h^2 + k^2 + l^2)}}{\sin\theta} \qquad 5.1$$

Where

d is the inter-planer spacing and (*hkl*) is the index of the XRD reflection peak.

The X-ray density (dx) of all the samples of the series was obtained by the following relation:

$$dx = \frac{8M}{Na^3} \qquad 5.2$$

where

'8' is the number of molecules per unit cell, 'M' is the molecular weight of sample, 'N' is the Avogadro's number and 'a' is lattice constant.

The crystallite size of the nano crystalline samples were measured from XRD line broadening analysis applying Scherrer's formula [45]:

$$D_{XRD} = \frac{k\lambda}{\beta\cos\theta} \qquad 5.3$$

Where

$D_{XRD}$is the dimension of the crystallites, λ the wavelength of the X-ray radiation, θ the Bragg angle, k is a shape factor taken to be 0.94and β the peak width measured at half of the maximum intensity.

The percentage porosity (P) is calculated using the following relation:

$$\mathrm{P} = \left(\frac{\mathrm{d_X} - \mathrm{d_B}}{\mathrm{d_X}}\right)\times 100 \qquad 5.4$$

Where

dx and d_B are the X-ray density and bulk density respectively.

L_A and L_B i.e. the hopping length for tetrahedral A- and octahedral B-sites respectively were calculated using the following relation:

$$L_A = a\sqrt{\frac{3}{4}} \qquad 5.5$$

$$L_A = a\sqrt{\frac{2}{4}} \qquad 5.6$$

Using the experimental values of lattice constant '*a*', oxygen positional parameter '*u*' (0.375 Å) and substituting using the following equations, the allied parameters such as tetrahedral and octahedral bond length (d_{Ax} and d_{Bx}), tetrahedral edge, shared and unshared octahedral edge (d_{AXE}, d_{BXE} and d_{BXEU}) were calculated:

$$d_{AX} = a\sqrt{3}\left(u - \frac{1}{4}\right) \tag{5.7}$$

$$d_{BX} = a\left[3u^2 - \left(\frac{11}{4}\right)u + \frac{43}{64}\right]^{\frac{1}{2}} \tag{5.8}$$

$$d_{AXE} = a\sqrt{2}\left(2u - \frac{1}{2}\right) \tag{5.9}$$

$$d_{BXEshaired} = a\sqrt{2}\,(1 - 2u) \tag{5.10}$$

$$d_{BXEunshaired} = a\left(4u^2 - 3u + \frac{11}{16}\right)^{\frac{1}{2}} \tag{5.11}$$

Theoretical lattice parameter (a_{th}) were calculated using the following equation [46]:

$$a_{th} = \frac{8}{3}\sqrt{3}\left[(r_A + R_0) + \sqrt{3}(r_B + R_0)\right] \tag{5.12}$$

Where

r_A and r_B are radii of tetrahedral (A) site and octahedral [B] site, R_O is radius of oxygen i.e. (R_O = 1.32 Å).

The value of oxygen position parameter were calculated using the relation [47]:

$$u = \left[(r_A + R_0)\frac{1}{\sqrt{3a}} + \frac{1}{4}\right] \tag{5.13}$$

Where

'a' is the lattice constant, R_O= 1.32 Å is the radius of oxygen ion and r_A is the mean ionic radii of tetrahedral A-site.

The observed magnetic moment ($n_B$obs.) per formula unit in the Bohr magnet on (μ_B) was calculated using a relation 5.14[48]:

$$n_{B\,Obs.} = \frac{(Mw) \times (Ms)}{5585} \tag{5.14}$$

Where

MW is molecular weight of the sample and Ms is the saturation magnetization.

5.3 Results and discussion

5.3.1 Structural Analysis

Fig. 5.1 (a-c) shows the room-temperature X-ray diffraction pattern for all the investigated samples. The result of indexing the XRD pattern showed that the nominal composition structure is single-phase cubic with no reflections other than those belonging to the spine structure with Fd3m cubic spinel space group. The reflection from the planes, (2 2 0), (3 1 1), (2 2 2), (4 0 0), (4 2 2), (333) and (4 4 0) appeared for all samples. All the samples shows cubic spinel structure and the patterns are similar in the whole composition range where Miller indices (i.e.*h, k, l* values) in this range of compositions are unmixed which shows that the crystal structure is face centered cubic (FCC).

The XRD patterns show also a slight shifting in peaks position towards higher d-spacing values with increasing Cr^{3+} composition in the Co-Mn ferrites. The d-spacings for the recorded peaks were calculated according to Bragg's law. The values of lattice parameter (a) were obtained by fitting the diffracted peaks using standard least-squares method and by employing eq. 5.1 against Cr^{3+} ion substitution are shown in Fig. 5.2. It can be observed from the figure that the unit cell parameter decrease with an increasing Cr^{3+} substitution. In Cr^{3+} substituted Co-Mn ferrites, the Cr^{3+} ions are known to have strong site preference of B sites [49] leads to the replacement of Mn^{3+} ions at octahedral sites. The variation of lattice constant with increasing Cr^{3+}substitution can be explained on the basis of ionic radii of the impurity ions. The pauling ionic radius of Cr^{3+} (0.63Å) is smaller than that of Mn^{3+} (0.66 Å) ions. If the radius of the impurity ion is smaller than the displaced ion, the lattice shrinks and the lattice constant decreases.

It can be seen from Table 5.2 and Fig. 5.3that X-ray density increases with increase Cr^{3+} concentration, while the lattice parameter (a) has the opposite behavior. This causes a decrease in the size of the unit cell and consequently, it causes an increase of the X-ray density. Secondly the variation may be related to the difference in the atomic weights between Cr^{3+} and Mn^{3+} ions.

Table 5.2 and Fig.5.4 shows the compositional variation of bulk density (d_B) of Cr^{3+} substituted Co-Mn ferrite sintered at 600 °C for 4 h.It is indicated that the density noticeably decreases with the increase of Cr^{3+} substitution x until x = 0.75, for x = 1.0 composition a slight stability was observed for this sample. The decreasing of bulk density against Cr^{3+} substitution for the all the samples can be ascribed to the atomic weight and density of Cr (51.99,7.19 gm-3), which are smaller than that of Mn (54.93, 7.23 gm^{-3}). Secondly, the decrease might also be caused by many generated intragrain pores.

One of the most often used approaches in estimating the crystallite size (D_{XRD}) from the XRD data is the utilization of the Scherrer formula (eq.5.3) [45]. The peaks of (2 2 0), (3 1 1), (2 2 2), (4 0 0), (4 2 2), (333) and (4 4 0) have been de convoluted to Lorentzian curves for the determination of the crystallite size using full-width at half maximum value. It is observed from Table 5.2and Fig. 5.5 that the D_{XRD} decreased from 19.8 (x = 0.0) to 14.1 nm for x = 0.5 and it again increased to 16.3 nm for x = 1.0. It can be concluded that the replacement of Mn^{3+}ions with Cr^{3+} in Co–Mn ferrite may leads to a decrease in cation vacancies and in turn to a decrease of crystallite size.

Yan and Johnson [50] concluded that, the dissolution of an oxide dopant with 2^+ cation valence in ferrite does not created excess cation vacancies. However, dopants with 3^+ cation valence generate little excess cation vacancy concentration in the ferrite lattice. They also attributed the absence of enhanced grain growth for dopant oxides with 2^+ or 3^+ cation valence to the lake of a significant number of excess cation vacancies in the ferrite lattice.

It is also possible that the excess Mn_2O_3 in the ferrite composition may results in a higher cation vacancy concentration and lower density. The low cation vacancies can reduce the flux of cation diffusion and hence pore migration will be retarded. As a consequence, it was observed that pores were trapped inside the grains [51]. Therefore, the Cr^{3+} substitution which is accompanied by a decrease in Mn_2O_3 content in the Co-Mn ferrite results in a decrease in cation vacancies. The decrease in cation vacancies with increasing Cr^{3+}substitution in the prepared nano particle samples may be the reason for the observed decrease in crystallite size. On the other hand Cr^{3+} ions, which tend to decrease the grain size, cause impedance to the domain wall motion in ferrite and that the higher the concentration of these ions the more the wall motion is impeded [52].

The effect of Cr^{3+} substitution on the porosity of the prepared samples are observed in Table 5.2 and Fig. 5.6 The Cr^{3+} substitution enhance the porosity thus decreasing the density of the sample. Since the decrease of bulk density is of order 0.014 g/cm^3 with Cr substitution while the increase of X-ray density for x=0.0 to x=0.75 is of order 0.022g/cm^3, one can expect the porosity to increase with increasing Cr substitution. The small difference between d_B and d_X is mainly due to the increase in porosity percentage.

It has been reported that the jump length 'L_A and L_B'(i.e. the distance between the magnetic ions) of electrons influences the physical properties of the ferrite system. Electrons those are hopping between B- and A- sites are less probable compared to that between B- and B-sites, because the distance between the two metal ions placed in B-sites is smaller than if they were placed one in B-sites and the other in A-sites. *'L'* of the A- and B-sites is determined from the relations 5.5 and 5.6. It is observed from Table 5.3 and Fig. 5.7 that 'L_A and L_B' decreases with increasing Cr^{3+} substitution. The decrease in jump length is due to the decrease in the distance between the magnetic ions by the substitution of smaller Cr^{3+} ions at the B-sites.

Transmission electron microscopy

In order to investigate the particle morphology and confirm the phase structure of the sol-gel synthesized Co-Mn ferrite nano particle samples, selected samples were examined by high magnification TEM.TEM results are also helpful in order to clarify the nanostructure of ferrite magnetic nano particles prepared by sol-gel method. It is observed from Figs. 5.8(a) and 5.9(a) that the magnetic nano particles are aggregated. The average value of the nano crystalline particles are is consistent with the result obtained from XRD analysis. It is evident that the magnetic nano particles are not in exactly in spherical shape. With the observation of ferrite nano particles it reflects the shape of the spinel crystal of FCC structure. It can also be seen from TEM images that the ferrite nano particles are uniform in both morphology and particle size, but agglomerated to some extend due to the interaction between magnetic nano particles. Figs. 5.8(b)-5.9(b) shows selected area electronic diffraction (SAED) pattern of then particles and indexed diffraction rings confirm the crystal planes of Co-Mn-Al ferrite.

All the allied parameters; tetrahedral and octahedral bond length (d_{Ax} and d_{Bx}), tetrahedral edge, shared and unshared octahedral edge (d_{AXE} and d_{BXE}) were calculated using equations 5.7-5.11. The values of all the allied parameters are tabulated in Table 5.4 and their graphical illustration were presented in Figs. 5.10-5.14. It is observed that d_{Ax}, d_{Bx}, d_{AXE} and d_{BXE} decrease with increasing Cr^{3+} substitution. This is due to the substitution process, that is, replacement of larger ionic radii (Mn^{3+}) by smaller ionic radii (Mn^{3+}) and their distribution over the tetrahedral A- and octahedral B-sites.

5.3.2 Infrared spectroscopy (IR)

Infrared spectroscopy is used to detect completion of solid state reaction, cation distribution, deformation of spinel structure, cation ordering and force constants for octahedral and tetrahedral sites in spinel ferrites. The ferrite crystallizes in the natural spinel ($MgAl_2O_4$) form with the space group $Fd3m - (O_h^7)$. On the basis of group theoretical calculations, spinel ferrites exhibit four IR active fundamentals (ν) in the vibrational spectra of normal as well as inverse spinel ferrites [53]. It has been reported that the first three IR bands are due to tetrahedral (A) and octahedral [B] coordination compounds, while the fourth one is due to some type of lattice vibrations involving tetrahedral cations.

Figs. 5.15 (a-c) shows the IR absorption spectra of all the investigated ferrite samples, from which it can be seen that there are four bands characterizing ferrites which can easily be observed in the range 300–800 cm^{-1} for the studied samples. The positions of IR bands are listed in Table 5.5.The difference in positions of the bands for the various compositions was expected because of the difference in the distances for the octahedral and tetrahedral ions [Waldron], the four bands can be classified into two groups: two high-frequency bands and two low-frequency bands.

The high-frequency bands, ν_1; is appeared in the wave number range of 716–748 cm^{-1} and is related to intrinsic vibrations of the tetrahedral group, the second band, ν_2 is in the range of 294–375 cm^{-1} and is due to the octahedral metal complexes. The shoulder to the band ν_1 is appeared, this should is corresponds to low-frequency ν_3 band which is in the range of 494–551 cm^{-1} and this ν_3 band is probably related to the divalent octahedral metal–oxygen ion complexes. The forth band, ν_4 at 220-307 cm^{-1} was observed and can be assigned to the divalent tetrahedral vibrations.The shift in the ν_1 and ν_2 bands was found to depend on the compositions of ferrites.

Increase in substitution of Cr^{3+} ions increase the intensity of all the bands at the same time increase in broadness is also observed. This increase in intensity and increase in broadness can be explained on the basis of cation distribution.The order of cations on the octahedral site varied as the Cr^{3+} content increased thereby decreasing the Mn^{3+} and Fe^{3+}composition from the octahedral B site. The disorderedsystem gives rise to broader bands in their spectrum [54] and it has been attributed to the statistical distribution of Fe ion son A and B sites.

The variation in the intensity of absorption band may also be related to the change of dipole moment with the internuclear distance ($d\mu/dr$) [55]. This value represents the contribution of the ionic bond Fe–O in the lattice. So, the observed variation in the absorption band intensity with increasing Cr^{3+}substitution is presumably due to the perturbation occurring in Fe–O bonds by substitution the Cr^{3+} ions. On the other hand, the electronic distribution of Fe–O bonds is greatly affected when Cr^{3+} ion with ($3d^4 4S^2$) orbital is introduced in its neighbourhood and this consequently affects ($d\mu/dr$) of the Fe–O bond [56].The absorption band $\nu_1$shifts slightly towards the higher frequency side, which can be attributed to the shifting of Feions towards oxygen ion on occupation of tetrahedral site by Cr^{3+} ions with smaller ionic radii, which decreases the Fe –O distance. The variation in$v_2$band frequency may be associated with the bond length and the change in cation distribution. The observed v_3 band could be due to Co^{2+}-O^- and Fe^{3+}-O^- complexes on the octahedral site. The intensity of this band decreased with the increase in Cr^{3+} ions since the Fe^{3+} composition decreased with increase in Cr^{3+} ions.

5.3.3 Cation distribution

The cation distribution of the presently investigated spinel ferrite system was estimated using X-ray diffraction data. The details of the analysis are already discussed in chapter 4. The estimated cation distribution of Co^{2+}, Mn^{3+}, Fe^{3+} and Cr^{3+} is listed in Table 5.6. It can be observed from the data of cation distribution that the Cr^{3+} ions show a preference for octahedral B-sites. From occupancy variation we have observed that Fe^{3+} ion can occupy both tetrahedral A- and octahedral B-sites. Hence, the present samples are in mixed spinel structure. Partial migration of $Co^{2+}$and Fe^{3+}ions from B to A sites has been observed by increasing the Cr^{3+}substitution accompanied by decreasing number of Mn^{3+} ions from A-sites.

In corroborating Eq. 5.12, the theoretical lattice constant (a_{th}) was calculated for different values of x. Over the range of x it has been noticed that the calculated values of the lattice constant agree rather well with the experimental results as depicted in Fig. 5.16 and Table 5.7.The difference between the theoretical and experimental lattice parameter is evidenced for all the samples as observed in Figs. 5.2 and 5.16. This discrepancy can be attributed to the porosity of the samples which reflect the behavior of the density.

The mean ionic radius of the tetrahedral A- and octahedral B-sites (r_A and r_B) can be calculated for all the samples using the cation distribution data. The values of the r_A and r_B are given in Table 5.7 and their variation is shown in Figs. 5.17 and 5.18. It is observed that the mean ionic radii of octahedral B site (r_B) decreases with an increase in Cr^{3+} substitution. The decrease in r_B is due to the occupancy of smaller Cr^{3+} ions of ionic radii

(0.63 Å). The occupancy of Cr^{3+} ions at B site is eventually associated with an increase in mean ionic radii of tetrahedral A-site. As the Cr^{3+} ion occupy the octahedral site is force Co^{2+} and Fe^{3+} ions of combined larger ionic radii to migrate tetrahedral A-site. This migration of Co^{2+} and Fe^{3+} ions from B site to A site enhance the mean ionic radii of tetrahedral A-site, resulted in an increase in r_B.

Table 5.7 and Fig. 5.19 shows the calculated values of oxygen positional parameter 'u'. The oxygen parameter 'u'depends on the chemical composition, preparation conditions and sintering procedure. The ideal 'u'value is close to 0.375Å in spinel ferrites. The values of 'u' for the investigated samples were higher than the ideal one. This indicates that the crystal lattice deviates from the ideal spinel ferrite because of the difference in the chemical composition. However, the deviation from the ideal crystal structure (Δ) found to vary with Cr^{3+} substitution.

5.3.4 Magnetization

The magnetization curves of the synthesized and annealed $CoMn_{1-x}Cr_xFeO_4$ spinel ferrite nano particle samples obtained from room temperature VSM measurement are shown in Figs. 5.20(a-c).Substitution of Cr^{3+} ions into Co-Mn ferrite greatly affects its magnetic properties. The values of saturation magnetization (Ms), coercivity (Hc), remanence magnetization (Mr), remanence ratio (R) and magneton number (n_B) obtained from magnetization plots are given in Table 5.8.

It is observed from Figs. 5.20 and 5.21 that the substitution of Cr^{3+} ions decreases the saturation magnetization of Co-Mn ferrite. Incorporation of more Cr^{3+} ions into the B sites weakens the L-S couplings further, probably due to the weaker magnetic moment of Cr^{3+} compared to Mn^{3+}. Such results suggest that the L-S couplings in Cr^{3+} do not benefit from its relatively large orbital angular momentum. On the other hand, Co^{2+} with a $t_{2g}^5e_g^2$electron configuration in spinel has very strong L-S coupling even though it has the same number of unpaired electrons and the same theoretical orbital angular momentum as the

Cr^{3+}cation. The great difference in magnetic behavior between $Co^{2+}$and Cr^{3+} cations in spinel ferrite nano particles may offer some insights into the magnetic quantum interactions at the atomic level.

In spinel ferrite the saturation magnetization is dominated by the super exchange interactions between the tetrahedral A- and octahedral B-sites cations. Incorporation of Cr^{3+} ions will decrease the number of magnetic linkages occurring between tetrahedral and octahedral cations and thereby leads to weakening of the tetrahedral–octahedral super exchange interactions. According to Neel's molecular-field model [48], the A-B super exchange interaction predominate the intra sublattice A-A and B-B interactions. Therefore, the net magnetic moment is given by the sum of the magnetic moments of the A and B sub lattices; $n_{Bcal.}= M_B-M_A$, where M_B and M_A are the B and A sub-lattice magnetic moments in μ_B, n_{Bcal}.Values of $n_{Bcal.}$were calculated using cation distribution data and by using the magnetic moment of Fe^{3+} ($5\mu_B$), Co^{2+}($2\mu_B$), Mn^{3+}($4\mu_B$) and Cr^{3+}($3\mu_B$) ions.

The observed magnetic moment ($n_{B\ Obs.}$) per formula unit in the Bohr magnet on (μ_B) was calculated using the relation 5.14.The variation of both the magnet on number is shown in Fig. 5.22 and the values are presented in Table 5.8. In the present ferrite system the Fe^{3+} ions are replaced by Cr^{3+} ions, leading to a decrease in the B -site sublattice magnetization. Therefore, the magnetization of the B sublattices decreases, which leads to a decrease in the net magnetization. The decrease in net magnetic moment can be explained by the A-B interaction. In the presently investigated system, Cr^{3+}($3\mu_B$) ions replacesMn^{3+}($4\mu_B$) ions. This replacement leads to a decrease of the magnetic moment of the B -site, and thus the magnet on number n_B decreases with Cr^{3+}substitution. The decrease in $n_{B\ Obs.}$ is associated mainly due to the decrease in saturation magnetization and molecular weight with Cr^{3+} substitution.

Remanence magnetization (Mr) and remanence ratio (R) is also decreased (Figs. 5.23-5.24 and Table 5.8) with the increase in Cr^{3+} substitution. Coercive field reflect the coercivity of a ferromagnetic or ferrimagnetic material. This value refers to the intensity of the magnetic field required to reduce the magnetization of the magnetic sample to zero after the magnetization of the sample has reached saturation. It is observed from Fig. 5.25 and Table 5.8 that the coercivity increases with increasing Cr^{3+} substitution. According to the one-ion model, the anisotropy field of ferrites depends on the amount of Fe ions in the sample. It observed that the distribution of Co^{2+} and Fe^{3+} ions varies as a result of increasing Cr^{3+}substitution. This might positively contribute for anisotropy constant to increase with increasing Cr^{3+}substitution and that, consequently, the magnitude of Hc also increases. According to Stoner-Wolfforth theory coercivity is related to anisotropy constant K though the following relation [57,58]:

$$H_C = \frac{0.98 \times K}{M_S} \qquad 5.15$$

Where

K is the anisotropy constant and Ms is the saturation magnetization.

For all concentrations of Cr^{3+} ions, the system may be considered isolated. According to this relation Ms is inversely proportional to Hc, and this is in good agreement with the present magnetic results.The coercivity also depends upon defects, surface effect, strains, non-magnetic atoms, etc. in thematerial [59]. The coercive force variation of the system shows atypical size dependent behavior. This behavior can be attributed to the combination of surface effect and its surface anisotropy [60]. The electronic configuration of Cr^{3+} ions results in the lattice or crystalline field distortion, and generates an internal stress. This might also one of the reasons to increase the coercivity of the samples with Cr^{3+} substitution

5.4 Conclusions

The nano particles of Cr^{3+} substituted Co-Mn ferrite with particle size 14-19 nm have been successfully synthesized by sol-gel auto-combustion method. No impurity phase other than cubic spinel is observed in the X-ray diffraction data. The XRD pattern revealed that the cubic spinel structure is maintained for the all the compositions. The particle sizes measured from XRD and TEM are in good agreement with each other. The estimated cation distribution data obtained from the XRD analysis with employing Bertaut method indicate that Co^{2+}, Cr^{3+} and Fe^{3+} have strong preference towards octahedral B-site whereas Mn^{3+} preferred octahedral B site. The theoretical values of lattice constant agree well with experimental lattice constant, and show decreasing trend with increase in Cr^{3+} substitution. The structural parameters such as X-ray density, bulk density, and porosity were strongly affected by the incorporation of Cr^{3+} ions in Co-Mn ferrite. Hopping length i.e. jump length of ion decreased with Cr^{3+}substitution and can be related to the smaller ionic radii associated with Cr^{3+} ions as compared to that Mn^{3+} ions. Two major absorption bands were observed in the infrared spectra and reveal the formation of single phase cubic spinel structure of Cr^{3+} substituted Co-Mn ferrite. The saturation magnetization, remanence magnetization and remanence ratio decreases linearly with increasing Cr^{3+} content. Incorporation of more Cr^{3+} ions into the B sites weakens the L-S couplings further, probably due to the weaker magnetic moment of Cr^{3+} compared to Mn^{3+}. Such results suggest that the L-S couplings in Cr^{3+} do not benefit from its relatively large or bitalangular momentum. Coercivity found to enhance with Cr^{3+}substitution.

References

[1] Z. Siwy, I.D. Kosinska, A. Fulinski, C.R. Martin, Phys. Rev. Lett. 94 (2005) 048102.

[2] J.H. Shim, T. Hwang, S. Lee, J.H. Park, S.J. Han, Y.H. Jeong, Appl. Phys. Lett. 86(2005) 082503.

[3] A.E. Strevens, A. Drury, S.M. Lipson, M. Kroll,W.J. Blau, H.H. Horhold, Appl. Phys.Lett. 86 (2005) 143503.

[4] X. Yang, J. Dong, Appl. Phys. Lett. 86 (2005) 163105.

[5] M. Endo, H. Muramatsu, T. Hayashi, Y.A. Kim, M. Terrones, M.S. Dresselhaus,Nature 433 (2005) 476.

[6] H. Cui, X. Yang, L.R. Baylor, D.H. Lowndes, Appl. Phys. Lett. 86 (2005) 053110.

[7] S. Morup, C. Frandsen, Phys. Rev. Lett. 92 (2004) 217201.

[8] O. Ozatay, P. Chalsani, N.C. Emloy, I.N. Krivorotov, R.A. Buhrman, J. Appl. Phys.95 (2004) 7315.

[9] F. Meier, V. Cerletti, O. Gywat, D. Loss, D.D. Awschalom, Phys. Rev. B 69 (2004)195315.

[10] E. Roduner, Chem. Soc. Rev. 35 (2006) 583.

[11] Man Han, Christy R. Vestal, and Z. John Zhang, J. Phys. Chem. B 108 (2004)583-587

[12] J.L. Dorman, D. Fiorani (Eds.), Magnetic Properties of Fine Particles, North-Holland, Amsterdam, 1992.

[13] M. Kishimoto, Y. Sakurai, T. Ajima, J. Appl. Phys. 76 (1994) 7506.

[14] I.M.L. Billas, A. Chatelain,W.A. de Heer, Science 265 (1994) 1682.

[15] D.D. Awschalom, D.P.D. Vincenzo, Phys. Today (1995) 43.

[16] J. Shi, S. Gider, K. Babcock, D.D. Awschalom, Science 271 (1996) 937.

[17] Manish Srivastava, S. Chaubey, Animesh K. Ojha, Mater. Chem. Phys. 118 (2009) 174–180

[18] Alex Goldman, Modern Ferrite Technology, 2nd ed. Springer, New York, 2006.

[19] M. Kaiser, J. Alloys Compd. 468 (2009) 15–21

[20] P.K. Roy, J. Bera, J. Mater. Res. Bull. 42 (2007) 77.

[21] Sagar E. Shirsath, R. H. Kadam, S. M. Patange, M. L. Mane, Ali Ghasemi, Akimitsu Morisako, Appl. Phys. Lett. 100 (2012) 042407.

[22] V. Varshuey, R.K. Puri, IEEE Trans. Magn. 25 (1989) 3109.

[23] V. N.Antonov, B. N.Harmon, V. P.Antropov, A. Y. Perlov,A. N. Yresko, Phys. Rev. B 64 (2001) 134410.

[24] G. A.Sawatzky, F.Van Der Woude,A. H. Morrish, Phys. Rev. 187 (1969) 747.

[25] Einat Tirosh, Gabriel Shemer, and Gil Markovich, Chem. Mater.18 (2006)465-470

[26] Sagar E Shirsath, “Synthesis condition reflected structural and magnetic properties of $Li_{05}Cr_{05}Fe_2O_4$ nanoparticles” in ‘Magnetic Nanoparticles: Properties, Synthesis and Applications’ edited by Beate Acklin and Edon Lautens, Nova publishers, New York,2012.

[27] Sagar E. Shirsath, Yukiko Yasukawa, Ali Ghasemi, Xiaoxi Liu, and Akimitsu Morisako, J. Appl. Phys. 115 (2014) 17A515

[29] H.Mohan,I. A. Shaikh,R. G. Kulharni, Physica B 217 (1996)292.

[30] G. F. Goya, H. R.Rechenberg,J. Z.Jiang, J. Appl. Phys. 84 (1998) 1101.

[28] A.Broese Van Groenou, P. F.Bergers, A. L.Stuyts, Mater. Sci.Eng. 3 (1968/69) 317.

[31] Y. Kinemuchi, K. Ishizaka, H. Suematsu,W. Jiang, K. Yatsui, Thin Solid Films 407(2002) 109.

[32] J. Zhou, J. Ma, C. Sun, L. Xie, Z. Zhao, H. Tian, J. Am. Ceram. Soc. 88 (2005) 3535.

[33] P.E. Meskin, V.K. Ivanov, A.E. Barantchikov, B.R. Churagulov, Y.D. Tretyakov,Ultrason. Sonochem. 13 (2006) 4.

[34] Sagar E. Shirsath, Mahesh L. Mane, Ali Ghasemi, Yukiko Yasukawa, Xiaoxi Liu, Akimitsu Morisako, IEEE Trans. Magn. 49 (2013)4210 - 4213.

[35] J. Liu, H. He, X. Jin, Z. Hao, Z. Hu, Mater. Res. Bull. 36 (2001) 2357.

[36] A. Kale, S. Gubbala, R.D.K. Misra, J. Magn. Magn. Mater. 277 (2004)

350.

[37] S.Komarneni, E. Fregeau, E. Breval, R. Roy, J. Am. Ceram. Soc.Commun.71 (1988),C–26.

[38] A.H. Morrish, K. Haneda, J. Appl. Phys 52 (1981) 2496.

[39] D.W. Johnson Jr., Am. Ceram. Soc. Bull. 60 (1981) 221.

[40] A. M. Pachpinde, M. M. Langade, Kishan S. Lohar, Sunil M. Patange, Sagar E. Shirsath, Chem. Phys. 429 (2013) 20-26

[41] Ph. Courty, H. Ajot, Ch. Macilly, B. Delmon, Powder Technol. 7 (1973) 21.

[42] A.S. Teja, P.Y. Koh, Prog. Cryst. Growth Charact. Mater. 55 (2009) 22.

[43] U.T. Lam, R. Mammucari, K. Suzuki, N.R. Foster, Ind. Eng. Chem. Res. 47 (3) (2008)599.

[44] Sagar E. Shirsath, M. L. Mane, Yukiko Yasukawa, Xiaoxi Liu and Akimitsu Morisako, J. Nano. Res. 15 (2013) 1976

[45] B. D. Cullity, Elements of X-ray diffraction, Addison-Wesley, London, 1959.

[46] R.Valenzuela, Magnetic ceramics, Cambridge University Press, 1994.

[47] K.J. Standley, Oxide magnetic materials, (Clarendon Press, Oxford, 1972).

[48] L. Néel, Ann. Phys. Paris, 3 (1948) 137.

[49] M. V. Chaudhari, Sagar E. Shirsath, A. B. Kadam, R. H. Kadam, S. B. Shelke, D. R. Mane, J. Alloys Compd. 552 (2013) 443–450

[50] M.F. Yan, D.W. Johnson, J. Am. Ceram. Soc. 61 (1978) 342–349.

[51] P. Sainamthip, V.R.W. Amarakoon, J.Am. Ceram. Soc. 71 (1988) 644–648.

[52] A.M. Sankpal, S.V. Kakatkar, N.D. Chaudhari, R.S. Patil,S.R. Sawant, J. Mater. Sci.: Materials in Electronics 9(1998) 173–179.

[53] R.D. Waldron, Phys. Rev. 99 (1955) 1727.

[54] S.A.Patil, S.M.Otari, V.C.Mahajan, A.B.Patil et al. Solid StateCommun.78(1) (1991) 39.

[55] S.A. Mazen, M.H. Abdallah, B.A. Sabrah, H.A.M. Hashem, Phys.Stat. Sol. (a) 134 (1992) 263–271.

[56] A.M. El-Sayed, Ceram. Inter. 28 (2002) 651–655.

[57] E.C. Stoner and E.P. Wohlfarth, Phil. Trans. Roy. Soc. A 240 (1948)599; Reprinted by IEEE Trans. Magn. 27 (1991)3475.

[58] S. H. Liou, S. Huang, E. Klimek, and R. D. Kirby, J. Appl. Phys. 85, 4334 (1999)

[59] P.K. Roy, J. Bera, J. Magn. Magn. Mater. 320 (2008) 1128.

[60] Sagar E. Shirsath, R. H. Kadam, Anil S. Gaikwad, Ali Ghasemi, Akimitsu Morisako, J. Magn. Magn. Mater.323 (2011) 3104–3108.

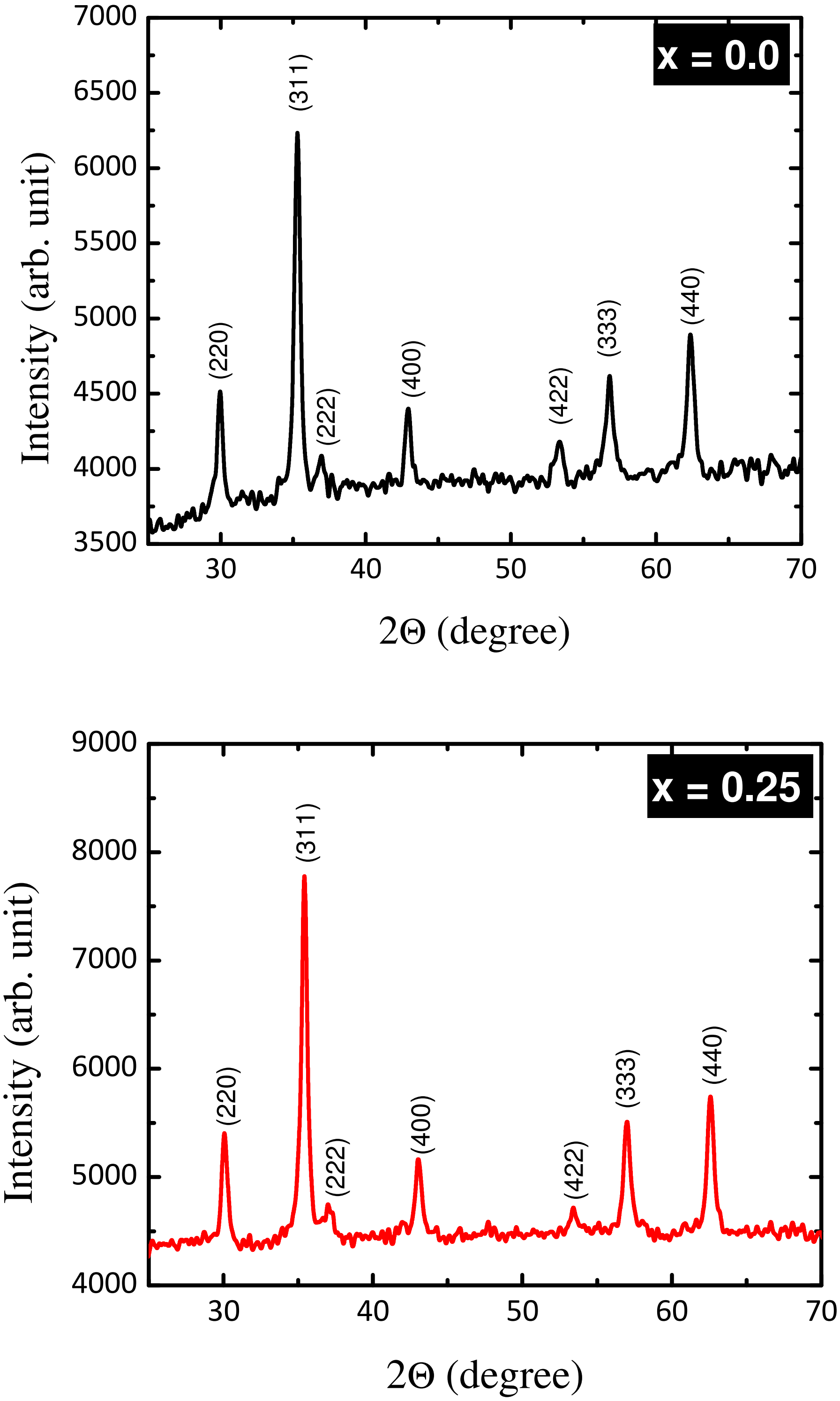

Fig. 5.1 (a): X-Ray diffraction patterns of x = 0.0 and x = 0.025 for $CoMn_{1-x}Cr_xFeO_4$

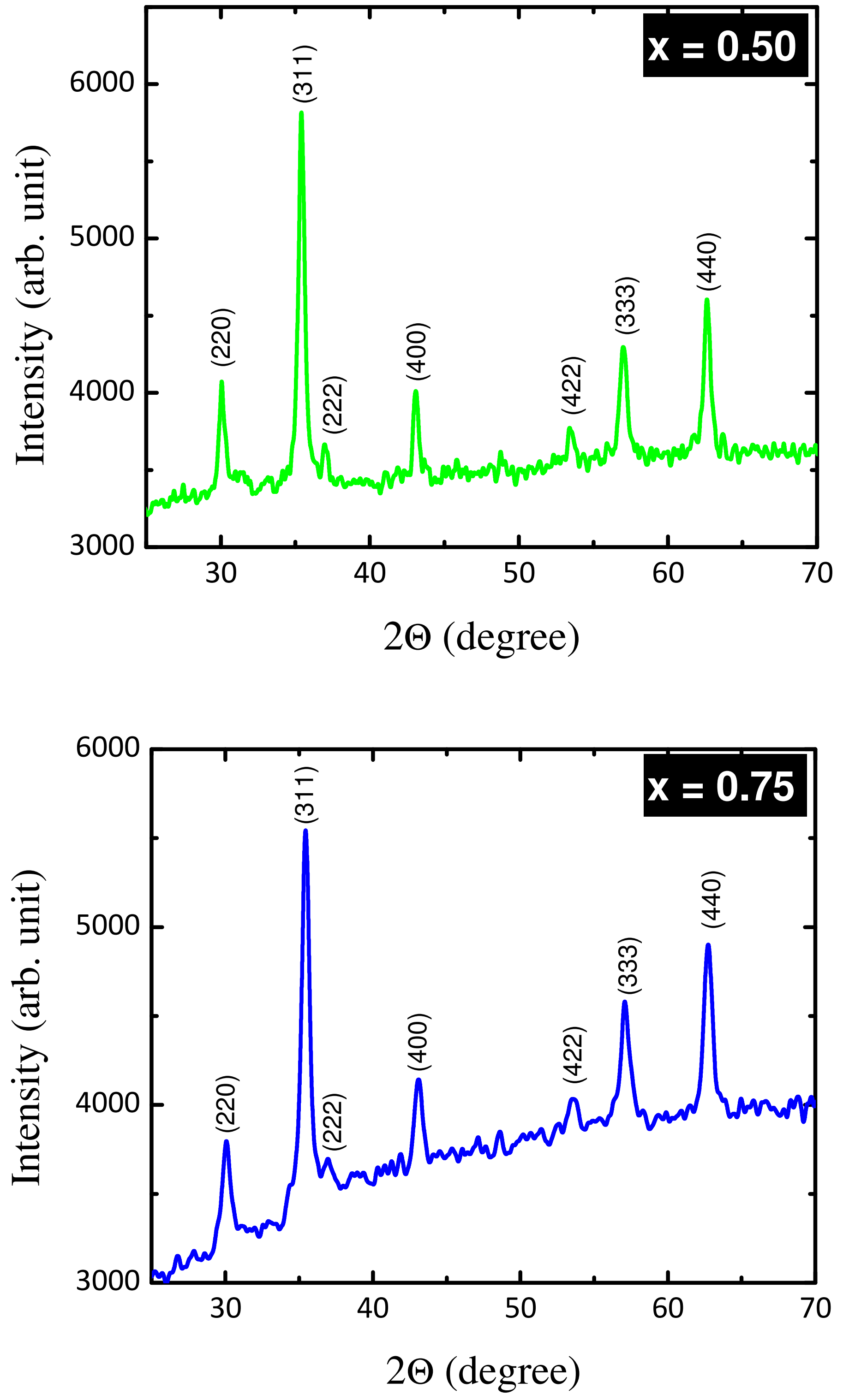

Fig. 5.1 (b): X-Ray diffraction patterns of x = 0.50 and x = 0.075 for CoMn$_{1-x}$Cr$_x$FeO$_4$

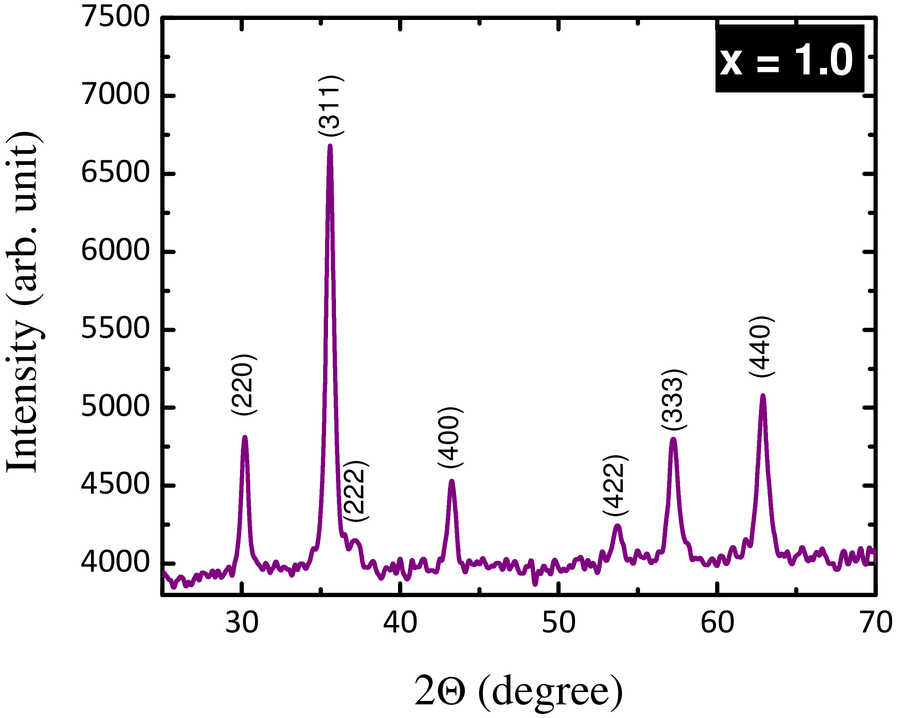

Fig. 5.1 (c): X-Ray diffraction patterns of x = 1.00 for $CoMn_{1-x}Cr_xFeO_4$

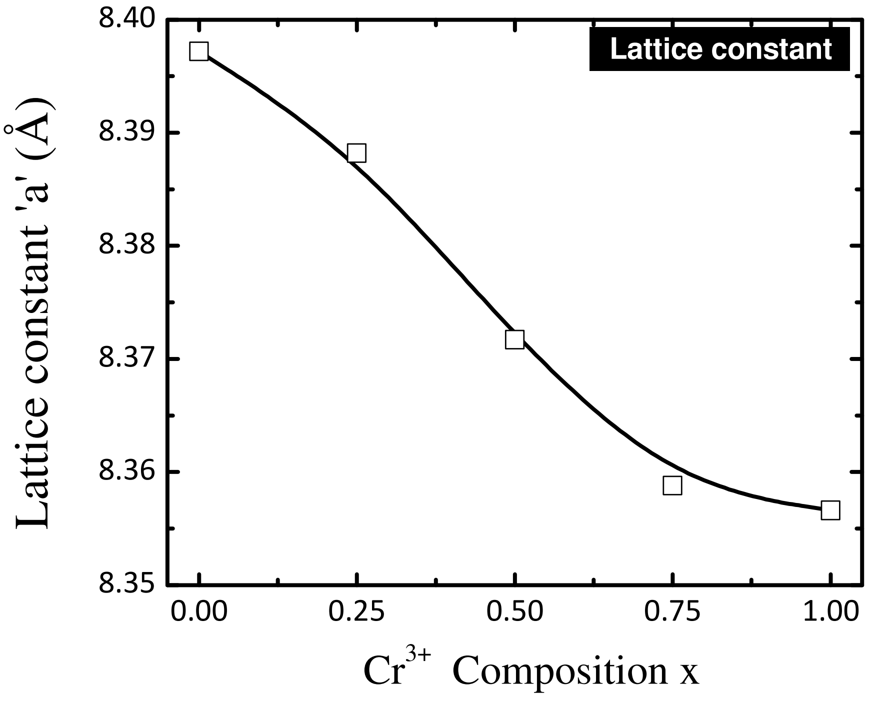

Fig. 5.2: Variation of lattice constant with Cr^{3+} composition x for $CoMn_{1-x}Cr_xFeO_4$.

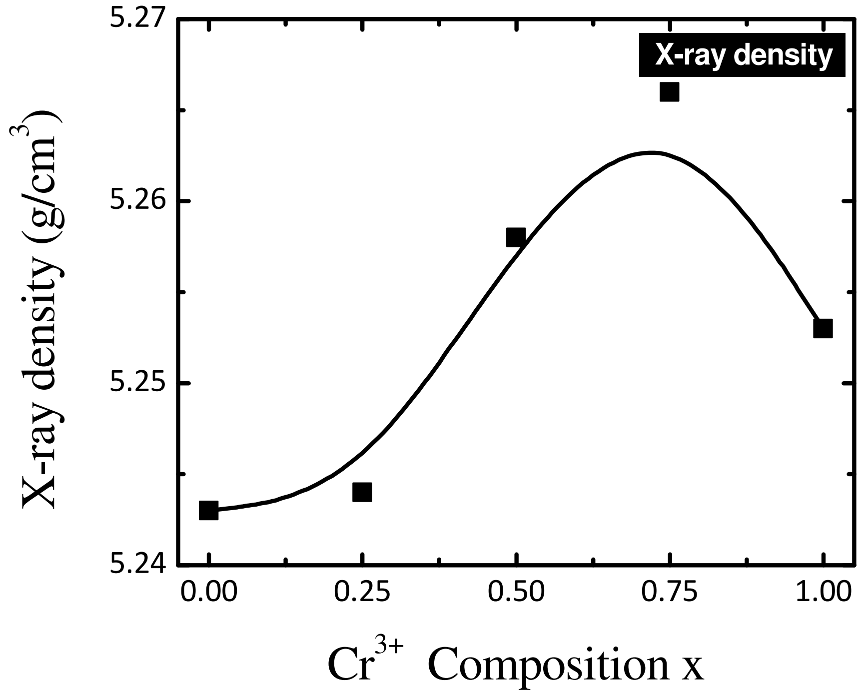

Fig. 5.3: Variation of X-ray density Cr^{3+} composition x for $CoMn_{1-x}Cr_xFeO_4$.

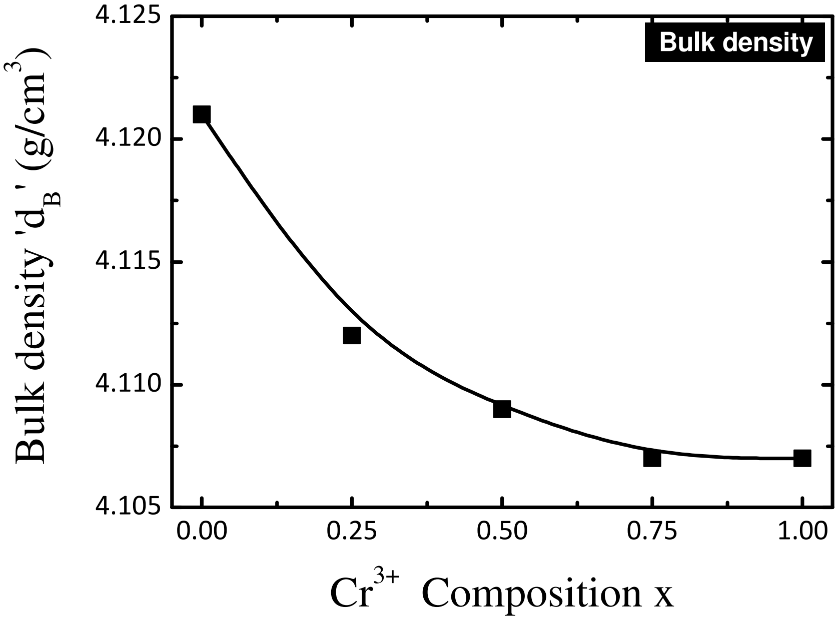

Fig. 5.4: Variation of bulk density (d_B) with Cr^{3+} composition x for $CoMn_{1-x}Cr_xFeO_4$.

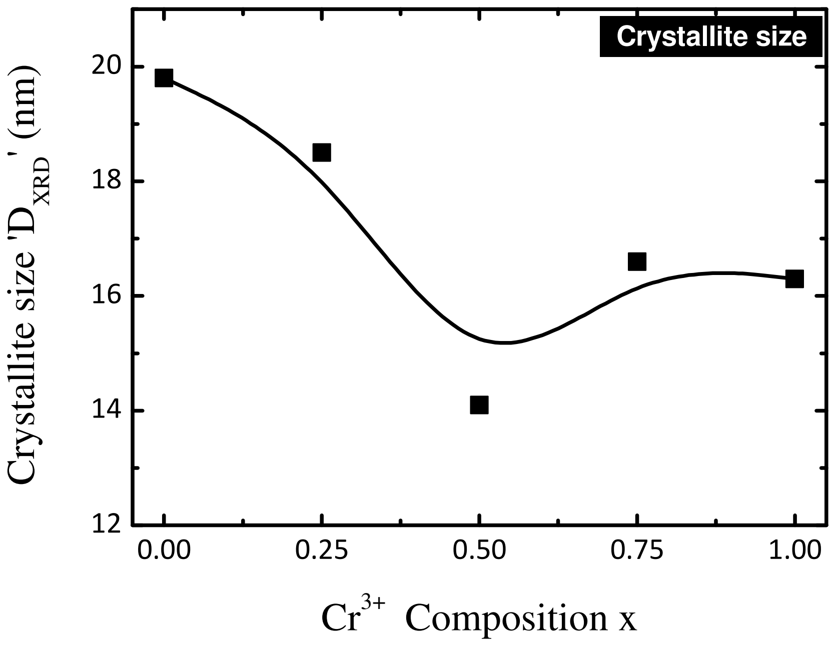

Fig. 5.5: Variation of crystallite size (D_{xrd}) with Cr^{3+} composition x for $CoMn_{1-x}Cr_xFeO_4$.

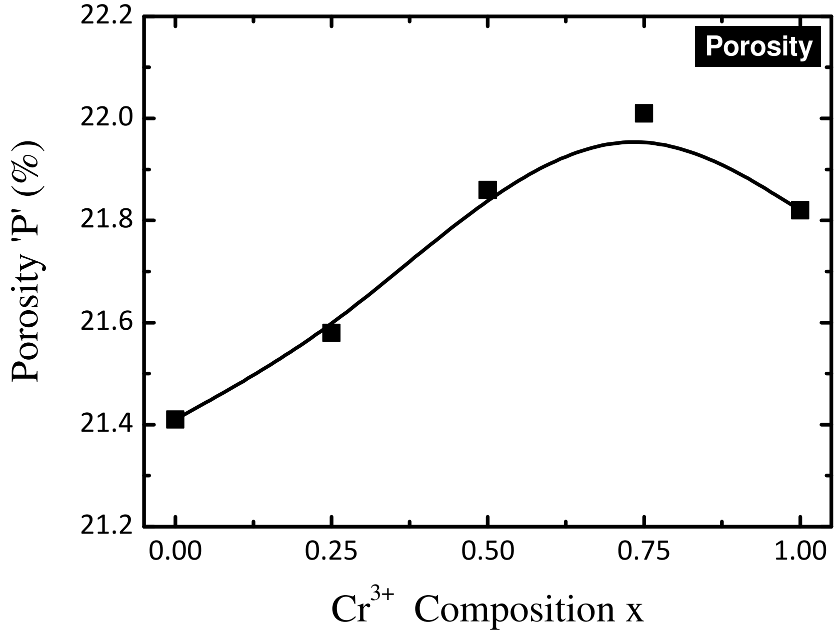

Fig. 5.6: Variation of porosity (P) with Cr^{3+} composition x for $CoMn_{1-x}Cr_xFeO_4$.

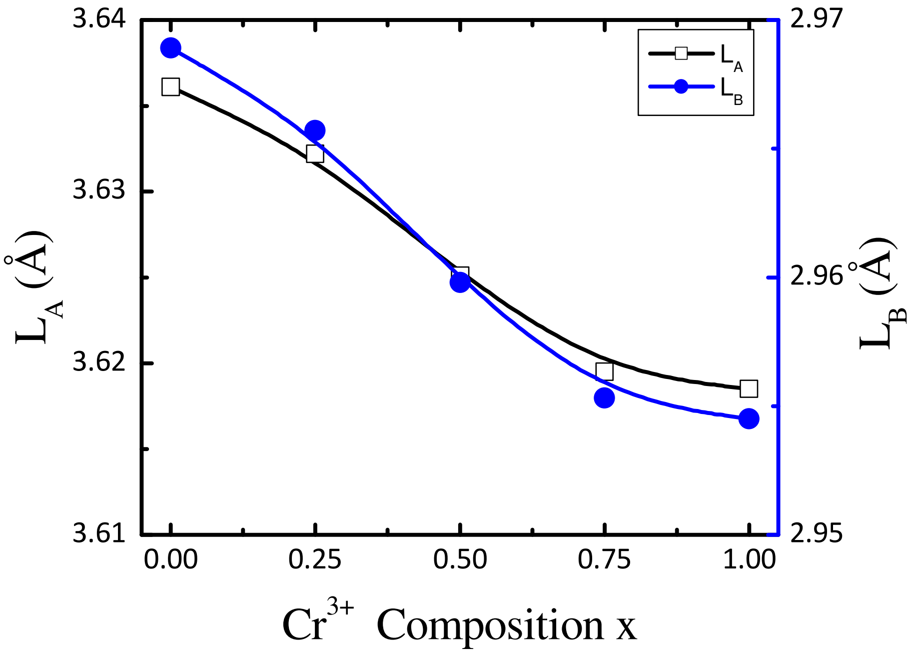

Fig. 5.7: Variation of hopping lengths (L_A and L_B) with Cr^{3+} composition x for $CoMn_{1-x}Cr_xFeO_4$.

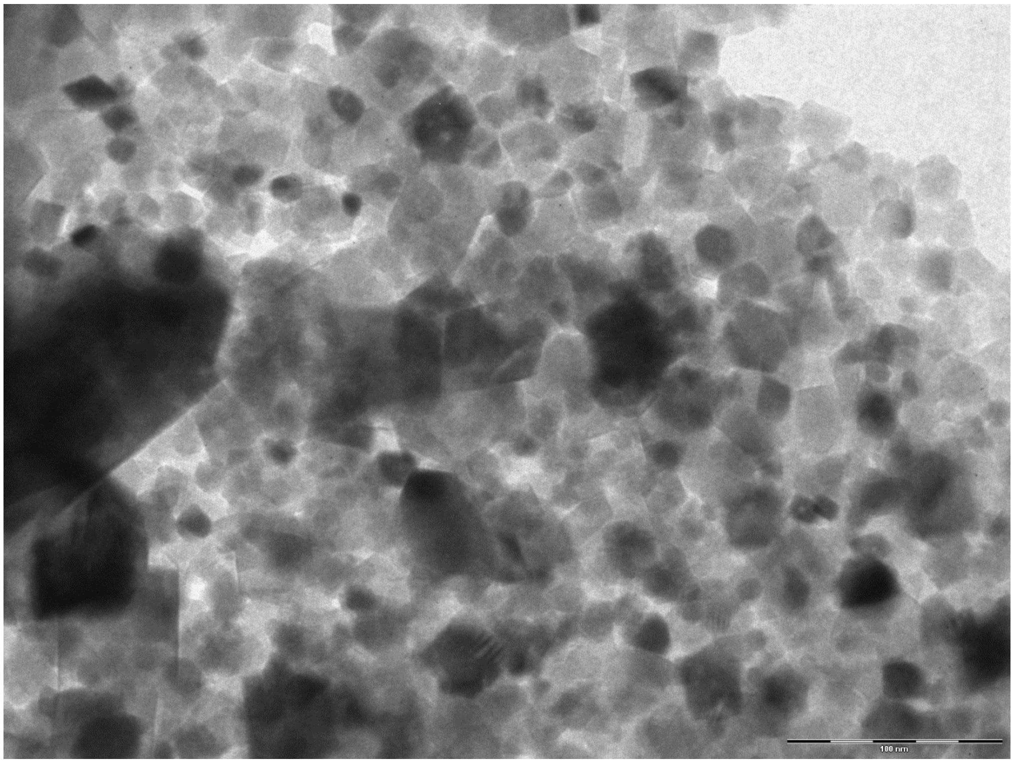

Fig. 5.8 (a). Transmission electron micrograph (TEM) image of x = 0.25 for $CoMn_{1-x}Cr_xFeO_4$

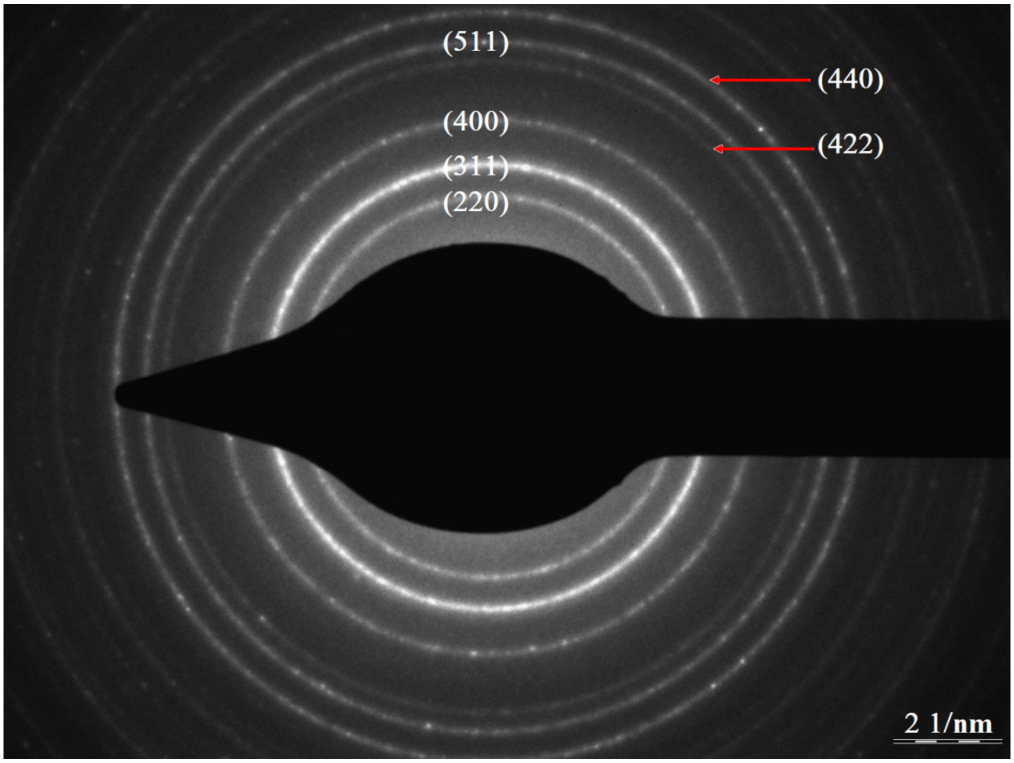

Fig. 5.8 (b). Selected area electron diffraction (SAED) image of x = 0.25 for $CoMn_{1-x}Cr_xFeO_4$

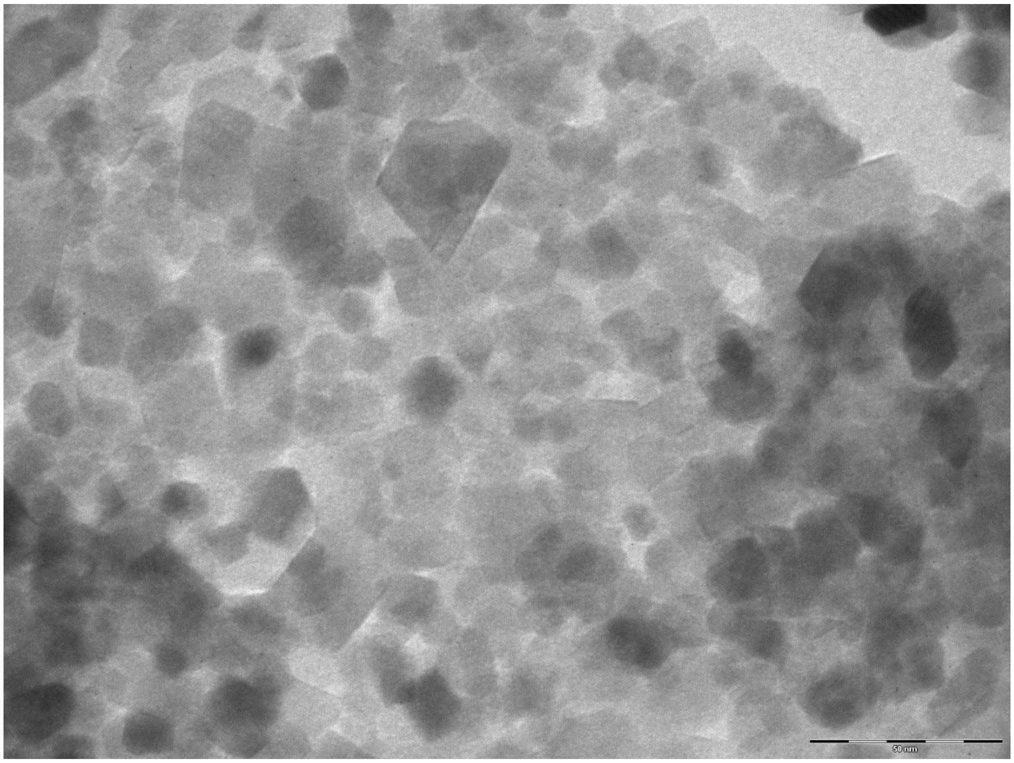

Fig. 5.9 (a). Transmission electron micrograph (TEM) image of x = 1.0 for $CoMn_{1-x}Cr_xFeO_4$

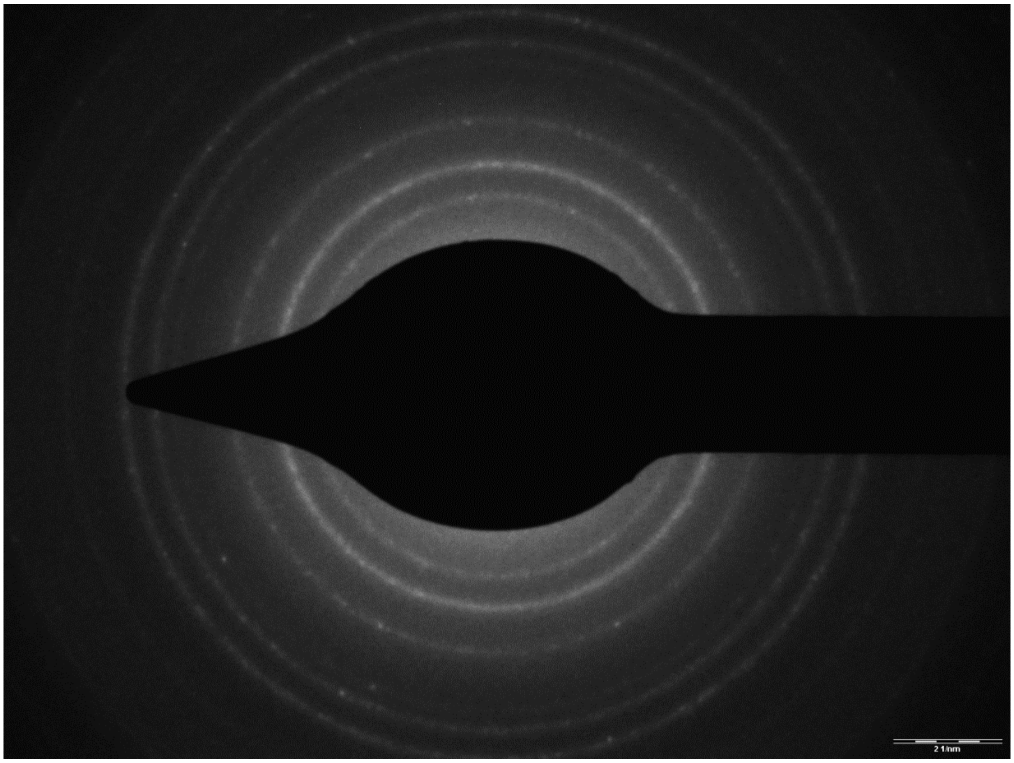

Fig. 5.9 (b). Selected area electron diffraction (SAED) image of x = 1.0 for $CoMn_{1-x}Cr_xFeO_4$

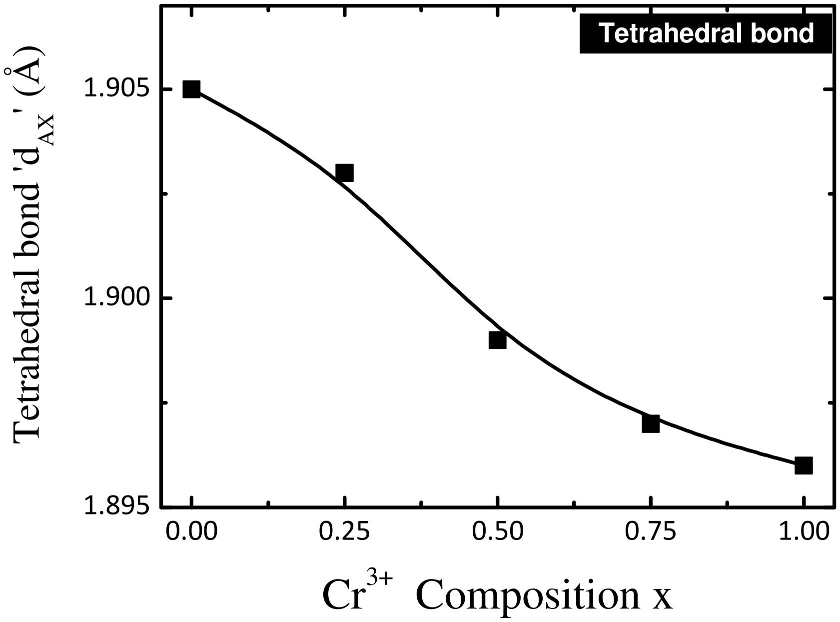

Fig. 5.10: Variation of Tetrahedral bond (d_{AX}) with Cr^{3+} composition x for $CoMn_{1-x}Cr_xFeO_4$.

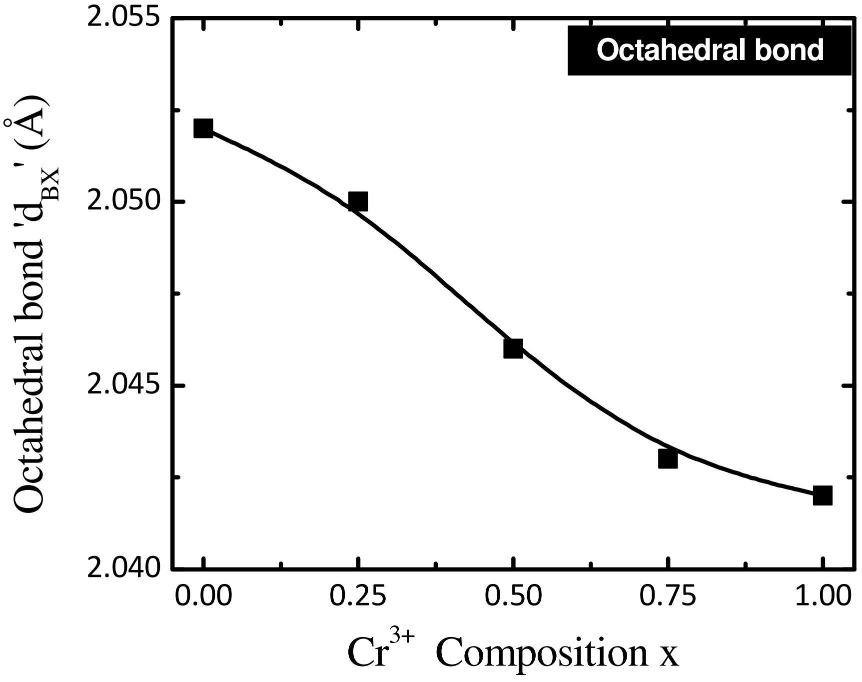

Fig. 5.11: Variation of octahedral bond (d_{BX}) with Cr^{3+} composition x for $CoMn_{1-x}Cr_xFeO_4$.

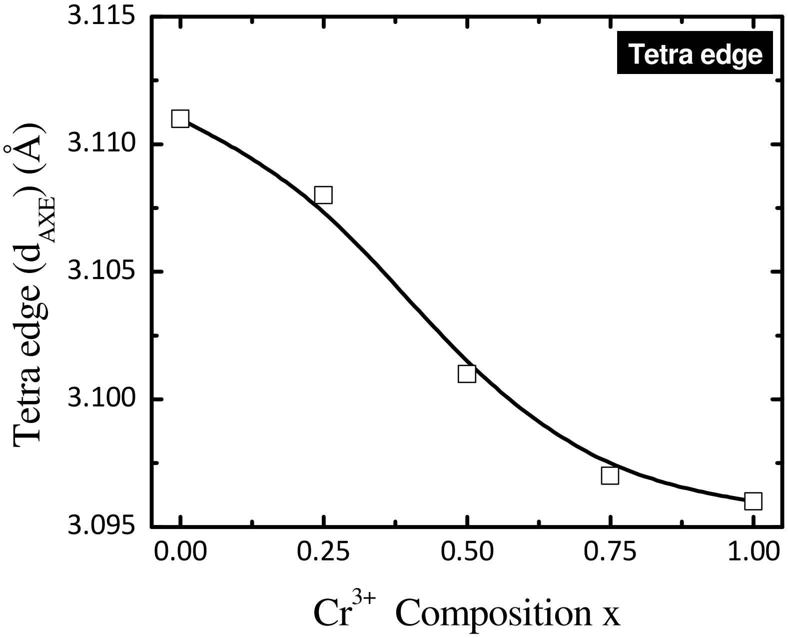

Fig. 5.12: Variation of tetra edge (d_{AXE}) with Cr^{3+} composition x for $CoMn_{1-x}Cr_xFeO_4$.

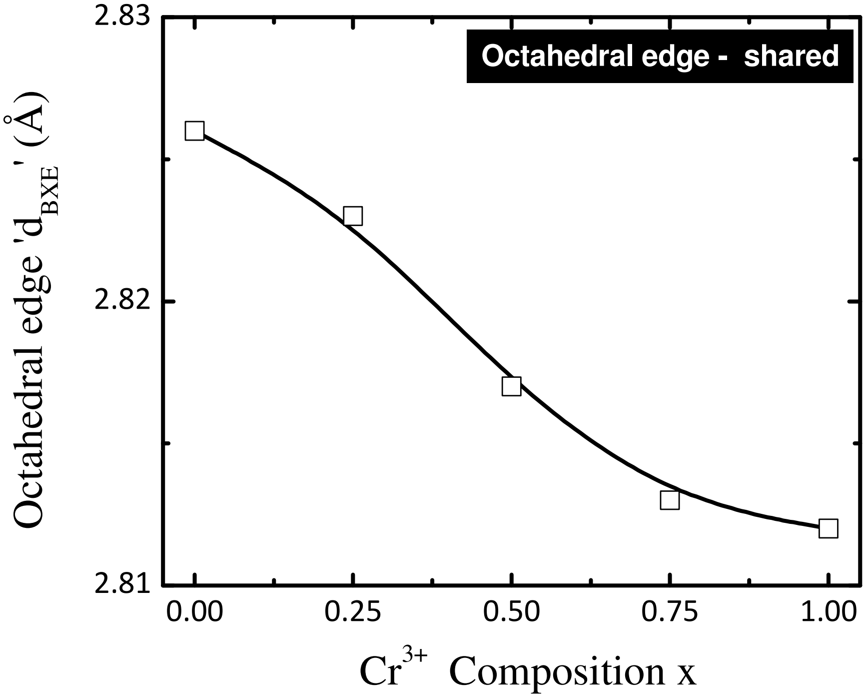

Fig. 5.13: Variation of octahedral edge- *shared* (d_{BXE}) with Cr^{3+} composition x for $CoMn_{1-x}Cr_xFeO_4$.

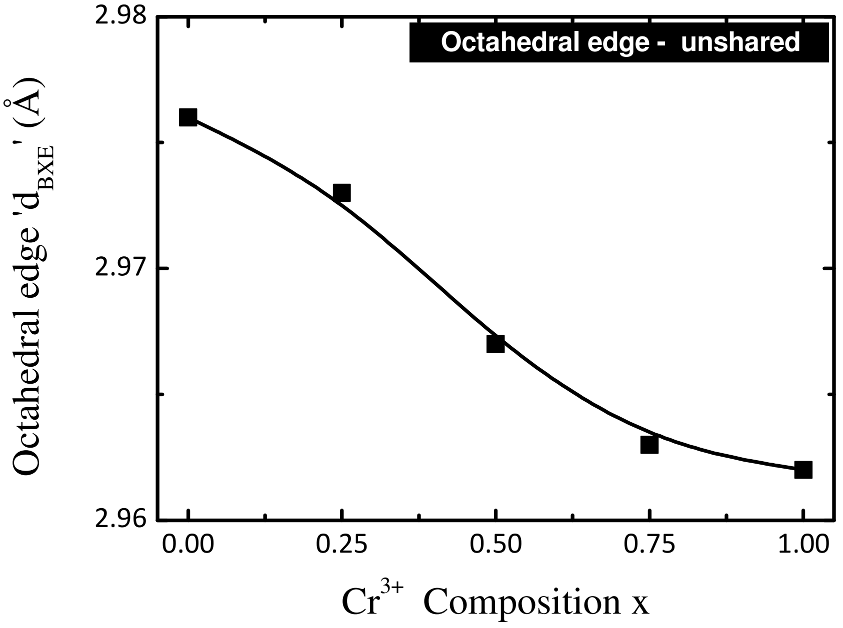

Fig. 5.14: Variation of octahedral edge- *unshared* (d_{BXE}) with Cr^{3+} composition x for $CoMn_{1-x}Cr_xFeO_4$.

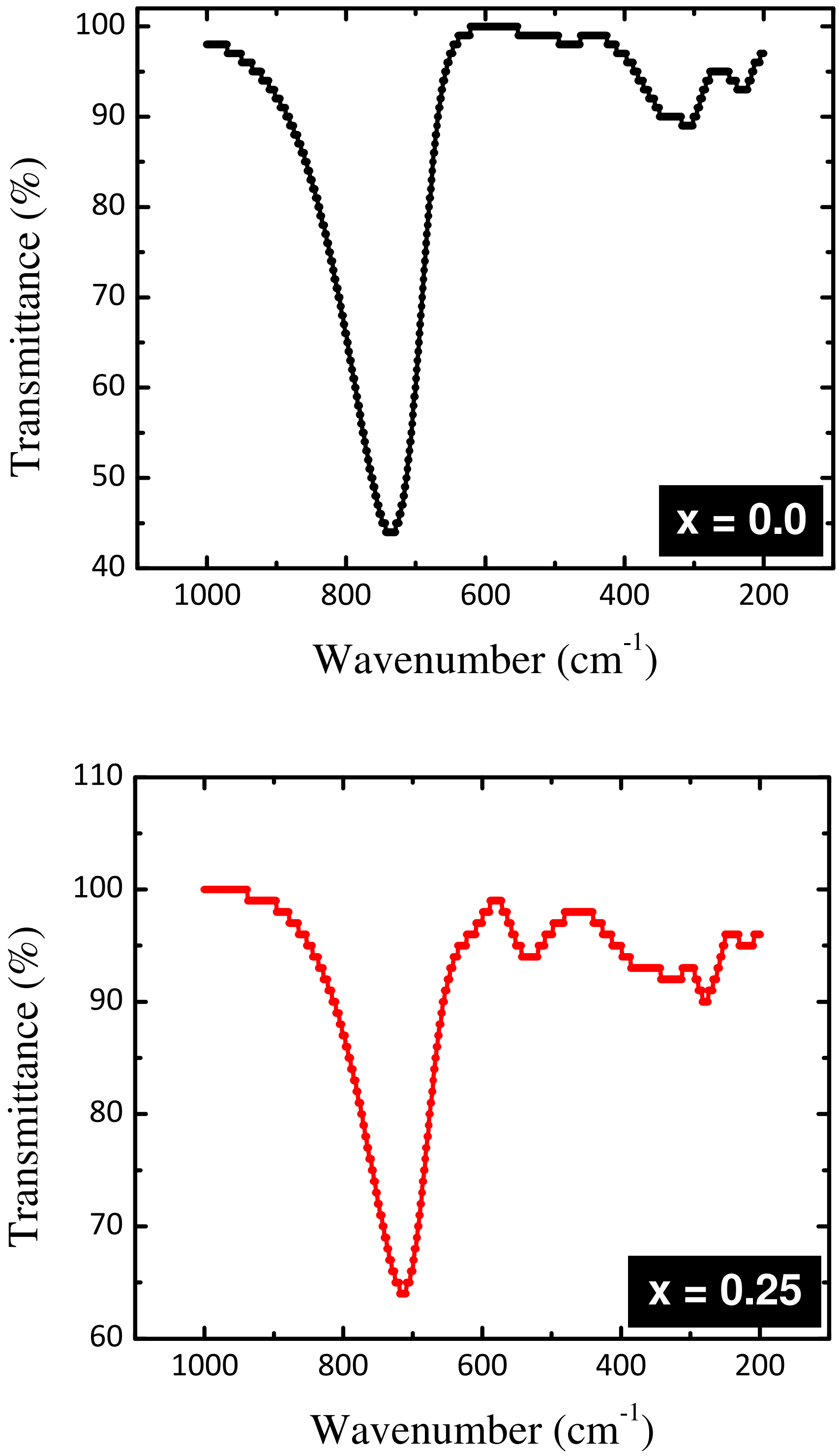

Fig. 5.15 (a): Infrared spectra of x = 0.00 and x = 0.25 for $CoMn_{1-x}Cr_xFeO_4$

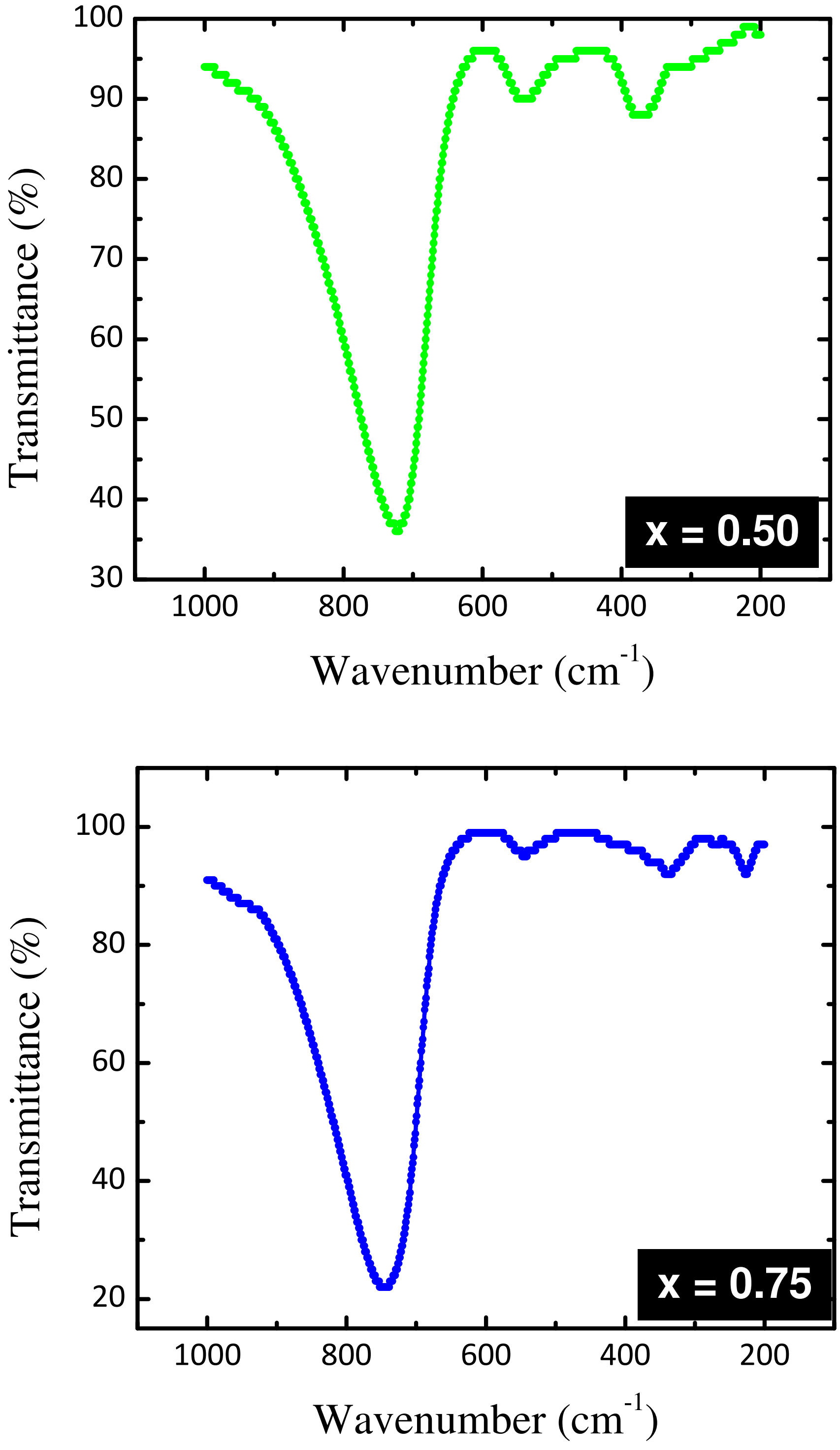

Fig. 5.15 (b): Infrared spectra of x = 0.50 and x = 0.75 for $CoMn_{1-x}Cr_xFeO_4$

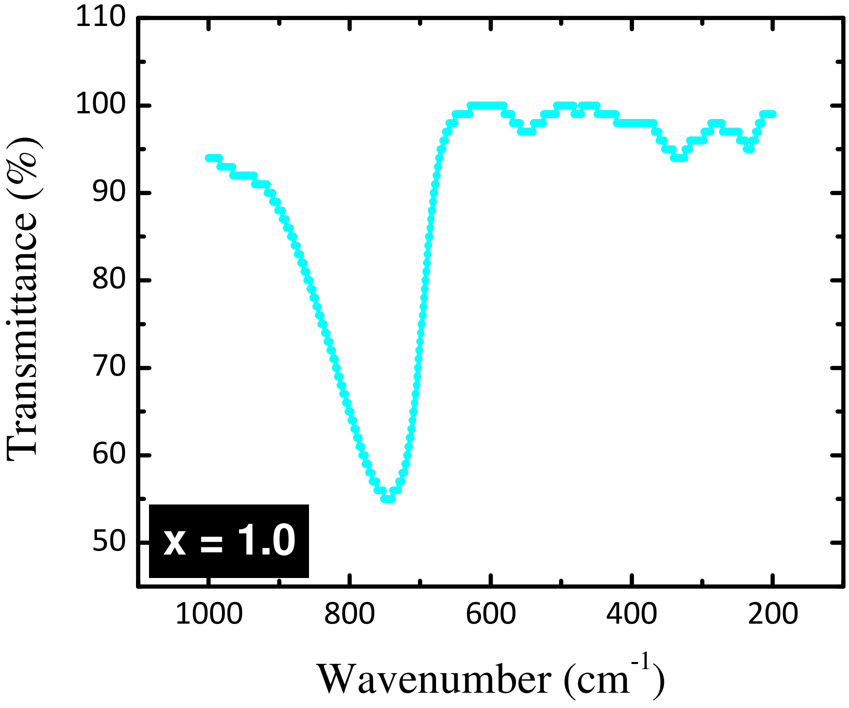

Fig. 5.15 (c): Infrared spectra of x = 1.0 for $CoMn_{1-x}Cr_xFeO_4$

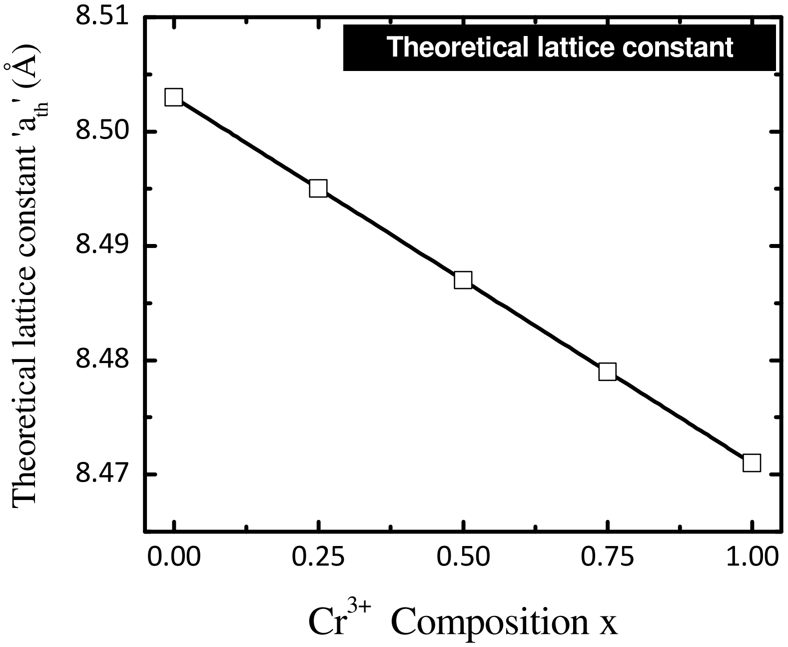

Fig. 5.16: Variation of theoretical lattice constant (a_{th}) with Cr^{3+} composition x for $CoMn_{1-x}Cr_xFeO_4$.

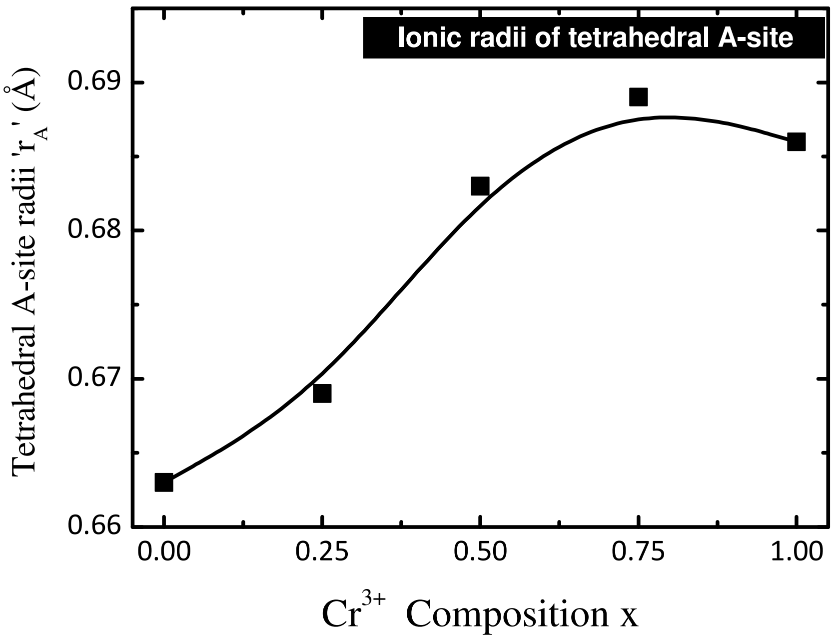

Fig. 5.17: Variation of site tetrahedral A-site ionic radii (r_A) with Cr^{3+} composition x for $CoMn_{1-x}Cr_xFeO_4$.

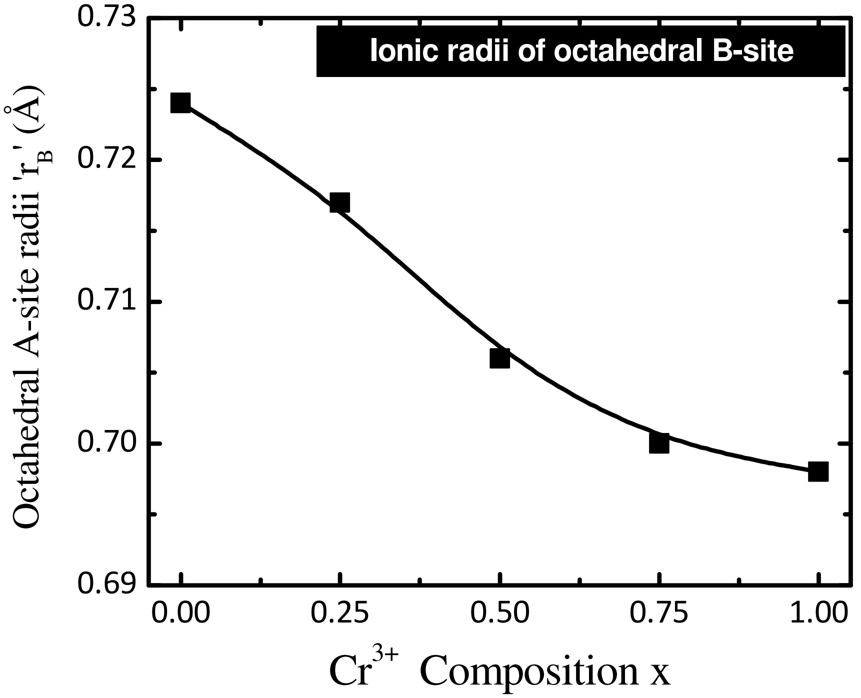

Fig. 5.18: Variation of site octahedral B-site ionic radii (r_B) with Cr^{3+} composition x for $CoMn_{1-x}Cr_xFeO_4$.

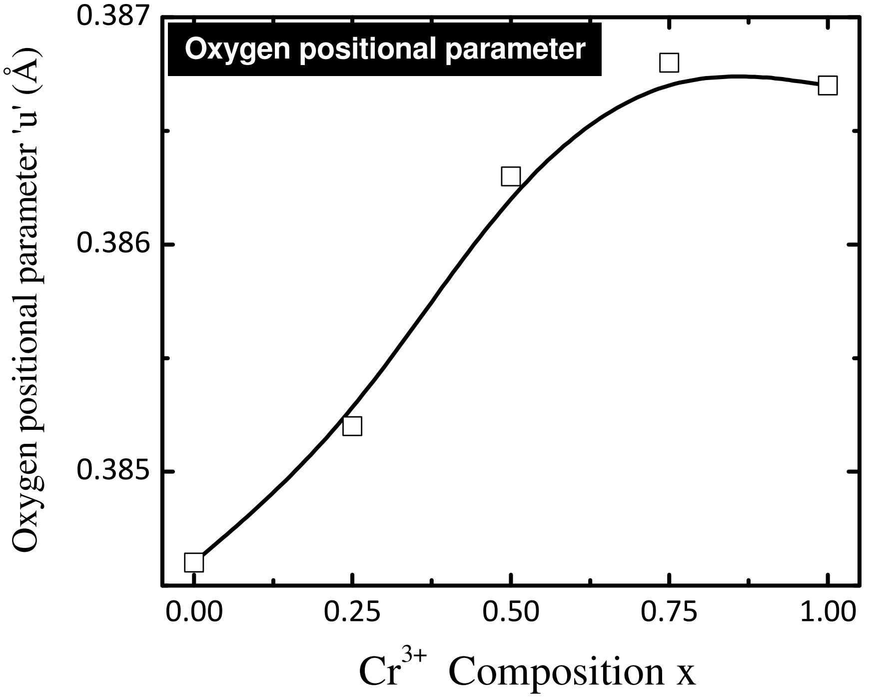

Fig. 5.19: Variation of oxygen parameter (u) with Cr^{3+} composition x for $CoMn_{1-x}Cr_xFeO_4$.

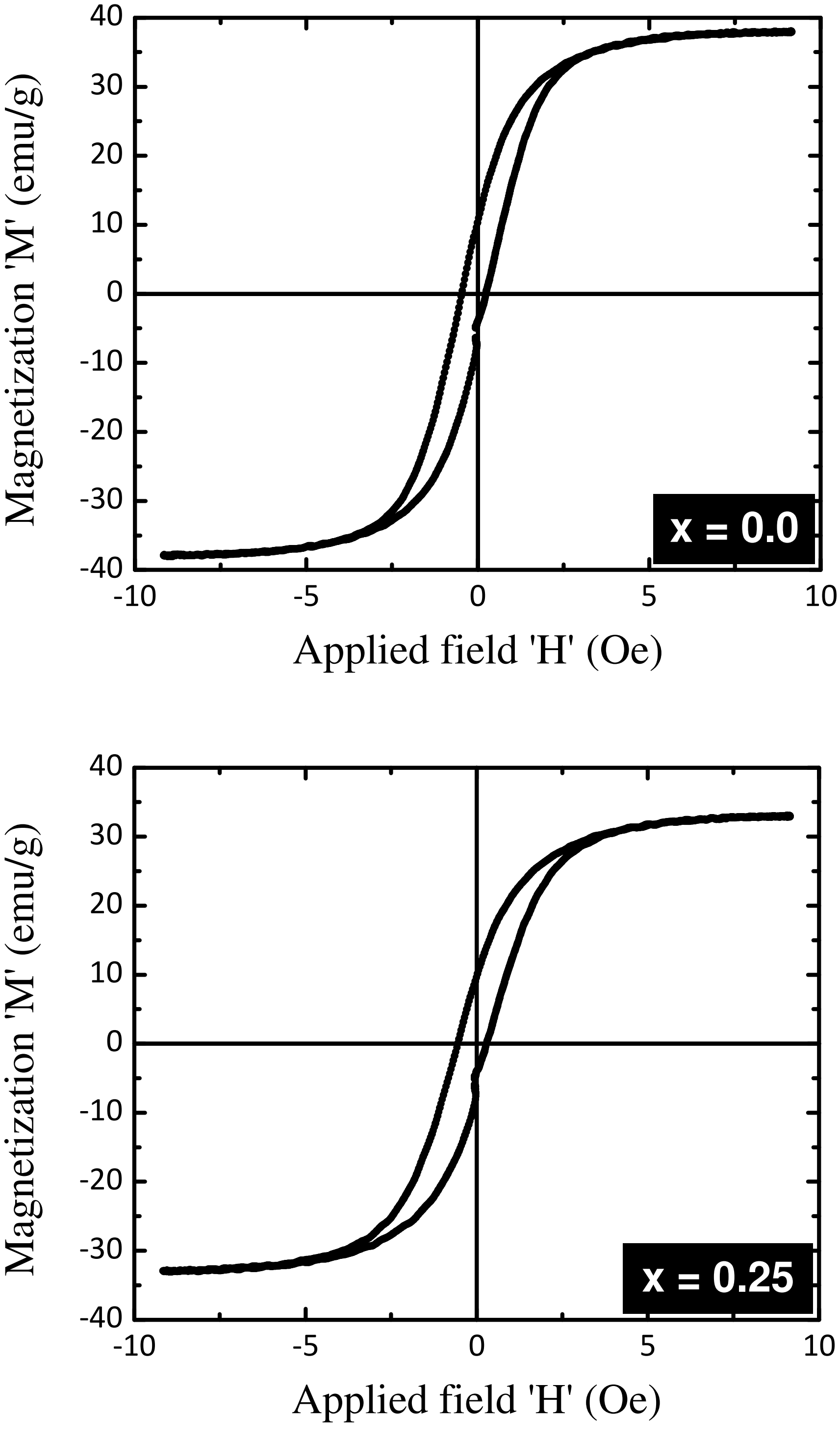

Fig. 5.20 (a): Variation of magnetization (M) with applied field (H) of x = 0.00 and x = 0.25 for $CoMn_{1-x}Cr_xFeO_4$

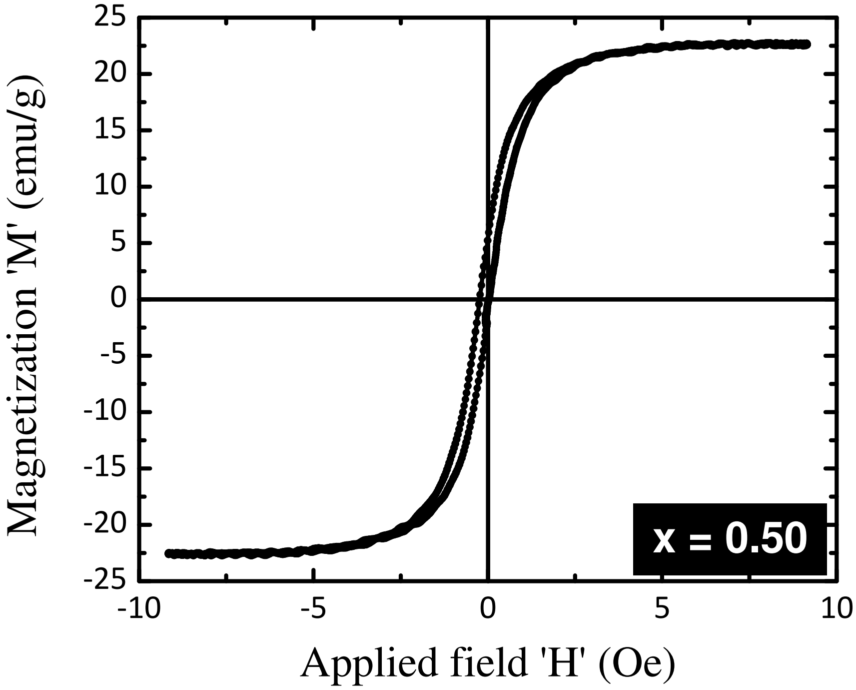

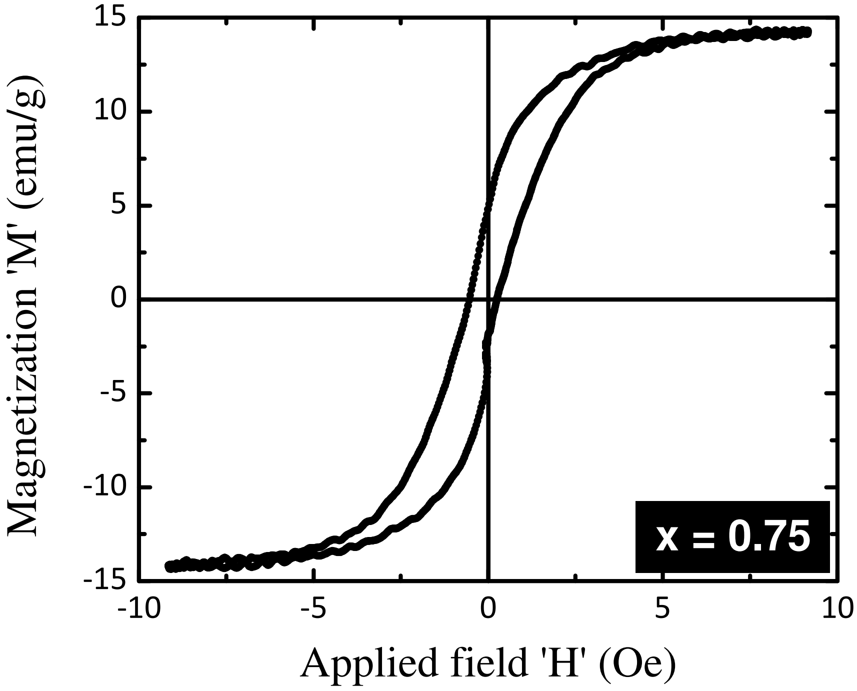

Fig. 5.20 (b): Variation of magnetization (M) with applied field (H) of x = 0.50 and x = 0.75 for $CoMn_{1-x}Cr_xFeO_4$

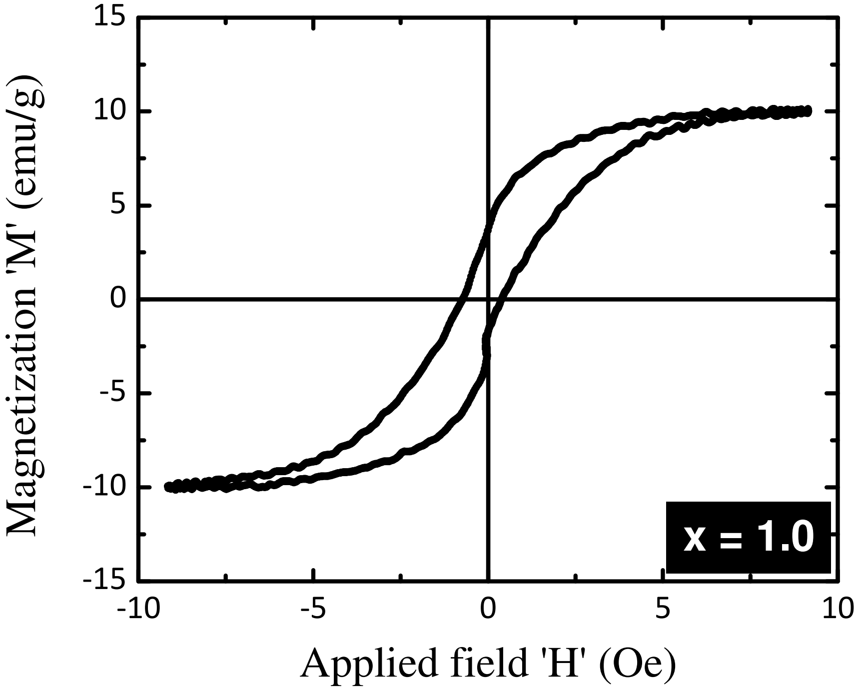

Fig. 5.20 (c): Variation of magnetization (M) with applied field (H) of x = 1.00 for $CoMn_{1-x}Cr_xFeO_4$

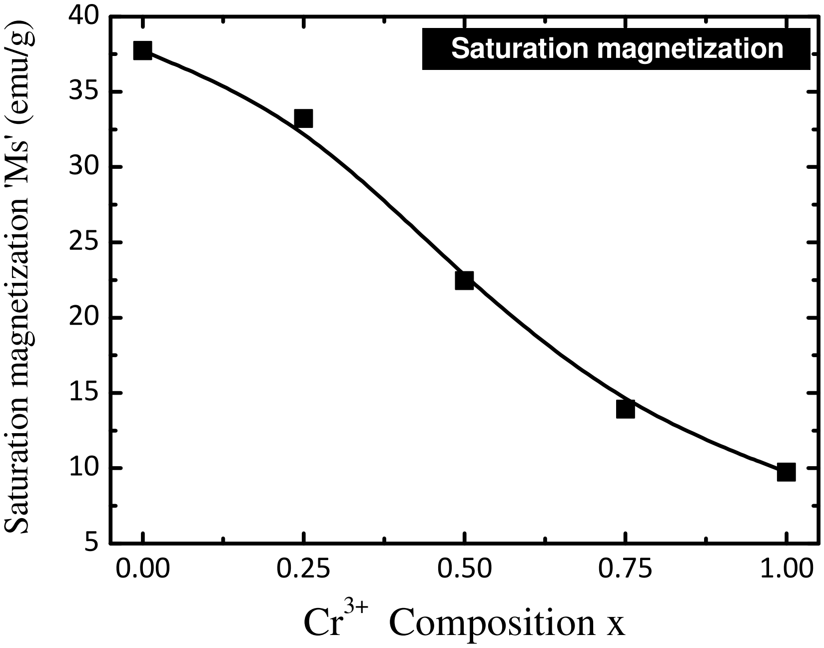

Fig. 5.21: Variation of saturation magnetization (Ms) with Cr^{3+} composition x for $CoMn_{1-x}Cr_xFeO_4$.

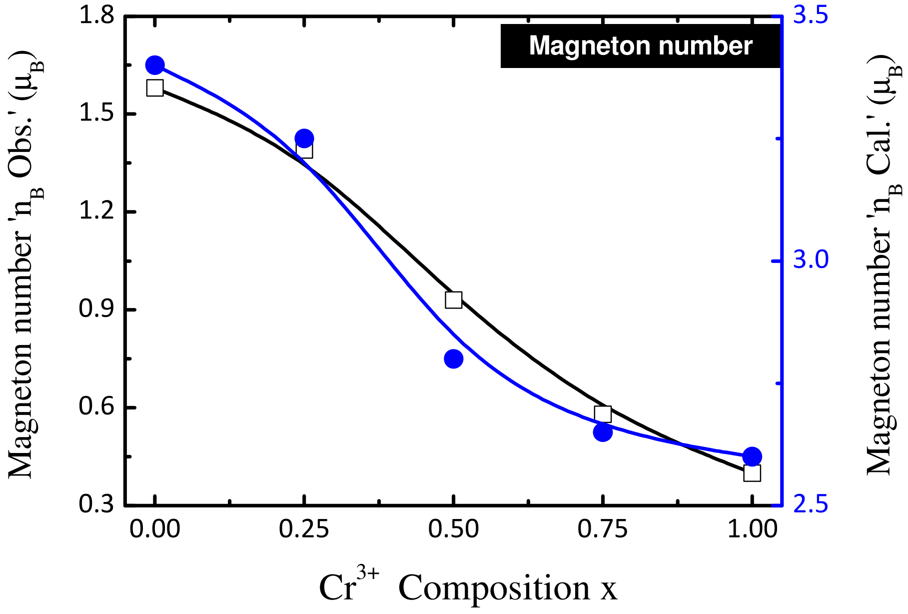

Fig. 5.22: Variation of observed (n_B Obs.) and calculated (n_B Cal.) magneton number with Cr^{3+} composition x for $CoMn_{1-x}Cr_xFeO_4$.

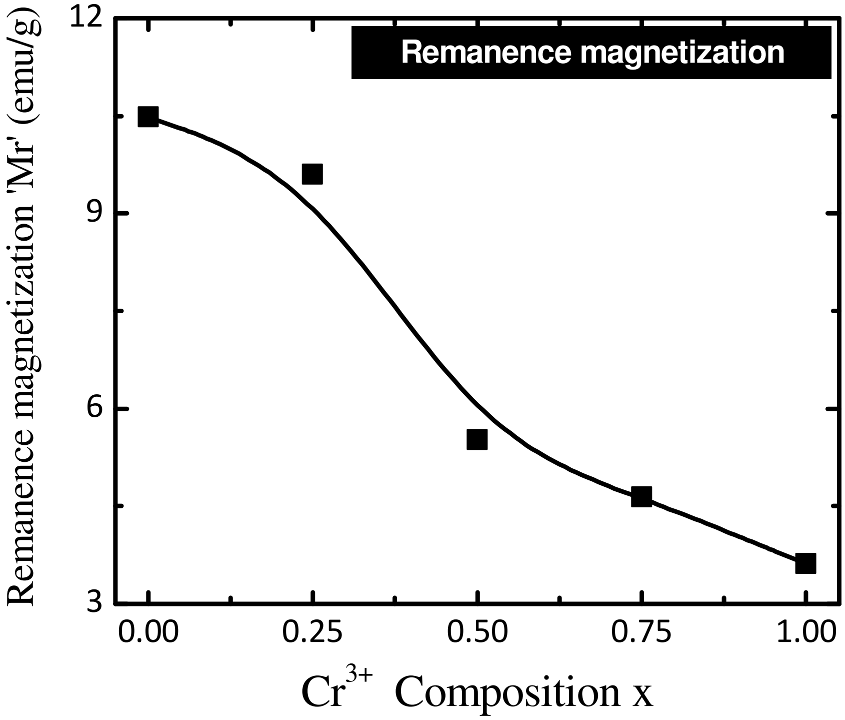

Fig. 5.23: Variation of remanence magnetization (Mr) with Cr^{3+} composition x for $CoMn_{1-x}Cr_xFeO_4$.

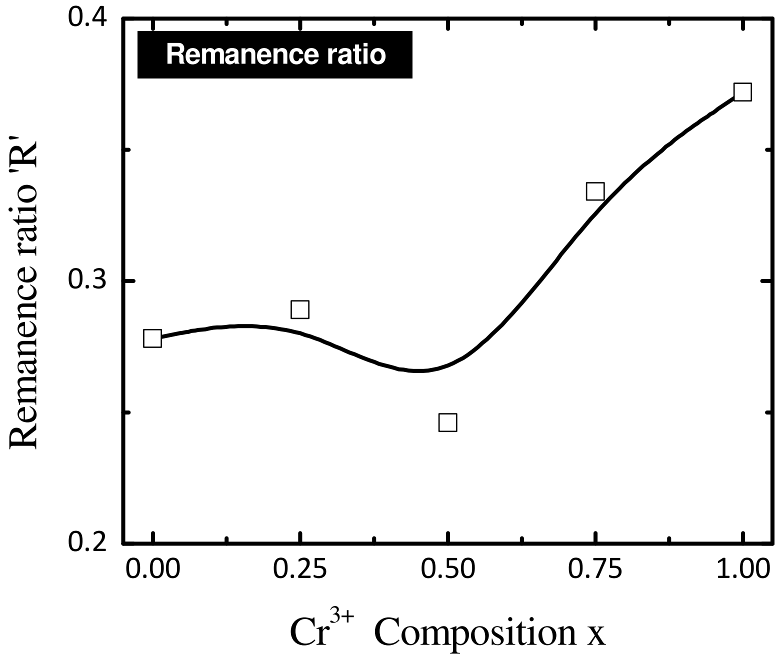

Fig. 5.24: Variation of remanence ratio (R) with Cr^{3+} composition x for $CoMn_{1-x}Cr_xFeO_4$.

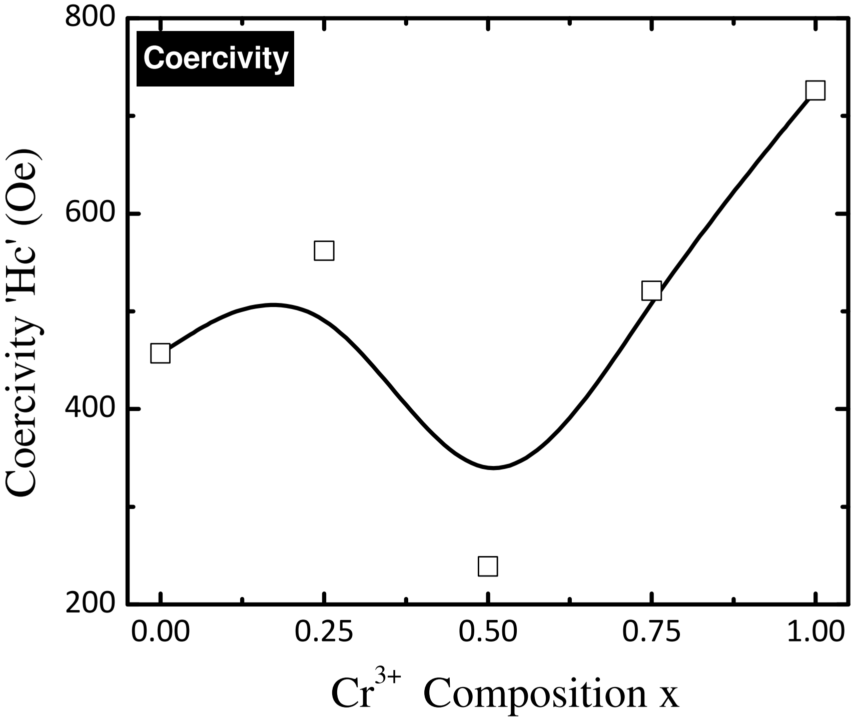

Fig. 5.25: Variation of coercivity (Hc) with Cr^{3+} composition x for $CoMn_{1-x}Cr_xFeO_4$.

Table 5.1

Theoretical percentage of element in $CoMn_{1-x}Cr_xFeO_4$ ferrites.

Comp. x	Theoretical %				
	Co	Mn	Cr	Fe	O
0.00	25.2159	23.506	0.000	23.8954	27.3822
0.25	25.2955	17.686	5.5795	23.9709	27.4686
0.50	25.3756	11.828	11.1943	24.0468	27.5556
0.75	25.4563	5.933	16.8448	24.1232	27.6431
1.00	25.5374	0.000	22.5313	24.2001	27.7312

Table 5.2

Lattice constant (a), X-ray density (d_x), crystallite size (D_{XRD}), bulk density (d_B) and porosity (P) of $CoMn_{1-x}Cr_xFeO_4$

Comp. x	a (Å)	dx (g/cm^3)	D_{XRD} (nm)	d_B (g/cm^3)	P (%)
0.00	8.3972	5.243	19.8	4.121	21.41
0.25	8.3882	5.244	18.5	4.112	21.58
0.50	8.3717	5.258	14.1	4.109	21.86
0.75	8.3588	5.266	16.6	4.107	22.01
1.00	8.3566	5.253	16.3	4.107	21.82

Table 5.3

Hopping lengths (L_A and L_B) of $CoMn_{1-x}Cr_xFeO_4$

Comp. x	Hopping length	
	L_A (Å)	L_B (Å)
0.00	3.6361	2.9689
0.25	3.6322	2.9657
0.50	3.6251	2.9598
0.75	3.6195	2.9553
1.00	3.6185	2.9545

Table 5.4

Tetrahedral bond (d_{AX}), octahedral bond (d_{BX}), tetra edge (d_{AXE}) and octahedral edge (d_{BXE}) (shared and unshared) of $CoMn_{1-x}Cr_xFeO_4$

Comp. x	d_{AX} (Å)	d_{BX} (Å)	Tetra edge (Å)	Octa edge d_{BXE} (Å)	
			d_{AXE}	Shared	unshared
0.00	1.905	2.052	3.111	2.826	2.976
0.25	1.903	2.050	3.108	2.823	2.973
0.50	1.899	2.046	3.101	2.817	2.967
0.75	1.897	2.043	3.097	2.813	2.963
1.00	1.896	2.042	3.096	2.812	2.962

Table 5.5

IR absorption bands of $CoMn_{1-x}Cr_xFeO_4$

Comp. **x**	**□$_1$ (cm^{-1})**	**□$_2$ (cm^{-1})**	**□$_3$ (cm^{-1})**	**□$_4$ (cm^{-1})**
0.00	736	314	494	234
0.25	716	294	533	220
0.50	722	375	540	307
0.75	745	340	547	225
1.00	748	337	551	236

Table 5.6

Cation distribution of $CoMn_{1-x}Cr_xFeO_4$

Comp. x	Cation distribution	
	A-site	B-site
0.00	$Mn_{0.7}Fe_{0.3}$	$Co_{1.0}Mn_{0.3}Fe_{0.7}$
0.25	$Mn_{0.65}Co_{0.05}Fe_{0.3}$	$Mn_{0.1}Co_{0.95}Cr_{0.25}Fe_{0.7}$
0.50	$Mn_{0.35}Co_{0.15}Fe_{0.5}$	$Mn_{0.15}Co_{0.85}Cr_{0.5}Fe_{0.5}$
0.75	$Mn_{0.2}Co_{0.2}Cr_{0.05}Fe_{0.55}$	$Mn_{0.05}Co_{0.8}Cr_{0.7}Fe_{0.45}$
1.00	$Co_{0.2}Cr_{0.2}Fe_{0.6}$	$Co_{0.8}Cr_{0.8}Fe_{0.4}$

Table 5.7

Ionic radii of tetrahedral A-site (r_A), octahedral B-site (r_B), theoretical lattice constant (a_{th}) and oxygen positional parameter (u) of $CoMn_{1-x}Cr_xFeO_4$

Comp. 'x'	r_A (Å)	r_B (Å)	a_{th} (Å)	u (Å)
0.00	0.663	0.724	8.503	0.3846
0.25	0.669	0.717	8.495	0.3852
0.50	0.683	0.706	8.487	0.3863
0.75	0.689	0.700	8.479	0.3868
1.00	0.686	0.698	8.471	0.3867

Table 5.8

Saturation magnetization (Ms), remanence magnetization (Mr), remanence ratio (R), magneton number (η_B) and coercivity (Hc) of $CoMn_{1-x}Cr_xFeO_4$

Comp. x	Ms (emu/g)	M_r (emu/g)	R	η_B (μ_B) Obs.	η_B (μ_B) Cal.	Hc (Oe)
0.00	37.74	10.48	0.278	1.58	3.40	457
0.25	33.22	9.60	0.289	1.39	3.25	562
0.50	22.47	5.52	0.246	0.93	2.80	239
0.75	13.91	4.64	0.334	0.58	2.65	521
1.00	9.73	3.62	0.372	0.40	2.60	726